MODELING OF MULTIPLE-OPTICAL-AXIS PATTERN-INTEGRATED INTERFERENCE LITHOGRAPHY SYSTEMS

A Thesis
Presented to
The Academic Faculty

by

Donald Edward Sedivy III

In Partial Fulfillment
of the Requirements for the Degree
Master of Science in the
School of Electrical and Computer Engineering

Georgia Institute of Technology
May 2014

MODELING OF MULTIPLE-OPTICAL-AXIS PATTERN-INTEGRATED INTERFERENCE LITHOGRAPHY SYSTEMS

Approved by:

Professor Thomas K. Gaylord, Advisor
School of Electrical and Computer Engineering
Georgia Institute of Technology

Professor John A. Buck
School of Electrical and Computer Engineering
Georgia Institute of Technology

Professor Stephen E. Ralph
School of Electrical and Computer Engineering
Georgia Institute of Technology

Date Approved: 27 March 2014

ACKNOWLEDGEMENTS

Over the course of my two years at Georgia Tech, there are many people who have helped me greatly with my research and broader understanding of science and engineering. It is with great humility that I acknowledge their support and contributions

First and foremost, I would like to thank my thesis advisor, Professor Thomas K. Gaylord. Never in my experience as an Army officer have encountered someone who is as professional and thorough as him. By providing the appropriate balance and guidance and the freedom of action, he has allowed me to develop while ensuring that I never strayed too far from the correct path. In addition to conducting research, he has also provided an example of what a teacher and mentor should be. Thank you for your patience and tireless efforts.

I would also like to thank the other members of my thesis committee: Professor John A. Buck and Professor Stephen E. Ralph. Your participation and guidance throughout this process were extremely helpful and enlightening. Knowing that each of you has a busy schedule, I appreciate the time and consideration you gave me.

With regard for my peers, I would like to thank the other members of the Georgia Tech Optics Laboratory for their camaraderie and support. In particular, I would like to thank Matthieu Leibovici for helping me understand his method of PIIL simulation which was invaluable to my own research, Joe Kummer for his help in verifying my modeling procedure and calculations, Micah Jenkins for his extensive knowledge of MATLAB, and of course LTC Matt Burrow from whom I inherited my portion of this well-developed line of research. For our Friday lunch discussion while were simultaneously

thought-provoking and stress-relieving I would additionally like to thank other group members including Dr. Jon Maikisch, Dr. Justin Stay, Dr. Mike Hutsel, Dr. Don Davis, Sylain LeLieprve, Sensen Li, Joshua Long, Austin Sutlief, and Lakshmi Raju.

I would additionally like to thank my parents, Don and Barbara for their lifetime of support and confidence that has led me down this path.

Lastly and most importantly, I would like to thank my wife, Mandy, for her love, support, and patience through this process. I appreciate the sacrifice of allowing me to work the late hours and weekends necessary to complete my research while you wrangled our two children. Although I love to get wrapped up in my work, nothing compares to coming home to you and our children at the end of the day.

Donald E. Sedivy

Georgia Institute of Technology
March 2014

TABLE OF CONTENTS

Page

LIST OF TABLES

Page

LIST OF FIGURES

Page

LIST OF ACRONYMS AND ABBREVIATIONS

DPM	Diffractive photomask
DUV	Deep Ultraviolet
FFS	Free-form Surface
FFT	Fast Fourier Transform
HMD	Head-mounted Display
MBI	Multi-beam Interference
MOA	Multiple-Optical-Axis
MOSFET	Metal-oxide-semiconductor field-effect transistors
IL	Interference Lithography
NA	Numerical Aperture
PC	Perspective control
PIC	Photonic integrated circuit
PII	Pattern-Integrated Interference
PIIL	Pattern-Integrated Interference Lithography
PIIES	Pattern-Integrated Interference Exposure System
SOA	Single-Optical-Axis

SUMMARY

With the demand for increasingly smaller components and devices permeating human existence, Pattern-Integrated Interference Lithography (PIIL), was first developed in the Georgia Tech Optics Laboratory in 2012 as a technique to produce, in a rapid, single-step, interference patterns with integrated functional elements in one, two, and three dimensions [1-10]. This technique was developed for use in the specific application areas of mirco- and nano-electronics [1, 11-14], photonic crystals [1, 15-24], and biomedical structures [1, 20, 25-30] based upon other interference lithography (IL) techniques that had been used for these applications. While a prototype system in a single-optical-axis (SOA) configuration has been experimentally demonstrated as a proof-of-concept, PIIL systems are still in a research and development stage [1-10].

A multiple-optical-axis (MOA) pattern-integrated interference exposures system (PIIES) offers the possibility of large angles of incidence and subsequently smaller crystal lattice constants, but has only been discussed in broad terms [6]. This configuration requires the lenses of the system to be tilted in order for the mask element to be in focus without keystone distortion. This tilt corresponds to perspective control as the planes of the mask, objective lenses, and image plane are all parallel. However, tilting the lenses of the system invariably introduces undesirable effects on both multi-beam interference (MBI) and imaging.

The primary objective of the research presented in this thesis is to establish a methodology for characterizing, simulating, and optimizing an MOA PIIES using a

combination of ray tracing and Fourier analysis applied to the single-element, non-optimal lenses previously used in an SOA PIIES implementation [1, 4, 5]. No attempt has been made to start with more appropriate components. The purpose of this approach is to provide a framework in which future purpose-specific lenses can be designed and their performance evaluated.

In developing this methodology, a background understanding of MBI, IL, PIIL, and off-axis imaging is required to understand the fundamental principles affecting system modeling. A review of application areas for PIIL as well an overview of PIIL system configurations and impact is presented to provide context for this research.

With the context for PIIL systems properly established, ray optics was used to formulate a characterization model to describe the aberrations that occur in an MOA PIIL system. The characterization and optimization were performed on a single axis of a MOA configuration under the assumption that all axes of the system were degenerate. A set of interference/image pattern metrics, collimation and ray spot diagram, were used to respectively describe the quality of the periodic pattern and mask image formed. The optical system parameters for this model involved the spacing between the optical elements of the system. The optimization of collimation and image quality individually produce generally similar requirements on the optical system. The large amounts of divergence and displacement in the spot pattern that occur with higher angles of tilt indicate that a more purpose-specific optical system would be needed to correct these effects further for larger tilt angles.

While the characterization analysis of an MOA PIIES provided a very quantitative assessment of system performance, it did not provide example images for evaluation. To this end, a method for simulating a full MOA PIIES using a combination of ray tracing and Fourier optics was developed using a three-axis MOA PIIL configuration. Simulation results show that even for the non-optimized components used in this MOA PIIES configuration, a pattern-integrated interference pattern can be produced with reasonably high fidelity.

In place of the fixed non-optimal commercial components used here, custom optical elements could be designed to improve the quality of the desired combination of interference and imaging. Increased angles of incidence/tilt in the system configuration would also be possible allowing for smaller-sized periodic elements.

CHAPTER 1

INTRODUCTION

With the advent of the modern age of technology, human existence has continued to realize capabilities once reserved for the realm of science fiction. From the internet, to cell phones, and global positioning devices enabled by advance optical and micro-electronic components, to advanced prosthetics, and artificially regrown tissues and organs; the research conducted in the areas of mirco-and nano-electronics, photonic crystals, and biomedical structures have enabled and will continue to enable humanity to vastly improve the condition of society. With specific regard to electronics, Gordon Moore, a co-founder of Intel, predicted that the number of transistors in commercially available products would double approximately every two years [1]. While this has held largely true for the past five decades, technology is rapidly approaching the scale where optical lithography, the current tool of choice for semiconductor manufacturing, will be unable to fulfill the required demand for faster and smaller devices predicted by Moore's Law without an improvement in technique or technology. To this end, various other techniques are currently being investigated as a viable economic alternative to replace traditional optical lithography [1, 11, 20]. One such technique that has demonstrated promise is interference lithography (IL) which is also referred to as "holographic" or "interferometric" lithography [1, 31-34]. Beyond electronics, the areas of photonic crystals and biomedical structures also have great interest in IL for the production of

periodic structures with integrated functional elements at the mirco- and nano-scale [1, 15-24].

While many different techniques are currently available to produce the functional elements for an interference-lithography-generated structure, Pattern-Integrated Interference Lithography (PIIL), first developed in the Georgia Tech Optics Laboratory in 2012, provides an attractive option for a variety of applications as it can produce in a single-step, interference patterns with integrated functional elements in one, two, and three dimensions [1-10]. While a prototype system in a single-optical-axis (SOA) configuration has been experimentally demonstrated as a proof-of-concept, PIIL systems are still in a research and development stage [1-10].

1.1 Background

1.1.1 Multi-Beam Interference

All IL techniques are dependent upon the principles of multi-beam interference. There are five primary parameters which can be adjusted to determine the size and shape of an interference pattern: the wavelength of each incident beam, its wavevector orientation, its polarization, phase, and amplitude.

The wavelength of incident light and angle of incidence, dictated by each beam's wavevector configuration, determine the size of the periodic pattern that is imaged. In the case of two beam interference, the period of the interference pattern is $\Lambda = \lambda / 2 \sin \theta$ where λ is the wavelength of incident light and θ is the magnitude of the angle of incidence of both beams [1, 35]. In the general case of plane-wave multi-beam interference, the intensity distribution formed in the image plane is given as

$$I_T(r) = I_0\{1 + \sum_{j>i}^{N} V_{ij} \cos[(\boldsymbol{k_j} - \boldsymbol{k_i}) \cdot \boldsymbol{r} + \varphi_i - \varphi_j]\}, \quad (1)$$

where I_0 is the DC intensity term for each beam summed together, $\boldsymbol{r}$ is the radial position on the image plane where the interference pattern intensity is evaluated, $\boldsymbol{k}$ is the wavevector of each respective beam, φ is the phase of each beam at the image plane, and V_{ij} is an interference coefficient defined in terms of the electric field vectors $\boldsymbol{E_i}$ and $\boldsymbol{E_j}$ for each beam where $V_{ij} = \boldsymbol{E_i} \cdot \boldsymbol{E_j}/I_0$.

The periodicity of the interference pattern formed depends on the argument of the cosine function. A relative phase shift, $(\varphi_i - \varphi_j)$, between any two beams will shift that subcomponent of the lattice structure. The $(\boldsymbol{k_j} - \boldsymbol{k_i})$ term depends on both the wavelength and wavevector configuration. It determines the periodicity and translational symmetry of the lattice structure. Figure 1(a) indicates the configuration for square lattice symmetry. For any number of interfering beams, decreasing the wavelength and increasing the angle of incidence reduces the period of that particular interference pattern. This is desirable as photonic crystal and microelectronic manufacturers continuously seek to reduce the size of their devices.

Multi-beam interference can be thought of as a superposition of multiple 1D, two-beam interference patterns that are superimposed as shown in Figure 1 for the case of three-beam interference. The manner in which these 1D patterns interact and interfere is determined by the interference coefficient, V_{ij}, which contains the information about the relative polarizations and amplitudes of each two-beam combination. This, along with the wavevector configuration determines the specific shape of the motifs and the particular lattice formed. Specific configurations for a *p4m* and *cmm* square lattice are

shown in Figure 1. By properly manipulating the variables in Eq. (1) and with sufficient beams, it is possible to produce all five 2D and all fourteen 3D Bravais lattices [36, 37].

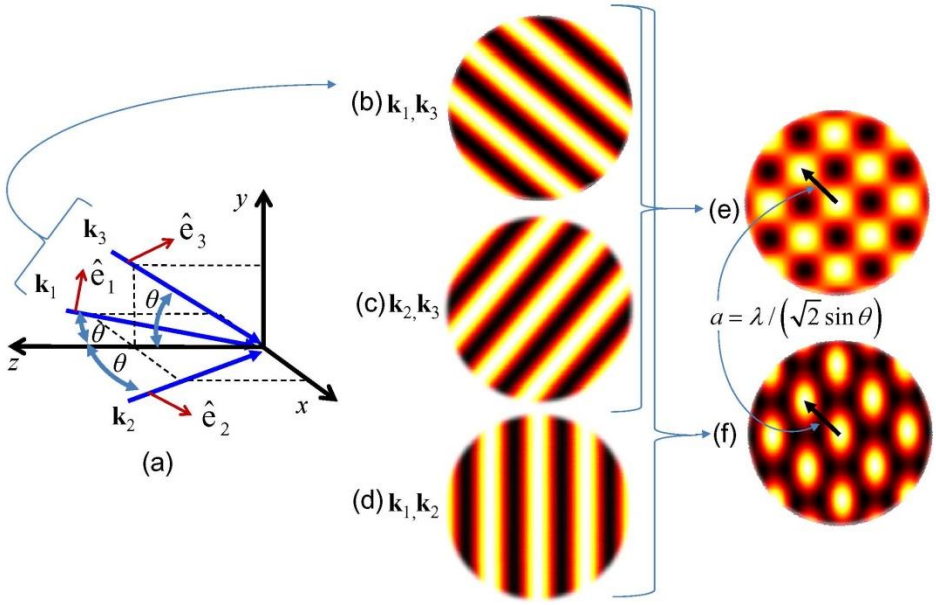

Figure 1: Three-beam interference. (a) Three beams defined by k_1, k_2, and k_3 interfere at the *x-y* plane at a common angle of incidence, θ, with respect to the *z* axis. The beam pairs defined by (b) k_1 and k_3, (c) k_2 and k_3, and (d) k_1 and k_2 form three distinct 1D interference-fringe patterns. (e) The fringes patterns of k_1 and k_2 and k_1 and k_3 combine to form a square lattice with *p4m* plane-group symmetry. (f) The fringe pattern of k_1 and k_2 combine with the other two fringe patterns to form a square lattice with *cmm* plane-group symmetry [1].

1.1.2 Interference Lithography

Photosensitive materials allow for the interference patterns generated by multi-beam interference to be recorded for a variety of uses. As early as 1970, a 1D diffraction grating was recorded in photoresist for use in thin-film waveguides fabricated with simple two-beam interference [1, 38]. Almost twenty years later, multiple two-beam exposures were demonstrated to produce 2D patterns in a photoresist by rotating the material between exposures [39]. By using more than two beams during a single exposure, more complex structures can be generated as implied by Eq. (1). Expanding

upon these foundations, IL has been demonstrated the ability to record a wide range of 1D, 2D, and 3D structures in a variety of materials that respond to wavelengths in the near-infrared [25, 40], visible light [26, 41], ultraviolet (UV) [24, 42], deep-UV [12, 43], and extreme-UV ranges [1, 44, 45].

Currently, IL is seen as a potential candidate to allow optical lithography to continue meeting demand for smaller and faster devices [1, 31]. While IL has the advantages of rapid production, simple optical components, high volume production, and low cost, one of the drawbacks is that IL can only generate periodic patterns [1]. To introduce interference-period scale functional elements required for integrated devices in microelectronics and photonic crystals, another lithographic technique in addition to IL is required. To this end, a variety of techniques have been developed to complement IL. These techniques include: electron beam lithography [46, 47], focused ion beam [48], direct laser writing [17, 49], atomic force microscope nano-indentation [50], multi-photon polymerization [51], projection lithography [52], contact lithography [53], and proximity lithography [1, 53].

As indicated in Table 1.1, these various techniques have advantages and disadvantages associated with them based on four attributes that are essential to high-volume commercial production: speed of the technique, whether or not the produced can be incorporated in a single exposure (implying an ability for high throughput), the cost effectiveness associated with the technique, and whether or not it can produce high-spatial-frequency (sharp-edged) integrated functional elements [1]. While the first five techniques listed are very effective at producing sharp features at the scale of the interference period, they are expensive and time consuming making them ill-suited to

large volume commercial production. Projection and contact lithography have improved speed compared with these other techniques, but are still prohibitive expensive for large volume production [1, 51]. While proximity lithography has the advantages of rapid and cheap production, it still lacks the ability to produce sharp, interference-period scale elements making it ill-suited to commercial production [1, 51, 53, 54]. Considering the shortfalls of the current techniques applied to IL for high volume commercial technologies, Pattern-Integrated Interference Lithography (PIIL) was introduced by the Georgia Tech Optics Laboratory to fulfill this perceived deficiency [1-10].

Table 1: Comparison of combined techniques to fabricate non-periodic functional elements in an MBI-defined periodic lattice [1].

Functional Element Fabrication Technique	Technique Characteristics			
	Fast?	Single Exposure?	Cost Effective?	High-Spatial-Frequency Integrated Functional Elements?
Electron Beam Lithography	No	No	No	Yes
Focused Ion Beam	No	No	No	Yes
Direct Laser Writing	No	No	No	Yes
Atomic Force Microscope Nano-Indentation	No	No	No	Yes
Multi-Photon Polymerization	No	No	No	Yes
Projection Lithography	Yes	No	No	Yes
Contact Lithography	Yes	Yes	No	Yes
Proximity Lithography	Yes	Yes	Yes	No
Pattern-Integrated Interference Lithography	**Yes**	**Yes**	**Yes**	**Yes**

1.1.3 Pattern-Integrated Interference Lithography

Pattern-Integrated Interference Lithography (PIIL) simultaneously combines multi-beam interference, IL, and imaging to produce in a single exposure a periodic pattern with

integrated functional elements offering interesting possibilities for next-generation periodic structures [1, 4-7, 9, 10]. In combining them, the multi-beam interference disrupts the imaging and the imaging disrupts the multi-beam interference. However, it has been shown that they still can be done together with usable fidelity, indicating promise for high-volume commercial applications [1]. In a prototype exposure system depicted in Figure 1 [1], a 7f optical system with a 4f optical imaging subsystem constructed along a single optical axis (SOA) was used to confirm experimentally the capabilities of PIIL [1, 4, 5]. The system was designed to accommodate three coherent beams (two beams are depicted in Figure 2, the third beam would lie out of plane and was omitted for simplicity) which would each illuminate the same mask pattern of arbitrary shape. The 4f subsystem would then image these interfering beams upon a photoresist with the mask pattern integrated within the 2D interference pattern.

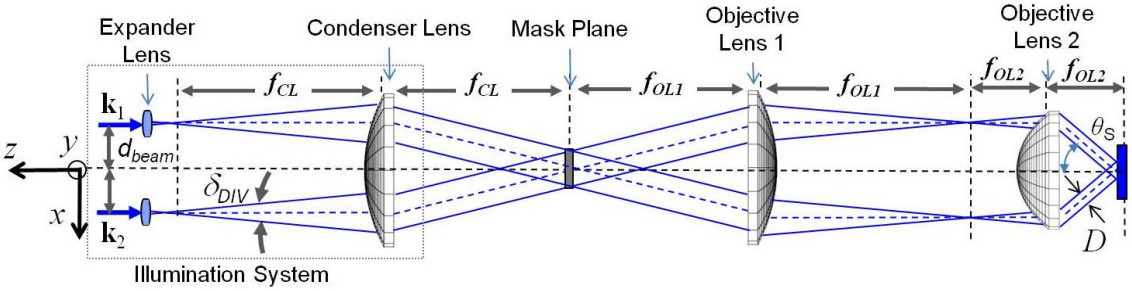

Figure 2: Prototype SOA PIIES configuration. A 7f optical system with a 4f optical imaging subsystem which begins at the mask plane and ends at the photoresist (image) plane [1].

While this system is impressive in its degree of simplicity and the quality of image/interference patterns that it can produce, one of the primary limitations to a SOA configuration is that the sizes of the lenses used in the system determine maximum angle of incidence of the beams and consequently the minimum size of the associated

interference pattern. For this prototype SOA PIIES which used the largest commercially available aspheric lenses, it was only able to achieve an angle of incidence of no more than 30° [1]. To decouple the size of the lenses used from the maximum angles of incidence, a multiple-optical-axis (MOA) PIIES, as shown in Figure 3, can be used [10]. However, for the image/interference pattern to be in focus without keystone distortion, the 4f subsystem lenses must be tilted relative to each individual axis resulting in an off-axis imaging system. AN MOA PIIES has only been described in broad terms and has yet to have been investigated in-depth [6].

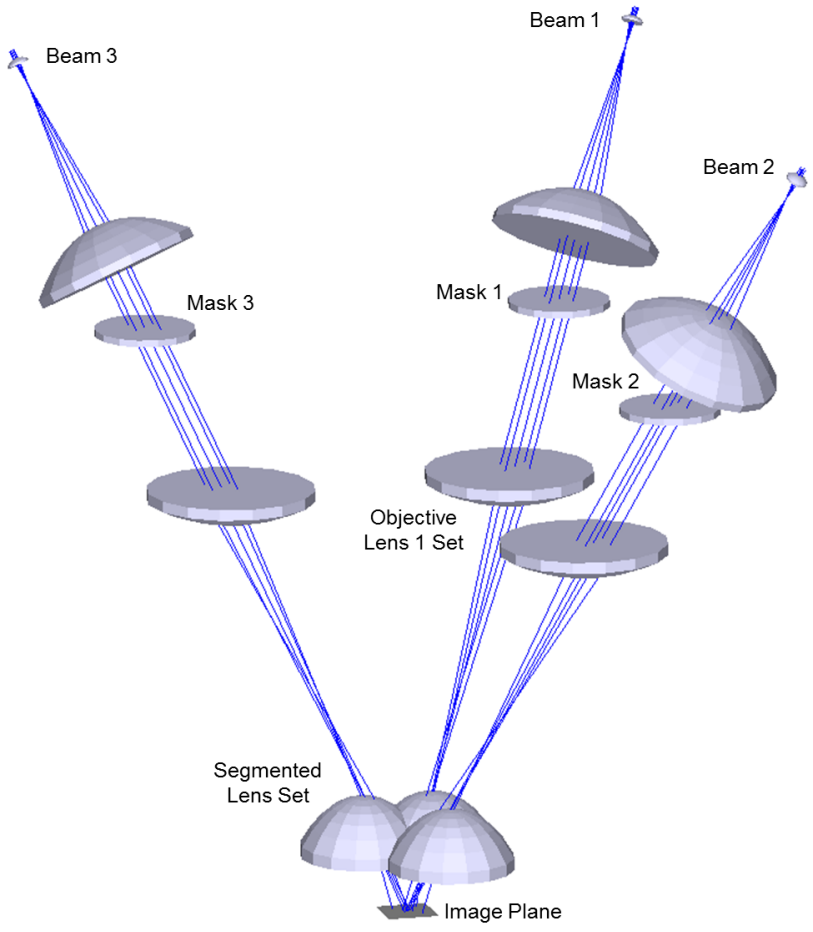

Figure 3: MOA PIIES configuration. Note that the 4f optical imaging subsystem is tilted with respect to each individual optical axis to ensure that each element of this subsystem is in a parallel plane to the image plane preventing keystone distortion.

1.1.4 Off-Axis Imaging

When introducing tilted elements into an optical system, two key conditions that may arise are perspective control and on-axis tilted-object imaging. Perspective control corresponds to distortionless off-axis imaging. It is achieved through the displacement of lenses in a system while on-axis tilted-object imaging is achieved by satisfying the Scheimpflug condition [55]. Imaging with tilted optical elements generally occur in devices where a wide field of view is required such as in a panoramic lens where perspective control is required or a head-mounted display (HMD) where on-axis tilted-object imaging must be achieved [56-58].

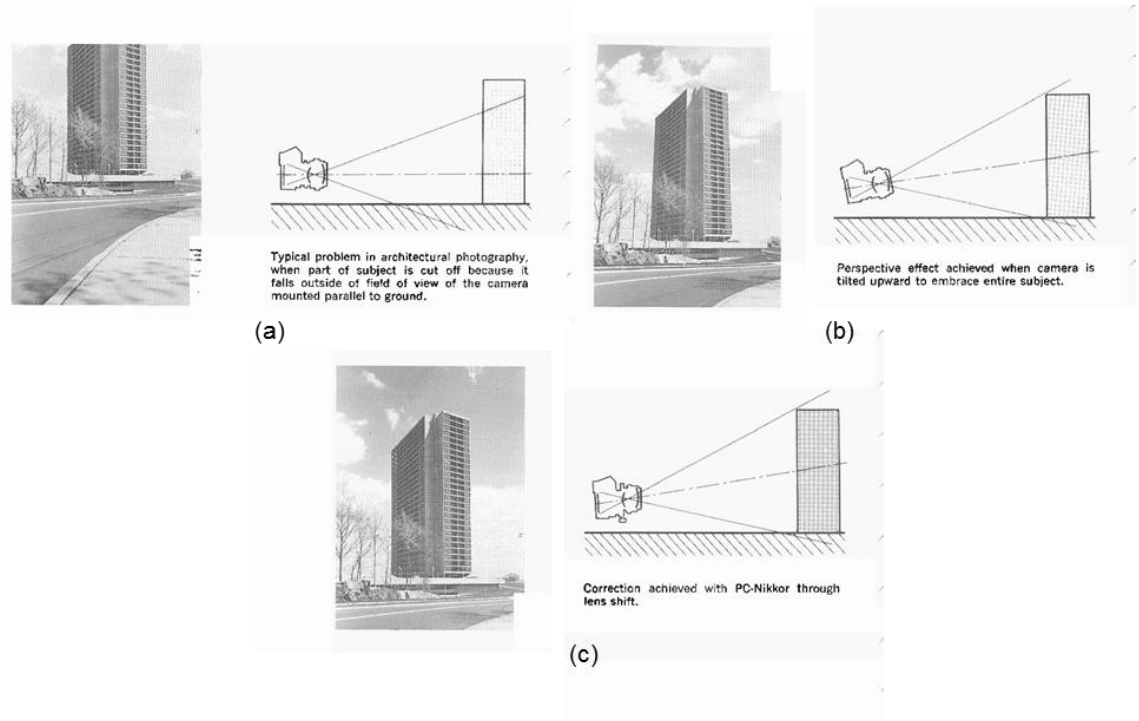

Figure 4: Perspective Control. (a) Picture taken with the camera oriented parallel to the building with the top of the building cut-off. (b) "Perspective effect" caused when the camera is tilted upwards to view the entire object. Note that the building appears to be "falling away" at the top. (c) Correction of his effect using a PC lens where the building appears vertical [59].

If a photographer were to tilt their camera in an attempt to capture the entire height of a building, the resulting image would experience keystone distortion as depicted in Figure 4(b). If the camera were kept level, the photographer would be unable to capture the entire extent of the building as depicted in Figure 4(a). However, a perspective control (PC) lens system solves this problem with a suitably designed mount that allows the lens system to undergo a lateral shift. This shift ensures that the object, lens system, and imaging plane of the camera are in parallel planes resulting in an image as depicted in Figure 4(c) where the building is shown in its entirety without keystone distortion. The resulting system configuration is an off-axis imaging system that is analogous to the MOA PIIES system shown in Figure 3.

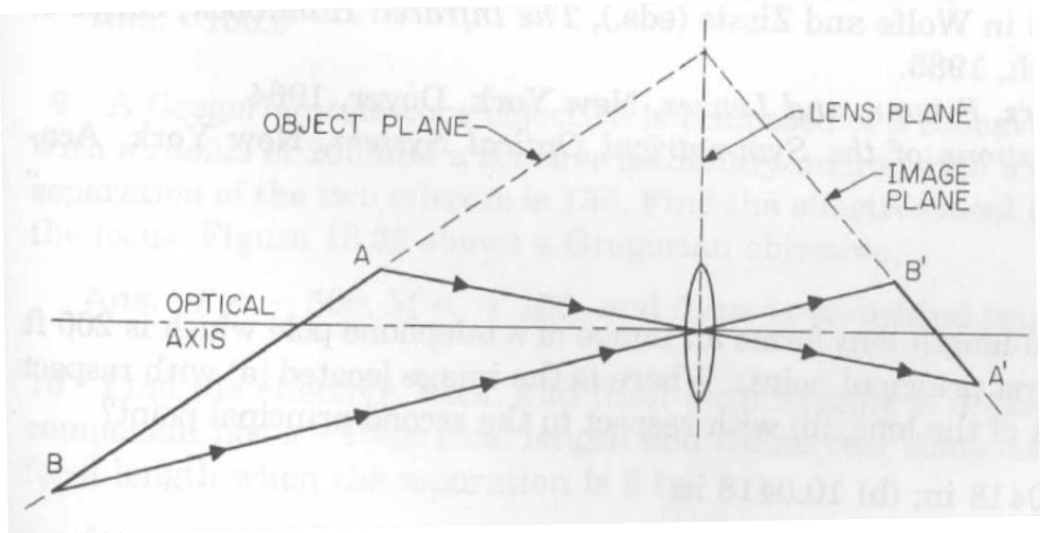

Figure 5: Depiction of the Scheimpflug condition. The object and images planes must intersect in the plane of the lens to ensure on-axis tilted-object imaging [55].

If an object's plane is tilted with respect to the principle plane of a lens or lens system, the image formed by the optical system is also in a tilted plane which is oriented such that the object and image planes will intersect each other in the plane of the lens as shown in Figure 5 [55]. Satisfaction of this requirement is called the Scheimpflug

condition and ensures on-axis tilted-object imaging [55]. This does not occur in the MOA PIIES depicted in Figure 3 as all optical components in the imaging portion of the system have principle planes that are parallel to their respective mask (object) and image planes.

In designing off-axis imaging systems, ray tracing has been used as an effective procedure to characterize and optimize the aberrations in the system. In the case of a panoramic optical system, a group of researchers from Shanghai University developed a ray tracing program to model and optimize a fish-eye style panoramic lens with a 170.8° field of view as shown in Figure 6 [56]. By developing a series of merit functions describing the aberrations in the optical system and propagating rays through it, they were able to optimize a series of optical system parameters that included the radius of curvature and thickness for each lens as well as the lens spacing to minimize the aberrations for both on-axis rays as well as off-axis rays [56]. Since the planes for each component lens lie in the same plane as the object and image planes, this imaging case corresponds to off-axis distortionless imaging case (perspective control).

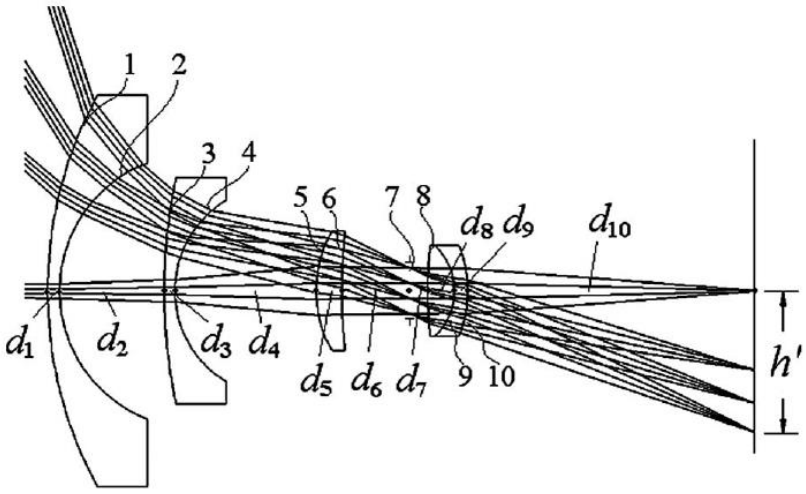

Figure 6: Optical scheme of a fish-eye lens optimized through ray-tracing [56].

Similarly, another group of researchers from Beijing University developed a ray tracing approach to design a compact HMD required to have a wide field of view [57]. They developed a series of merit functions to describe the distortion present in their final image for optimization; however, rather than optimizing each component of the optical system, they chose to optimize a free-form lens/prism. A free-from lens/prism is an optical element that can have each of its optical surface independently designed and custom built. This allows the HMD to fulfill its the wide field of view requirement while leaving other optical components intact as depicted in Figure 7 [57]. In setting the tilts and decenters for each surface of this freeform lens/prism as optical parameters to be optimized, they were able to design a HMD that had less that 5% distortion in its display [57]. Since the optical components of the HMD do not lie in the same plane as the object and image planes for the system, this imaging case corresponds to the satisfaction of the Scheimpflug condition to achieve on-axis tilted-object imaging.

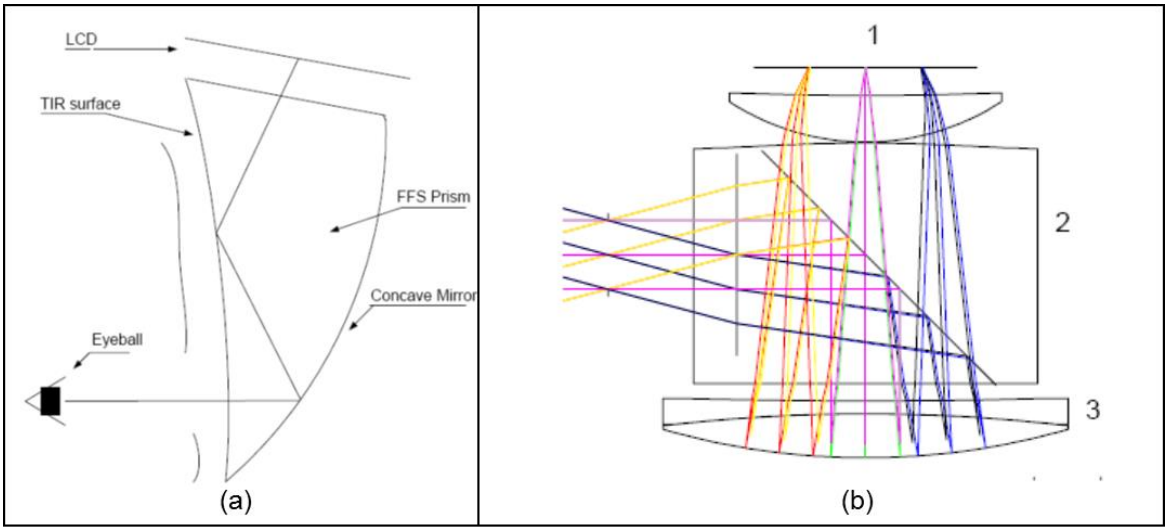

Figure 7: (a) HMD concept design with a free-form prism and (b) implemented with additional aspheric lenses. The free-form prism was designed for off-axis use and optimized via ray tracing analysis [57].

Whether perspective control or on-axis tilted-object imaging is the desired outcome, common to each approach of imaging system design is the use of ray tracing to describe the imaging properties of the system, the construction of a merit function designed to evaluate its performance, and the optimization of system parameters to improve performance. MOA PIIES is also an off-axis imaging system that corresponds to the specific case of perspective control. Based on current research, ray tracing seems a logical approach to describe and optimize such a system.

1.2 Research Objectives and Contributions

With the successful construction and experimental testing of a prototype PIIES in a SOA configuration, the research presented in this thesis explores and defines a methodology of modeling to be associated with an MOA system configuration for PIIL. Specifically, the characterization, optimization, and simulation of an MOA PIIES presented in this thesis resulted in the fulfillment the following objectives and contributions:

1. The development of a ray-tracing approach based upon a series of system parameters, intensity pattern metrics, and optical system metrics to characterize the collimation and imaging performance of an MOA PIIES.
2. The development of an optimization process using a ray tracing approach to minimize the divergence and aberrations of an MOA PIIES for a given set of optical components.
3. The development of a method to export successfully binary ray tracing data from ZEMAX optical design software into MATLAB to build a simulation model.

4. The development of a simulation model combining the advantages of ray tracing and Fourier optics to model successfully the image/interference pattern produced by an MOA PIIES.

1.3 Thesis Overview

The preceding research objectives and contributions are examined in detail in subsequent chapters.

Firstly, Chapter 2 presents an overview of current PIIL application areas. Following this, Chapter 3 provides an in-depth discussion of the various available PIIL system configurations and an overview of the potential overall impact of PIIL. After the establishment of the context for PIIL, Chapter 4 presents a rigorous explanation of the ray tracing approach taken to characterize and optimize an MOA PIIES. The metrics used and the results for an MOA PIIES using non-optimal optical elements are given in detail. While this characterization will be highly quantitative in nature, it does not provide example images for a more straightforward analysis. To this end, in Chapter 5, a simulation model for an MOA PIIES that combines both ray tracing and Fourier optics to generate the an approximation of the image/interference pattern produced by the system is developed. The results of this simulation model with a common set of 90° waveguide bend masks as well as different masks for each of the system axes is presented in Chapter 6. Chapter 7 summarizes the results of this research and provides a detailed look into future work relevant to the development of custom optical elements which can be evaluated using the techniques described in this research to ultimately facilitate an experimental demonstration of an MOA PIIES.

CHAPTER 2

PIIL APPLICATION AREAS

Pattern-Integrated Interference Lithography (PIIL) has a variety of interesting application areas that involve fabrication at the mirco- and nano-scale that can have profound effects for commercial-scale production. While mirco- and nano-electronics are areas with a high degree of interest, photonic crystal and biomedical structures are nascent areas that are poised for large growth in which PIIL may potentially be an enabling technology for large-scale commercial production.

2.1 Micro- and Nano-electronics

As initially discussed in Chapter 1, mirco- and nano-electronics fabrication is approaching the limits of traditional projection lithography while demand for smaller and faster devices remains unabated [1, 11, 20]. To meet this demand, interference lithography (IL) has been proposed as a fast and cost-effective solution for nano-scale electronics fabrication [11-14]. In 2004, a set of triple-gate metal-oxide-semiconductor field-effect transistors (MOSFETs) was fabricated using IL with a 266 nm DUV laser to achieve element spacing down to 150 nm as shown in Figure 8(a) [14]. Moreover, in 2005 IL using a 157 nm excimer laser a 2D structure was fabricating in photoresist with element spacing down to 90 nm as shown in Figure 8(b) [11-13]. While impressive, the drawback to using IL alone is that fabrication is limited to only periodic structures. However; in 2012 it was demonstrated in a proof-of-concept experiment that PIIL could produce integrated functional elements on the scale of the interference pattern in a single

exposure using a 363.8 nm (Ar ion laser) source as shown in Figure 8(c) [1, 4, 5]. By applying experimentally verified PIIL techniques to wavelengths and resources used in state-of-the-art electronics manufacturing, it may be possible to produce periodic patterns with integrated interference-period scale functional elements at the nanometer scale in a single, rapid step.

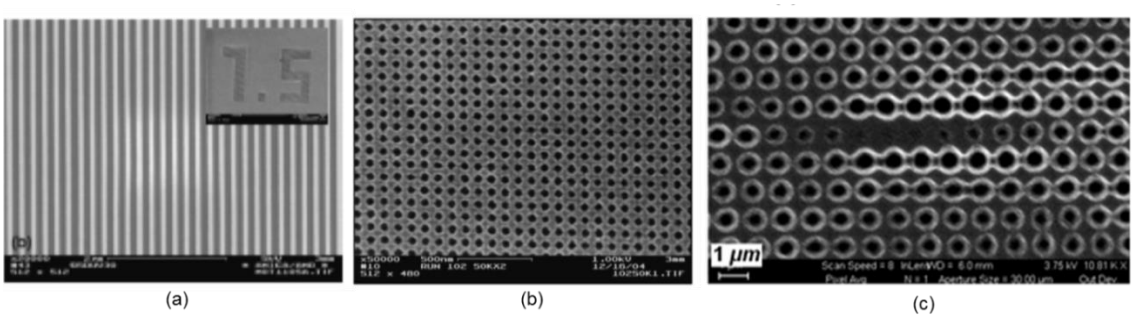

Figure 8: SEM images of (a) 1D IL fabricated structure for triple gate MOSFET, spacing is 150nm [14]; (b) 2D IL fabricated structure using a 157 nm excimer laser; spacing between motifs is 90 nm [11]; and (c) 2D PIIL fabricated structure with a simple waveguide functional element using a 363.8 nm Ar ion laser; spacing between motifs is 1 μm [1].

2.2 Photonic Crystals

Much of the development of in the field of IL has been geared towards the fabrication of photonic crystals [1, 15-24]. With the development of high-speed fiber-optics networks and photonic integrated circuits (PICs), an increasing larger portion of network traffic is being handled in the optical domain [60, 61]. Crucial to meeting the continuing demand for increased bandwidth in these networks are the development of PICs which include multiple functions including polarizers, waveguides, couplers, variable-optical-attenuators, multiplexers/demultiplexers, and switches in a single, integrated device [1, 20, 60-62]. PICs developed for implementation in networks using telecommunications wavelengths require structures fabricated on the nano-scale [1, 20]. While PICs continue

to develop with increased functionality, the fabrication of these devices is expensive and time-consuming which is undesirable for large-volume commercial production.

Currently, there is no established method for the large-scale and cost-effective production of photonic crystal devices [1, 20]. To meet this deficiency, IL can be used as a fast, cost-effective production method for photonic crystals in one, two, and three dimensions as shown in Figure 9 [1, 15, 19-22]. However, as previously stated one of the limits in using IL is that only periodic structures can be generated with an additional technique required for the manufacture of integrated devices. A variety of techniques have been used in conjunction with IL lithography; however, as show in Table 1, only PIIL can meet the requirements of high-volume, cost-effective commercial production of interference-period scale, high spatial frequency integrated elements.

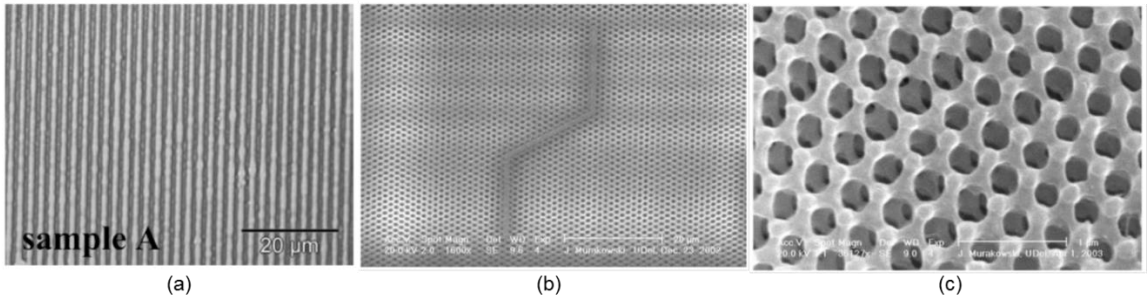

Figure 9: SEM images of (a) 1D [19], (b) 2D, and (c) 3D photonic crystal structures generated using IL. Note that the functional element (waveguide) in (b) is generated by electron-beam lithography [15].

2.3 Biomedical Structures

The development of micro- and nano-scale periodic and semi-periodic structures is of increasing importance to the field of biomedical science [1, 20, 25-30]. To regenerate nerves, arrays of mircochannels are needed to guide growth [1, 20, 28]. For bone regeneration, a series of periodic hydrogel meshes are often used to provide a scaffolding

structure to guide the regrowth process [1, 20, 29]. In forming, maintaining, and controlling tissue growth, periodic microfluidic channels are required to supply nutrients to cells prior to the redevelopment of blood vessels [1, 20, 26, 30].

In all of these applications, a periodic structure is used as a basis or scaffold for guiding the growth of some biological entity and in many applications, IL has been the tool of choice to generate these structures [1, 20]. For example, IL is used to generate a 2D periodic protein array as a scaffold structure to facilitate the growth of murine osteoblast (MC3T3) cells as show in Figure 10(a) [30]. Moreover, IL combined with stop-flow lithography has shown the ability to generate mirco-structured particles, shown in Figure 10(b), that have potential applications for facilitating cell regrowth and fabricating biosensors [1, 20, 26]. Based on the developing nature of biomedical structures and the proven capabilities of IL and by extension PIIL in generating periodic structures, PIIL has the potential to be an enabling technology for the production of low and high volume commercially available biomedical structures.

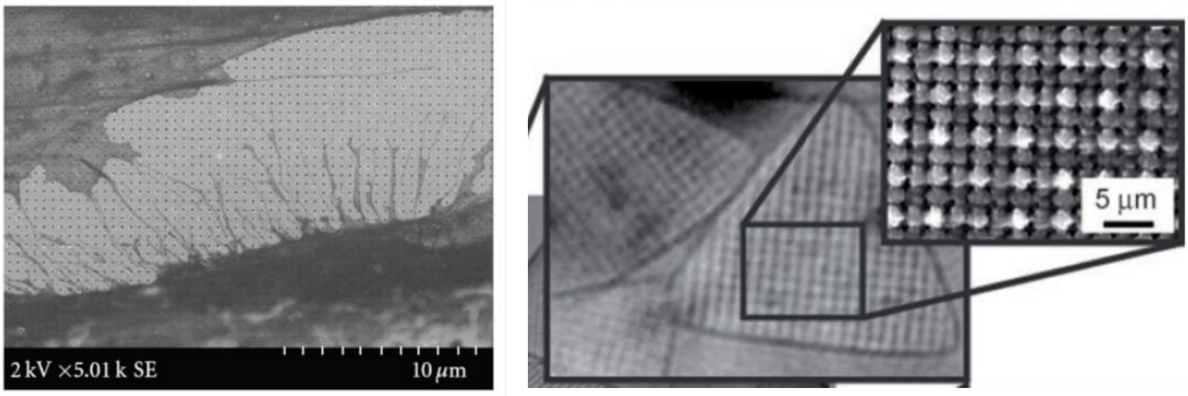

Figure 10: SEM images of (a) 2D protein array generated by IL with MC3T3 cells growing on the structure four hours after seeding [30] and (b) mirco-structured particles generated through a combination of phase-mask IL and stop-flow lithography [1, 20, 26].

CHAPTER 3

PIIL SYSTEM CONFIGURATIONS AND IMPACT

Pattern-Integrated Interference (PII) can be thought of as a logical progression of the field of interference as depicted in Figure 11 [6]. In conventional interference, two or more waves interact to produce interference fringes based on the orientation and magnitudes of the wavevectors, polarizations, and amplitudes of each component wave as shown in Figure 11(a) [1, 6, 35]. Building on interference, conventional holography is conceptually equivalent to a system with interference between an off-axis reference wave and a subject wave as shown in Figure 11(b) [6]. Following this progression, PII is the combination of waves that have joint reference and subject roles [6]. These reference/subject waves can be generated and recorded in photosensitive materials through a variety of single-optical-axis (SOA) and multiple-optical-axis (MOA) PIIL system configurations. These systems allow for rapid prototyping and the potential for high volume commercial production with the inclusion of a diffractive photomask [1, 4, 6].

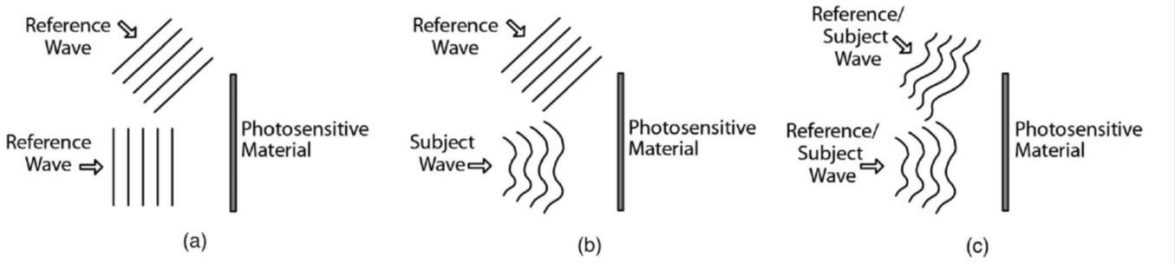

Figure 11: (a) Conventional interference as the superposition of two, three, or more waves. (b) Conventional holography as the interference of a subject wave with a reference wave. (c) PII as the superposition of two, three, or more reference/subject waves. The resulting patterns are typically recorded in a photosensitive material [6].

3.1 Single-Optical-Axis PIIL Systems

The PIIL system configuration employing the fewest optical elements is a single-optical-axis (SOA) system shown in Figure 12 [6]. This system will be referred to as a "basic SOA PIIL system." Only two beams are shown for simplicity but in principle there could be three, four, or many more beams in this system. In this configuration, a series of suitably coherent sources, normally from a laser, are expanded to approximately the size of the mask and then condensed through a single lens and passed through a single photomask [6]. A single objective lens is then used to image the mask element onto the photosensitive material. If the mask is blank, the unperturbed interference pattern is formed; however, if there is a mask element as shown in Figure 12, the element is imaged onto the photosensitive material. The formation of the mask image will largely eliminate the intensity of the corresponding periodic elements resulting in a custom-modified interference pattern [6]. The rays in Figure 12 correspond to a blank mask pattern [6].

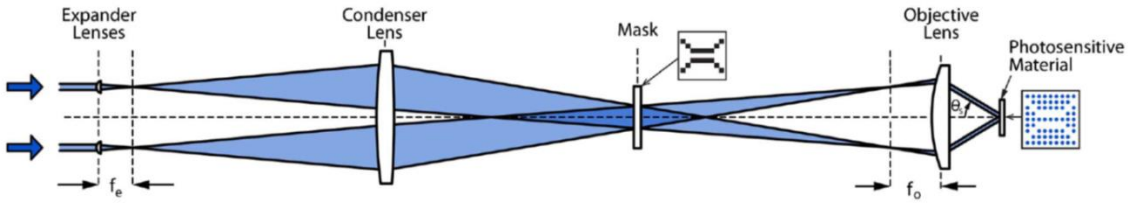

Figure 12: Basic SOA PIIL system configuration. A single photomask, condenser lens, and objective lens are employed for all beams. The blocking elements in the mask are identical for all beams [6].

A slightly more complicated SOA PIIL system employing a set of two objective lenses is shown in Figure 13. This is referred to in the literature as a "single-optical-axis Fourier–transform PIIL system" [6]. This is because the imaging subsystem, which starts at the photomask and ends at the photosensitive material, consists of two lenses in a Fourier transform configuration [6, 63]. This system differs from the basic SOA PIIL

system in that the beams incident on the single photomask are collimated. The double-objective lens system then focuses and re-collimates each beam so that they converge to the same location on the photosensitive material. Because the objective lens system is in a Fourier–transform configuration, individual off-axis collimated beams produce displaced Fourier transforms of the amplitude transmittance of the photomask which are then imaged onto the photosensitive material by the second objective lens of the imaging subsystem [6, 63]. Because of the configuration, spatial filters may be inserted into the Fourier plane of each beam to enhance system performance as shown in Figure 12. This system configuration was employed in the prototype system that first experimentally verified PIIL [1, 4, 5].

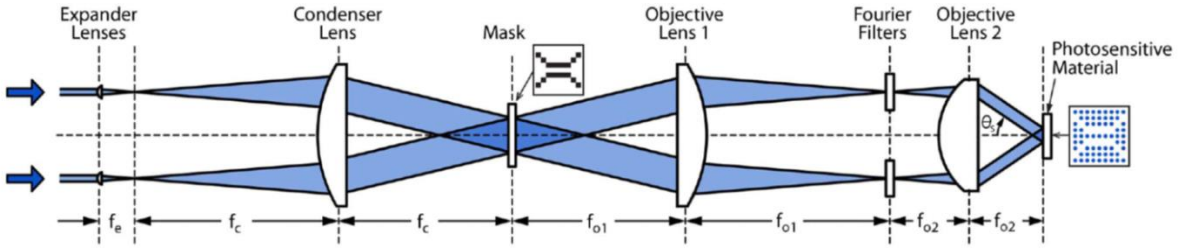

Figure 13: SOA Fourier–transform PIIL system configuration. A single double-objective lens system and a single mask are employed for all beams [6].

These two SOA configuration types represent the two main subclasses of a SOA PIIL system with the primary distinction between them involving the configuration of the imaging subsystem. For a more purpose-specific system, the single objective lens shown in Figure 12 could conceivably consist of a lens system designed to improve the imaging properties of the system but would remain classified a basic SOA PIIL system. Similarly, the first and second objective lens shown in Figure 13 could each be composed of an entire lens set to enhance performance while still remaining in a Fourier transform configuration.

3.2 Multiple-Optical-Axis PIIL Systems

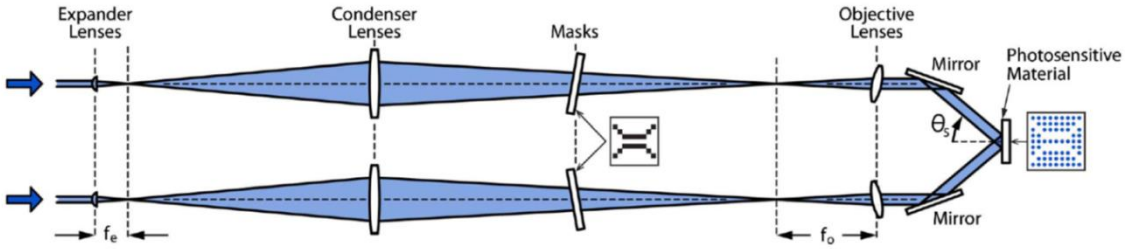

Figure 14: Basic MOA PIIL system configuration. The optical elements in each axis may be the same or differ [6]. The insertion of mirrors after each axis's objective lens ensures that the mask from each axis is imaged in the same plane.

While SOA PIIL systems employ fewer optical elements and are generally easier to construct with limited resources, PII systems in general may be multiple-optical-axis systems [1, 6]. Visually analogous to the basic SOA PIIL system configuration, a basic MOA PIIL system configuration is depicted in Figure 14 with a separate set of optical elements accommodating each beam. Each set of optical elements may be the same or differ for each axis [6]. This system will likewise image the mask elements for each axis onto the photosensitive material and attenuate the corresponding periodic elements resulting in a custom-modified interference pattern. A significant difference with this configuration is that the beams from the multiple axes must be directed towards the photosensitive material with mirrors and are inherently not normal to the plane of the photosensitive material [6]. This requires that the elements in the imaging subsystem be tilted to ensure that the image of each mask lies in the plane of the photosensitive material with uniform magnification while avoiding keystone distortion [6, 55]. For an angle of incidence, θ_s, onto the photosensitive material, the masks and objective lenses for each axis must be tilted at an angle of θ_s while the mirror must be tilted by $\theta_s/2$ in the opposite direction [6].

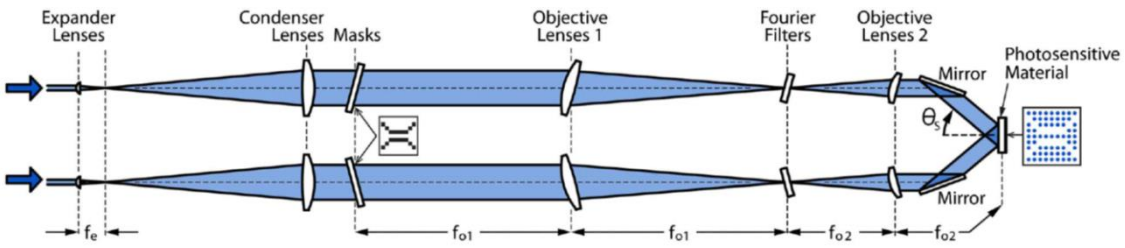

Figure 15: MOA Fourier–transform PIIL system configuration. A double-objective lens imaging subsystem in a Fourier–transform configuration is employed in each optical axis [6].

Continuing the analogy with SOA PIIL system configurations, it is possible to modify the basic MOA system configuration into an MOA Fourier–transform PIIL system configurations as shown in Figure 15. This configuration is similar to the basic MOA PIIL system configuration but employs a double-objective lens imaging subsystem in a Fourier–transform configuration in each optical axis. Analogous to the SOA case, this MOA PIIL system configuration requires that the beams incident on each photomask are collimated. Each double-objective lens system then focuses and re-collimates each beam so that they converge to the same location on the photosensitive material. Note that each element of each imaging subsystem must be tilted in the same manner as the basic MOA configuration to ensure all mask images are in focus at the image plane with uniform magnification [6, 55]. Because each objective lens system is in a Fourier–transform configuration, individual off-axis collimated beams produce displaced Fourier transforms of the amplitude transmittance of the photomask which are then imaged onto the photosensitive material by the second objective lens of each imaging subsystem [6]. Once again, this system will also image the mask elements for each axis onto the photosensitive material and attenuate the corresponding periodic elements resulting in a custom-modified interference pattern. Additionally, because of the Fourier–transform

configuration, spatial filters may be inserted into the Fourier plane of each beam to enhance system performance as shown in Figure 15 [6].

A variation on these two MOA PIIL system configurations is to remove the mirrors for each axis and rearrange each axis as shown in Figure 16 for the MOA Fourier–transform PIIL system configuration. Assuming minimal loss and perturbations from each mirror, this system configuration will yield the exact performance as an MOA PIIL with mirrors as the mirror only performs a geometric transformation. This system configuration provides better insight into how an MOA PIIL system functions. This configuration highlights that the mask element as well as the imaging subsystem components from each axis are oriented in the same plane but are axially displaced from each other. This verifies that all MOA PIIL cases correspond to the problem of perspective control (off-axis distortionless imaging). AN MOA PIIL with mirrors appears to correspond to on-axis tilted-object imaging; however, this first impression ignores the geometric translation performed by each mirror which ensures that the imaging of such a system is performed in the same manner as an MOA PIIL system without mirrors. As shown in Figure 16, an MOA configuration without mirrors requires more space to implement than a system configured with mirrors. Additionally, the spacing associated with the final objective lens element in each axis may necessitate the construction of a segmented lens for proper alignment as shown in Figure 17 for an MOA Fourier–transform PIIL system configuration constructed to scale.

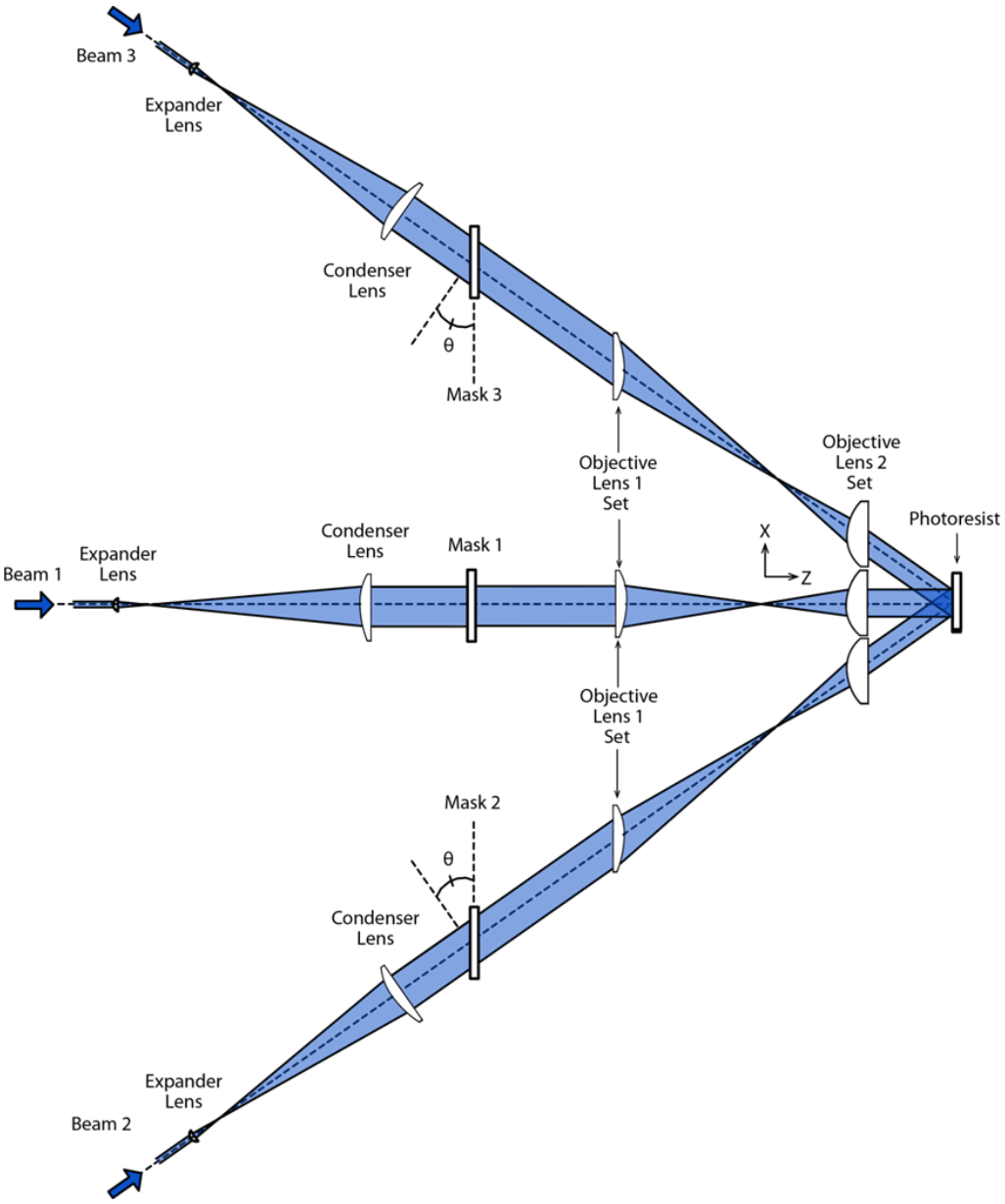

Figure 16: MOA Fourier–transform PIIL system configuration without mirrors concept diagram. The axis corresponding to beam 1 lies in the YZ plane out of the page. The remaining two axes lie in the XZ plane.

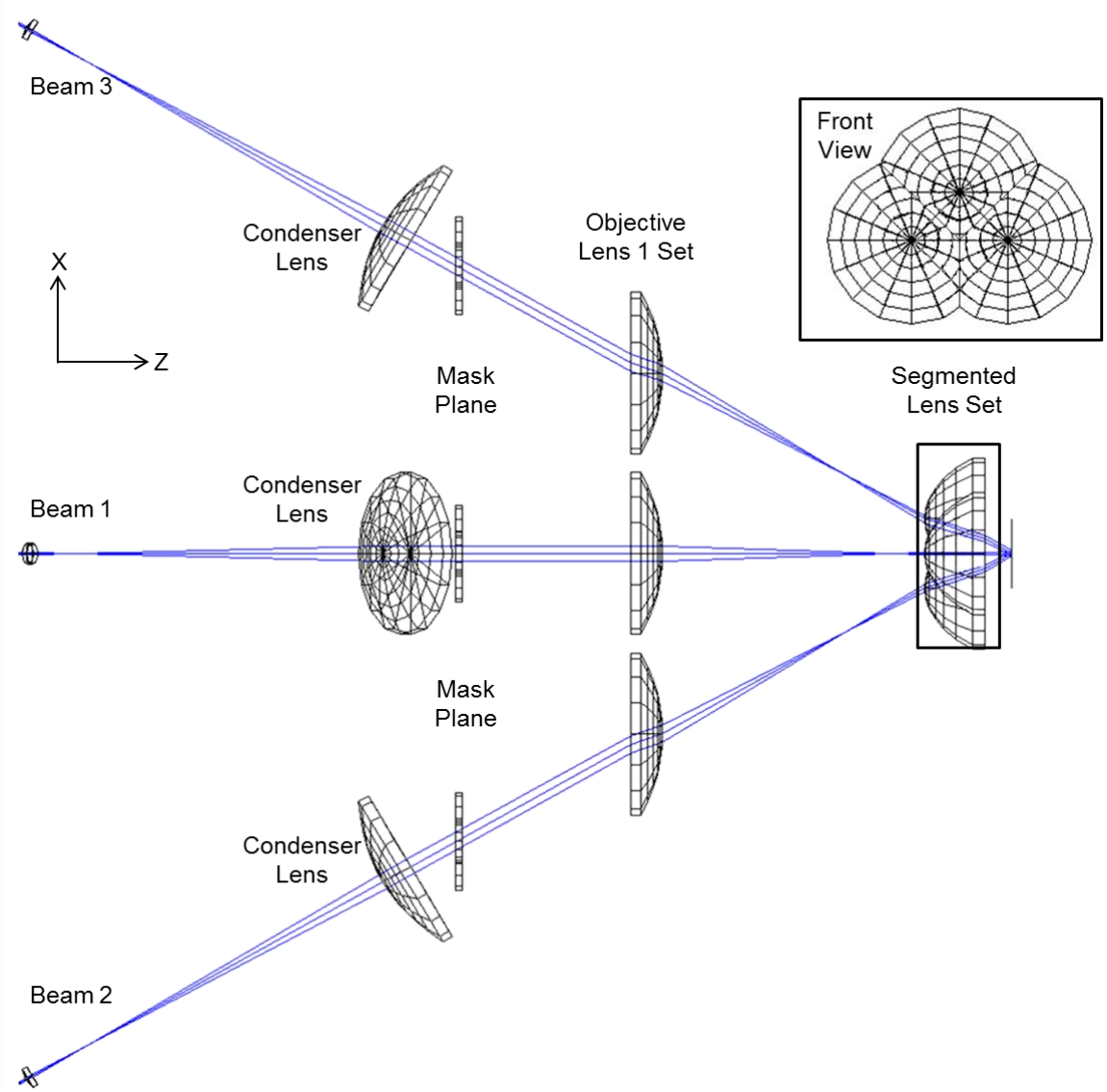

Figure 17: MOA Fourier–transform PIIL system configuration without mirrors. This diagram was constructed to scale using ZEMAX optical design software.

3.3 Comparison of Configurations

Each of these different system configurations has their respective advantages and disadvantages. While SOA system configurations have fewer elements and are simpler to configure, MOA system configurations offer more degrees of freedom to exploit. The angle of incidence onto the image plane of the photosensitive material that is possible in a SOA configuration is limited by the physical size of the optical elements used. In an

MOA configuration, the tilt or separation (corresponding the configurations with and without mirrors) of the optical elements determines the angle of incidence and can therefore achieve higher angles of incidence which generate smaller periodicities with practical-sized optical elements. Since each axis is only accommodating a single beam, the optical elements in an MOA configuration may be significantly smaller than an SOA configuration. Additionally, while a single mask in an SOA configuration is easier to align and less sensitive to adjustments, an MOA configuration involves multiple masks which can generate a wider variety of selectively modified interference motifs [6, 8, 9]. These additional degrees of freedom afforded in an MOA configuration come at the cost of an increased complexity in alignment as compared to an SOA configuration.

In comparing a basic objective lens imaging subsystem with a Fourier–transform double-objective lens system, while basic lens imaging configuration is simple to implement, the double-objective lens subsystems offers many advantages. Firstly, the double-objective lens system allows for the possibility of spatial filtering in the Fourier plane of the subsystem to enhance image quality [6, 8, 9]. Additionally, the double-objective lens allows for a larger demagnification factor in a more compact structure to image smaller elements when compared to a single objective lens configuration [6]. Lastly, double-objective lens systems in a Fourier–transform configuration have larger image-side NA allowing for higher resolution imaging [6].

3.4 PIIL Impact

These PIIL configurations present the opportunity for rapid prototyping with the use of commercially available components. As an example, the prototype SOA Fourier–

transform PIIES depicted in Figures 2 and 13 was constructed with components from ThorLabs and, once a procedure was established, could be assembled and aligned on an optical bench within 12-18 hours [1, 4, 5]. However, because these configurations are free-space interferometers, they are subject to interferometric stability issues associated with the use of discrete optoelectronic components and are ill-suited to meet large volume production requirements [6]. To have a potential impact on large-volume production, the recording of a diffractive photomask (DPM) as shown in Figure 18 has been proposed [1, 3, 4, 6, 64, 65].

A DPM is a common path interferometer that is substantially more stable and durable than the free-space interferometer PIIL system configurations [6]. As shown in Figure 18(a), the DPM recording procedure is shown for a SOA Fourier Transform PIIL configuration. First, the DPM is inserted between the second objective lens and the image plane of the PIIL system [6]. Additionally, a reference beam derived from the same laser source as all the beams is used in the system. This beam is focused in the front focal plane of the second objective lens through the use of an additional lens and a beam splitter [6]. This results in a collimated reference beam emerging from the second objective lens which is incident on the DPM along with the multiple PIIL beams. After holographically recording all of these beams in the DPM, subsequently illuminating the DPM reproduces the original PIIL beams as illustrated in Figure 18(b) [3, 6]. Note that a zero-order blocking element is incorporated into the DPM to ensure that the reference beam does not alter the PII pattern that is produced [1, 3, 6]. Thus, once a PIIL system configuration has been properly aligned to produce a desired pattern, it is possible to record this configuration in a DPM that can be used repeatedly without having to

consider the careful alignment of the original PIIL system. Also note that the DPM does not need to make physical contact with the photosensitive material used for recording which will increase the longevity of use associated with it and corresponding cost savings [6].

Thus, since the various PIIL system configurations can be assembled from commercially available components, they are particularly appropriate for development, prototyping, and modest-volume production [6]. However, for large-volume production, the implementation of a DPM in conjunction with a standard PIIL system configuration is more desirable.

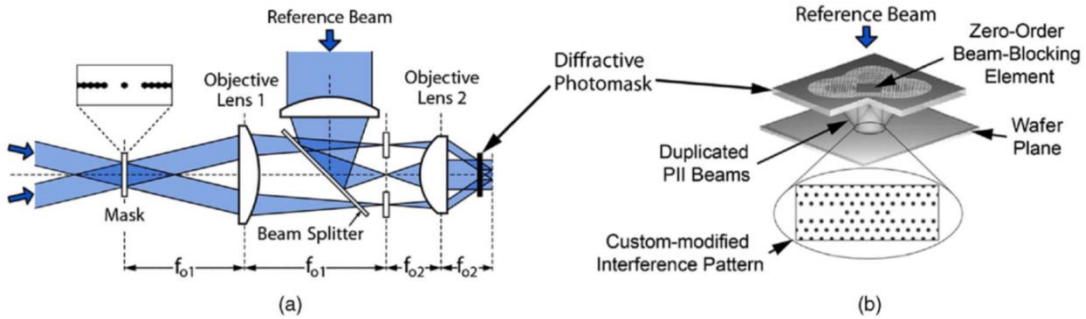

Figure 18: (a) Configuration for recording a diffractive photomask (DPM). In a SOA Fourier–transform PII system, the DPM is placed after the last objective lens and holographically recorded by using an additional reference beam. (b) PII pattern reconstruction. The interfering beams and resulting PII pattern are reproduced by illuminating the DPM with the same reference beam [6].

CHAPTER 4

MOA PIIL SYSTEM CHARACTERIZATION AND OPTIMIZATION

Based on research involving off-axis imaging systems described in Chapter 1, ray optics is used to formulate a characterization model to describe the aberrations that occur in an MOA PIIL system. An MOA Fourier–transform PIIL configuration implemented with single-element, non-optimal lenses that were previously used in the prototype SOA PIIES was the specific case chosen to develop this model [1, 4]. No attempt has been made to start with more appropriate components. The purpose of this approach is to provide a framework in which future purpose-specific lenses can be designed and their performance evaluated. A single axis of this configuration is shown in Figure 19. All axes in this system are specified to be degenerate allowing for the characterization and optimization of a single axis. This modeling technique treats the elements from the mask to the image plane corresponding to the imaging subsystem as depicted in Figure 19. Fourier optics is used to describe diffraction in the optical system which will become significant when simulating system performance.

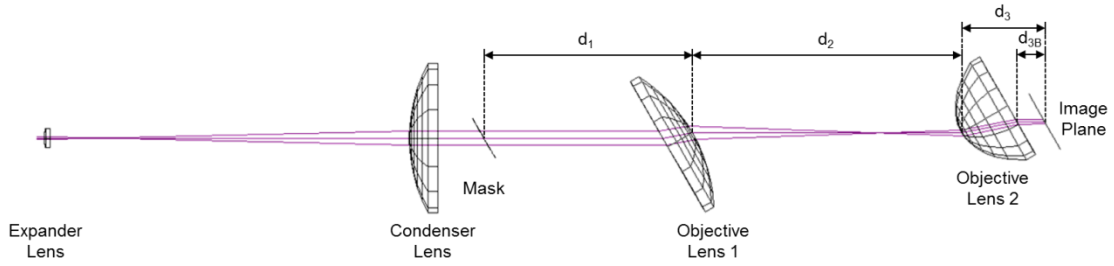

Figure 19: Single axis of an MOA Fourier–transform configured PIIES. Characterization and optimization is performed on the imaging subsystem of the axis which extends from the mask to the image plane.

4.1 Interference/Image Pattern Metrics

Evaluation of the interference/image pattern can be separated into quantities that influence the periodic pattern quality and those that influence the mask image quality. For periodic pattern quality, the collimation of incident beams is the primary metric to be optimized. For mask image quality, the ray spot diagram of incident beams is the primary metric to be optimized.

In order to maintain a uniform periodic structure throughout an interference pattern, the wavevector configuration of incident beams needs to remain constant across the exposure field. This is achieved when each beam is collimated. Additionally, for high contrast between constructive and destructive interference, it is required for the interfering beams to have equal intensity and their polarizations properly aligned. Therefore, when analyzing each optical axis, the degree to which the beam incident on the image plane is collimated provides an indicator of how uniform and high-contrast the interference pattern will be assuming the individual beam intensities and polarizations are suitably controlled.

A measurement of the quality of performance of any optical imaging system can be described by the aberrations that are present in its output. To quantify these aberrations, an analysis of the ray spot diagram of each incident beam is examined. A ray spot diagram generates a series of rays distributed between the chief ray and its marginal rays to determine discretely how an optical imaging system performs. If the initial spot diagram is a series of perfectly concentric circles, as shown in Figure 20(a), then an ideal imaging system will return a proportional series of perfectly concentric circles which are scaled according to the magnification of the system as shown in Figure 20(b). Any

deviation from the original spot diagram would indicate degradation in the performance of the system which can be described in terms of the various aberrations. Chromatic aberrations are ignored for the purposes of this analysis as we assume the sources to be essentially monochromatic. Thus, the degree to which an incident beam's spot diagram is preserved provides an indicator of the system aberrations.

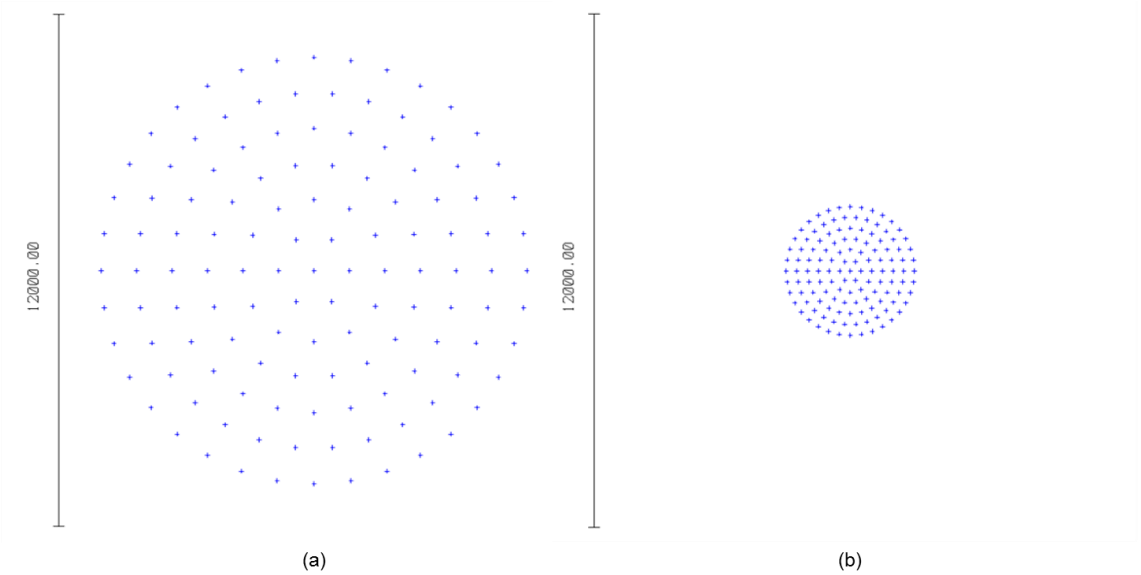

Figure 20: Spot diagrams of concentric circles (a) before entering and (b) after leaving a two-objective lens system with no tilt and magnification of 0.3. The side scale bars indicate a length of 12000 μm (12 mm). Note that the shape of the spot diagram remains unchanged but its size scales with the magnification of the system.

While the ray spot diagram is an indicator of most aberrations the mask pattern will experience as it is imaged, what it does not describe is whether or not that image will be in focus at the image plane. To perform this analysis, it is necessary to observe a point source placed on the mask plane and determine where the rays are focused after passing through the optical imaging system. For an ideal imaging system, all rays from an object point will be focused to a single image point; however, real systems will be subject to

aberrations that will affect this. This description will provide the basis for future designs to correct these types of aberrations in a practical MOA PIIES.

4.2 Optical System Parameters

The optical system parameters to be optimized for the MOA PIIES of this investigation are the distance between the mask plane and the first objective lens, the distance between the two objective lenses, and the distance between the second objective lens and the image plane; denoted as d_1, d_2, and d_3 respectively in Fig. 19.

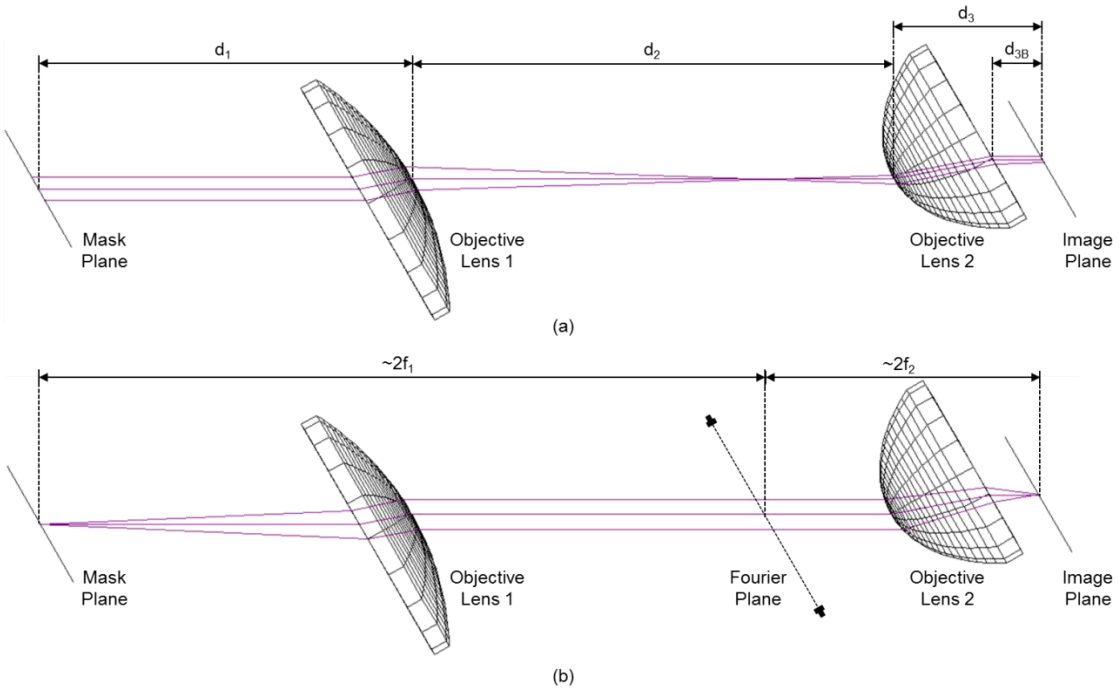

Figure 21: Optimized configuration for 30° tilted imaging system that approximates a 4f optical system with (a) an incident collimated beam and (b) an incident point source at the center of the mask plane.

The imaging portion of the optical system, highlighted in Fig. 21 for a 30° tilted imaging system, was designed as a 4f optical subsystem in a previous SOA PIIES [1, 4-6]. An ideal 4f optical system will focus an incident collimated beam to the objective lens system's Fourier plane and then recollimate the beam according to the magnification

of the objective lens system as indicated in Figure 21(a). Similarly, it will also collimate an incident point source on the mask plane and then focus it back to a point on the image plane as depicted in Figure 21(b). These properties of a 4f optical system produce a collimated beam incident on the image plane whose ray spot diagram is unperturbed. This enables interference and mask image formation. Additionally, a 4f optical system provides a readily accessible method to analyze the spatial frequency content of the mask pattern via Fourier optics. Because the mask patterns to be formed are desired to be on the same scale as the wavelength, the diffraction effect of the mask pattern, which can be described in terms of the spatial frequency content the optical system passes, needs to be included.

While it is not possible to produce an ideal 4f optical system when tilting the single-element, non-optimal lenses, it is desirable to replicate as closely as possible its properties to optimize the performance of an MOA PIIES. The parameter d_1 is adjusted such that a point source on the mask plane, modeled in a ray optics picture, should have all rays as close to collimated as possible as they exit the first objective lens. Correspondingly, d_2 is adjusted such that a collimated, circular beam input into the first objective lens yields a beam that is as close to collimated and circular as possible. Lastly, d_3 is adjusted such that the input into the second objective lens will be focused to a point that lies on the image plane. While this adjustment of the optical system parameters attempts to ensure uniform magnification of the image, it does not specifically address the presence of spherical aberrations which need to be removed to achieve the Abbe sine condition.

4.3 System Characterization Approach

The system characterization approach employs a ray tracing method implemented using ZEMAX optical design software [66]. Because all optical axes are specified to be identical, analysis was performed on a single axis. This analysis treats the elements from the mask to the image plane, depicted in Figure 21, as these are the elements that are tilted and where the aberrations are introduced.

For this characterization, the original two–objective lens imaging system from the previous SOA implementation is used [1, 4, 5]. The first objective lens is a Thorlabs AL100200 aspheric lens with an effective focal length of 200 mm and the second objective lens is a Thorlabs AL7560 aspheric lens with an effective focal length of 60mm. No attempt was made to select optimal lenses as it is only sought to establish a modeling approach for MOA systems; these particular lenses were merely used in a previous prototype SOA PIIES [1, 4]. All lens characteristics, including the aspheric lens data, were included in the simulation model. Primary analysis was performed using λ = 363.8 nm (argon-ion laser). Additional analysis was performed at λ = 780 nm, the design wavelength of the ThorLabs optics, to determine if there was a significant difference in performance by changing wavelengths.

The distance between the mask plane and objective lens 1, d_1, was optimized for various lens system tilts from 0° to 45° in 5° intervals. This was performed by tracing rays from a point source at the center of the mask plane and calculating the value of d_1 that yields the most collimated output described by least mean squared deviation in the angle of the rays exiting objective lens 1. A description of the specific merit function for d_1 is provided in Appendix A.

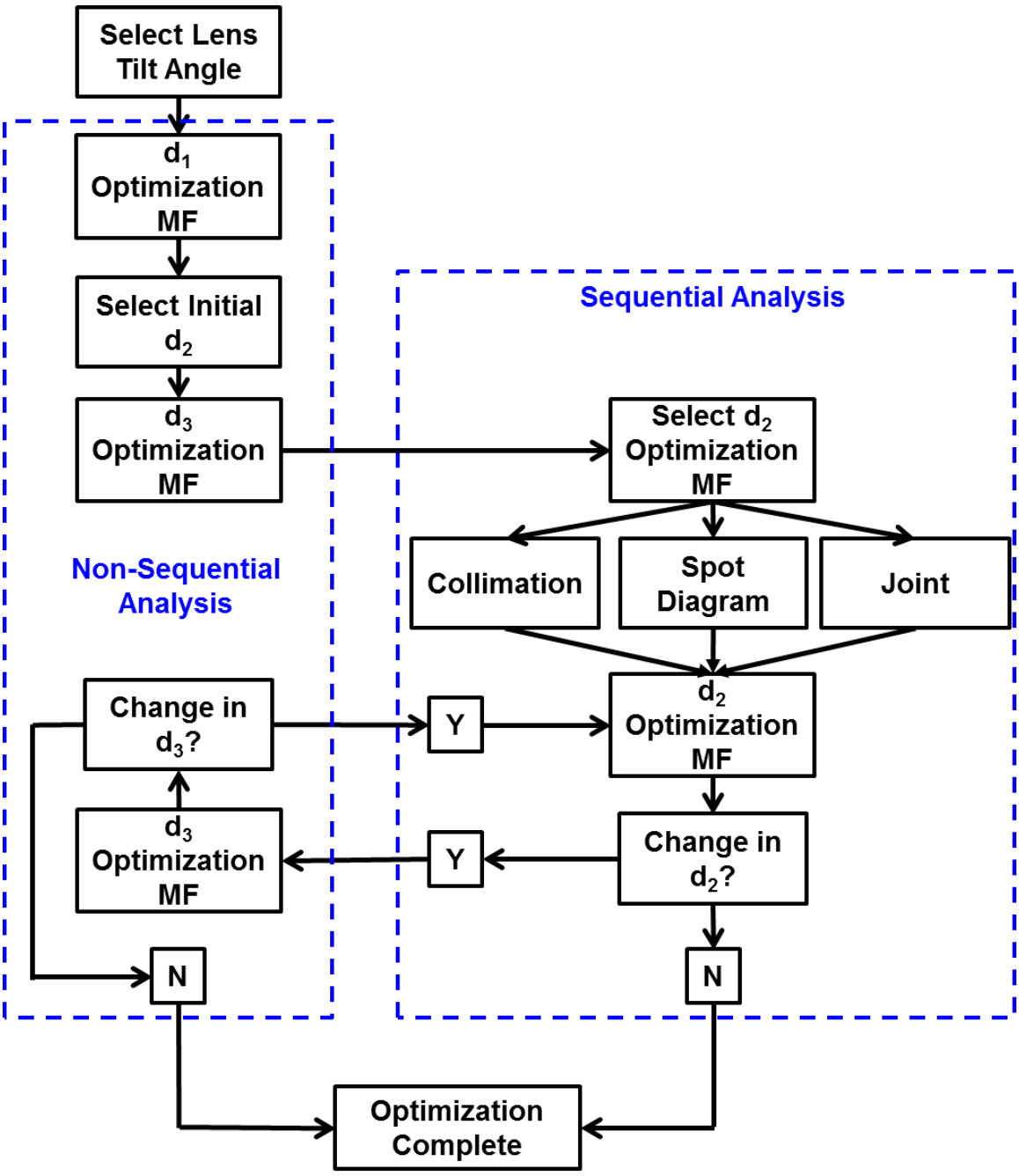

Figure 22: Block diagram of the process to optimize d_1, d_2, and d_3.

Following this, the distance between objective lenses, d_2, was adjusted for various lens system tilts from 0° to 45° in 5° intervals to obtain the minimum beam divergence as well as the configuration that produced the minimum deviation in the spot pattern. The values for d_2 for these cases were obtained using two separate merit functions that

minimized the root mean square deviation of these quantities. A third merit function, combining these two merit functions, was also used to create a joint optimization. All three merit functions used for d_2 are described in detail in Appendix A. Note that for each value of d_2, the distance between the second objective lens and the image plane, d_3, is optimized. This optimization is necessary because the output of the objective lens system is not symmetric for tilted lenses, meaning that changing the distance from the second objective lens to the image plane will affect the optimized value of objective lens spacing. Moreover, the value of d_3 needs to be optimized for a given value of d_2 because the spacing of the objective lens will affect where the mask pattern is imaged. By assuming an arbitrary but reasonable starting value for d_3, the values of d_2 and d_3 are iteratively calculated until their values converge. The specific merit function for d_3 is given in Appendix A. A block diagram of the entire optimization procedure is shown in Figure 22.

4.4 Characterization and Optimization Results

4.4.1 λ = 363.8 nm (Argon-ion laser)

In the case of optimum collimation (minimized beam divergence), beam divergence for marginal rays along the Y-axis, θ_{YM}, is confined to be less than 0.5° for tilt angles less than 35° with divergence beginning to increase noticeably to 1° and 2° for 40° and 45° tilts respectively as indicated in Figure 22(a). However, for these configurations of objective lens spacing, the spot diagram displacement of the beam increases steadily as tilt angle is increased. The spot diagram displacement, ΔD, is defined here as the difference between the marginal ray distance from the chief ray for the Y-axis or the X-

axis marginal rays divided by the unperturbed X-axis marginal ray distance expressed as a percentage. For tilt angles less than 30°, the maximum spot diagram displacement, ΔD_{max}, remains below 25% but increases sharply above that tilt as indicated in Figure 22(b). Analysis of the spot diagram of the 45° tilt case in ZEMAX shows significant astigmatism along the Y-axis as shown in Figure 24. For the case of minimized spot diagram displacement, ΔD_{max} remains under 12% for tilt angles below 30°. For angles of tilt beyond 30°, ΔD_{max} increases as indicated in Figure 22(b) with 80% spot diagram displacement for a 45° tilt. An analysis of the spot diagram for the 45° tilt case again shows astigmatism as the primary aberration, although not as severe as in the optimum collimation case; however, coma becomes a concern as indicated in Figure 24. The beam divergence for the optimized spot diagram displacement case remains under 0.5° for tilt angles less than 15° but then begins to increase dramatically to 4° for a tilt of 30° and over 20° divergence for a tilt of 45° as shown in Figure 22(a).

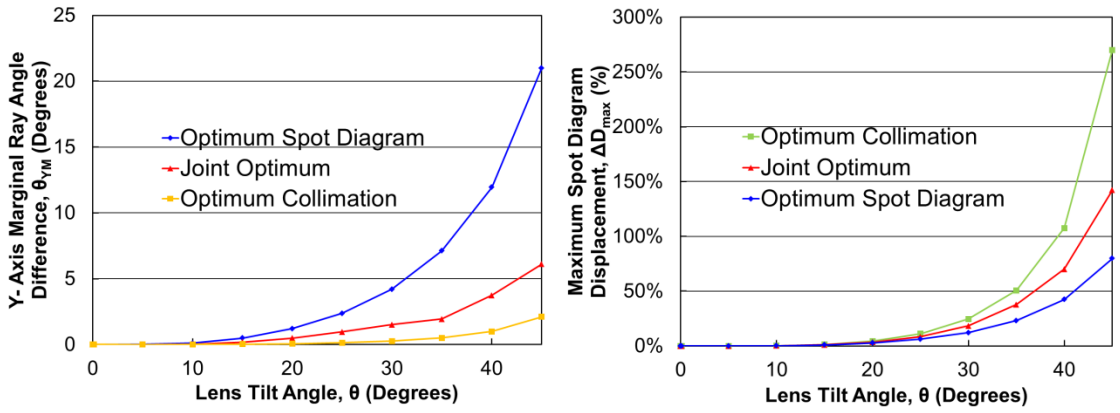

(a) (b)

Figure 23: Plots of (a) beam divergence and (b) maximum spot diagram displacement vs tilt angle, θ, of the two-objective lens system for λ = 363.8 nm (argon-ion laser).

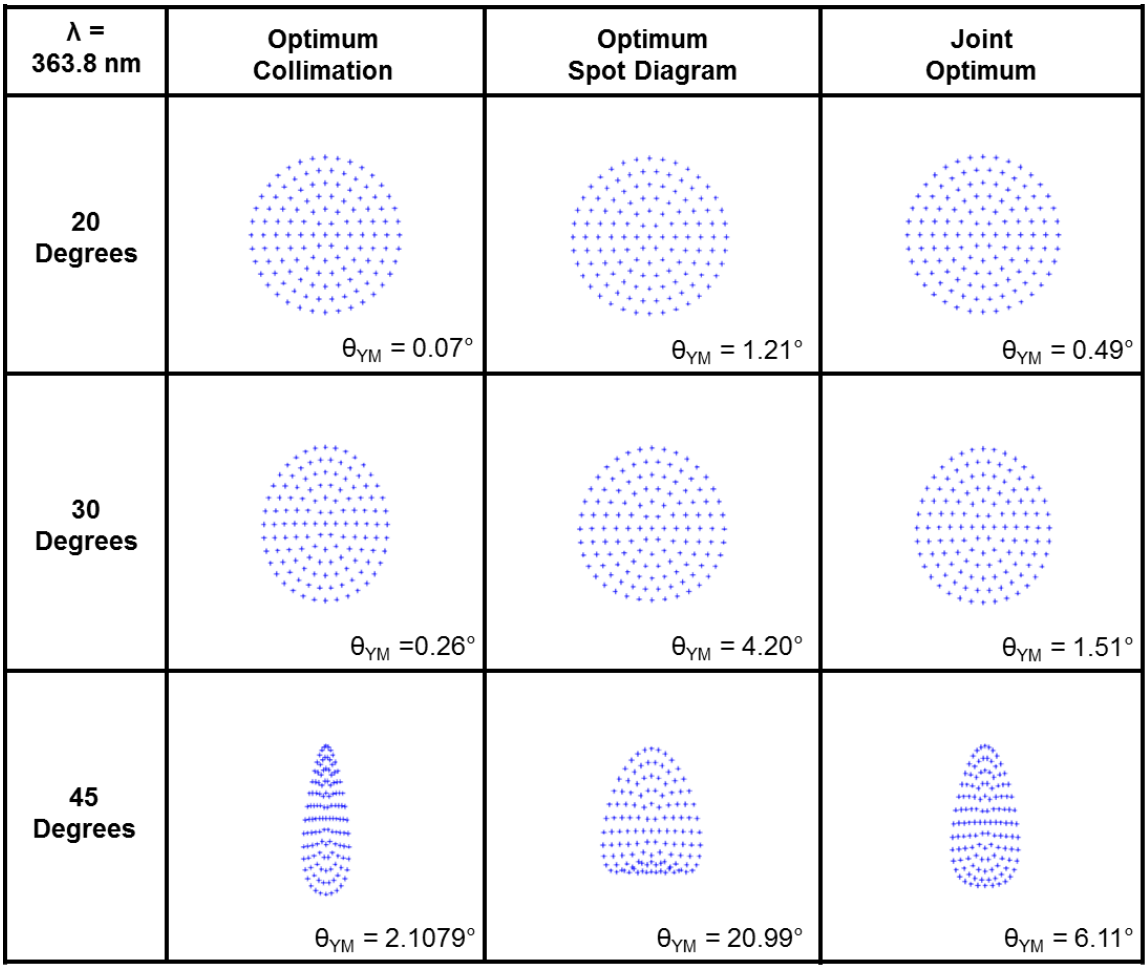

Figure 24: Spot diagrams at the image plane for optimum collimation, optimum spot diagram, and joint optimum cases corresponding to 20°, 30°, and 45° tilts for λ = 363.8 nm (argon-ion laser). Values for θ_{YM} corresponding to each spot diagram are annotated.

The joint optimization case, which considers both divergence and spot pattern displacement, maintains less than 1.5° of beam divergence and less than 20% maximum spot diagram displacement for tilt angles up to 30° as shown in Figures 22(a) and (b). Beyond 30°, beam divergence and spot diagram displacement begin to rise noticeably with beam divergence rising to 6° and spot diagram displacement rising to 140% for the 45° tilt case. The spot diagram for the 45° joint optimum case exhibits moderate astigmatism. Spot diagrams for optimum collimation, optimum spot diagram, and joint optimum cases corresponding to 20°, 30°, and 45° tilts are shown in Figure 23.

In all cases, the spacing between the mask plane and the first objective lens, the two objective lenses, and the second objective lens and the image plane (d_1, d_2, and d_3 respectively) decreases as lens tilt angle increases. The results for the joint optimization case is bounded between the values of d_1, d_2, and d_3 for the cases of independent beam divergence and spot diagram optimization as indicated in Figures 24(a)-(c). Thus, the optimization of collimation and image quality individually produce generally similar requirements on the optical system. The large amounts of divergence and displacement in the spot pattern that occur with higher angles of tilt indicate that a more purpose-specific optical system would be needed to correct these effects further for larger tilt angles.

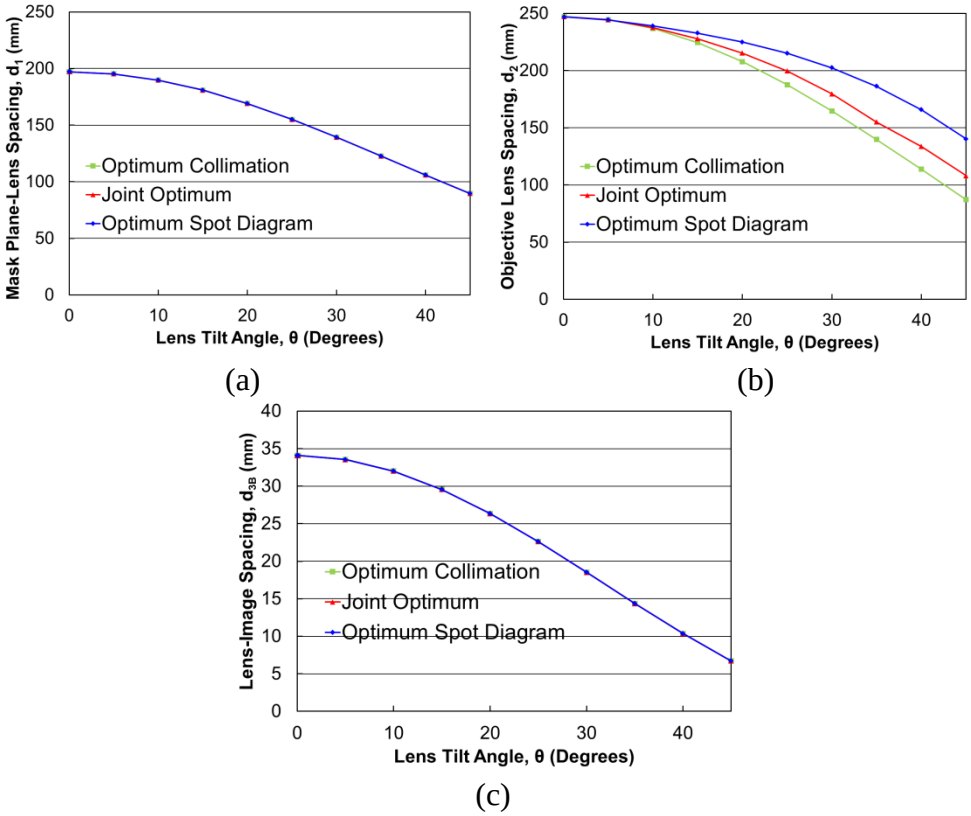

Figure 25: Plots of (a) mask plane-objective lens system spacing (d_1), (b) objective lens spacing (d_2), and (c) objective lens-image plane spacing (d_{3B}) vs tilt angle, θ, of the lens system for $\lambda = 363.8$ nm (argon-ion laser).

4.4.2 λ = 780 nm (Optics design wavelength)

In the case of optimum collimation (minimized beam divergence), beam divergence for marginal rays along the Y-axis, θ_{YM}, is confined to be less than 0.5° for tilt angles less than 35° with divergence beginning to increase noticeably to 0.92° and 1.94° for 40° and 45° tilts respectively as indicated in Figure 26(a). However, for these configurations of objective lens spacing, the spot diagram displacement of the beam increases steadily as tilt angle is increased. For tilt angles less than 30°, the maximum spot diagram displacement, ΔD_{max}, remains below 25% but increases sharply above that tilt as indicated in Figure 24(b). Analysis of the spot diagram of the 45° tilt case in ZEMAX shows significant astigmatism along the Y-axis as shown in Figure 27. For the case of minimized spot diagram displacement, ΔD_{max} remains under 12% for tilt angles below 30°. For angles of tilt beyond 30°, ΔD_{max} increases as indicated in Figure 26(b) with 84% spot diagram displacement for a 45° tilt. An analysis of the spot diagram for the 45° tilt case again shows astigmatism as the primary aberration, although not as severe as in the optimum collimation case; however, coma becomes a concern as indicated in Figure 27. The beam divergence for the optimized spot diagram displacement case remains under 0.5° for tilt angles less than 15° but then begins to increase dramatically to 4° for a tilt of 35° and over 15° divergence for a tilt of 45° as shown in Figure 26(a).

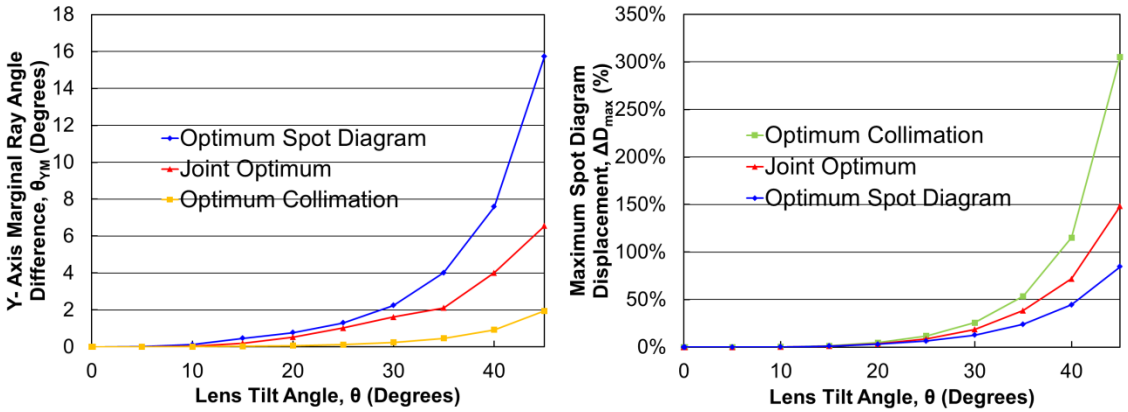

(a) (b)

Figure 26: Plots of (a) beam divergence and (b) maximum spot diagram displacement vs tilt angle, θ, of the two-objective lens system for λ = 780 nm (design wavelength).

λ = 780 nm	Optimum Collimation	Optimum Spot Diagram	Joint Optimum
20 Degrees	θ_{YM} = 0.06°	θ_{YM} = 0.77°	θ_{YM} = 0.53°
30 Degrees	θ_{YM} =0.24°	θ_{YM} = 2.24°	θ_{YM} = 1.61°
45 Degrees	θ_{YM} = 1.95°	θ_{YM} = 15.73°	θ_{YM} = 6.55°

Figure 27: Spot diagrams at the image plane for optimum collimation, optimum spot diagram, and joint optimum cases corresponding to 20°, 30°, and 45° tilts for λ = 780 nm (design wavelength). Values for θ_{YM} corresponding to each spot diagram are annotated.

The joint optimization case, which considers both divergence and spot pattern displacement, maintains less than 1.6° of beam divergence and less than 19% maximum spot diagram displacement for tilt angles up to 30° as shown in Figures 26(a) and (b). Beyond 30°, beam divergence and spot diagram displacement begin to rise noticeably with beam divergence rising to 6.5° and spot diagram displacement rising to 148% for the 45° tilt case. The spot diagram for the 45° joint optimum case exhibits moderate astigmatism. Spot diagrams for all the optimizations corresponding to 20°, 30°, and 45° tilts are shown in Figure 27.

In all cases, the spacing between the mask plane and the first objective lens, the two objective lenses, and the second objective lens and the image plane (d_1, d_2, and d_3 respectively) decreases as lens tilt angle increases. The results for the joint optimization case is bounded between the values of d_1, d_2, and d_3 for the cases of independent beam divergence and spot diagram optimization as indicated in Figures 25(a)-(c). Thus, the optimization of collimation and image quality individually produce generally similar requirements on the optical system. The large amounts of divergence and displacement in the spot pattern that occur with higher angles of tilt indicate that a more purpose-specific optical system would be needed to correct these effects further for larger tilt angles.

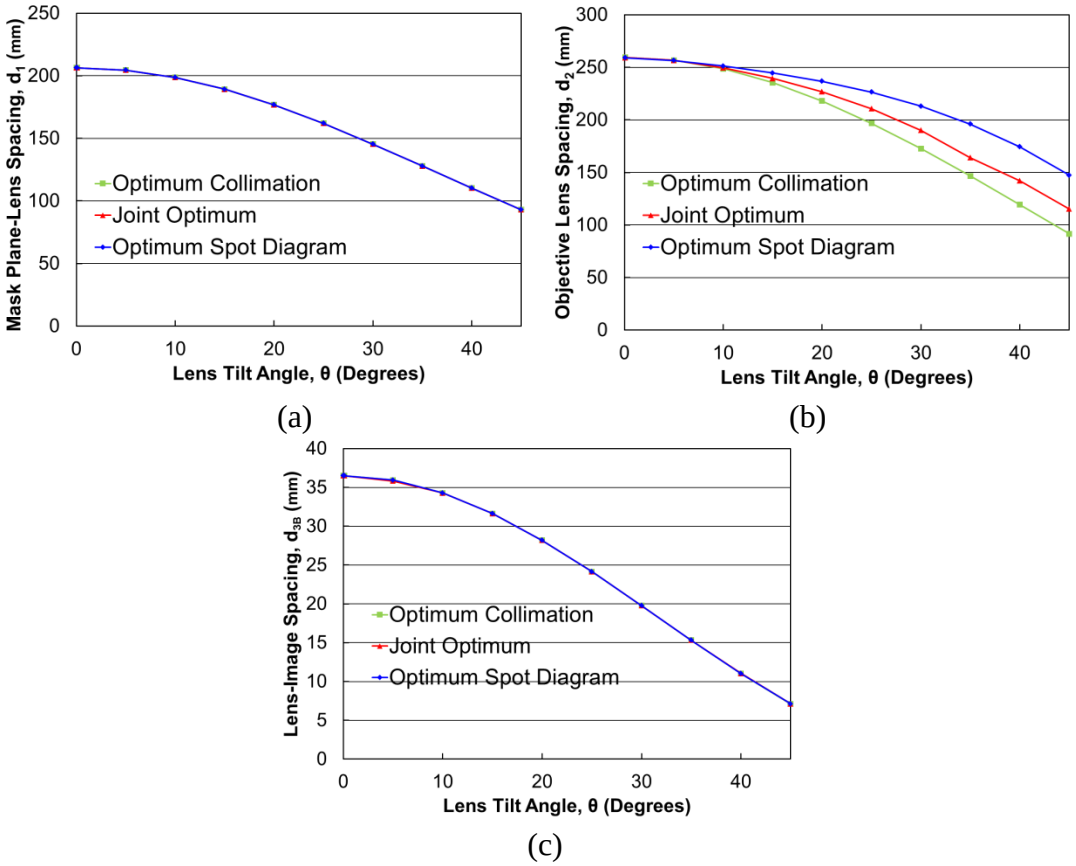

Figure 28: Plots of (a) mask plane-objective lens system spacing (d_1), (b) objective lens spacing (d_2), and (c) objective lens-image plane spacing (d_{3B}) vs tilt angle, θ, of the lens system for $\lambda = 780$ nm (design wavelength).

4.4.3 Comparison

Examining the spot diagrams in Figures 24 and 27, the optimization results for $\lambda = 363.8$ nm and $\lambda = 780$ nm are almost indistinguishable in terms of corresponding diagrams. In examining the exact numbers associated with each case as shown in Figures 23, 25, 26, and 28, the optical system demonstrates similar behavior when optimized for each wavelength. While exact numbers for θ_{YM} and ΔD_{max} vary slightly between each wavelength, there is no appreciable change in the behavior of the system. Similarly, while values for d_1, d_2, and d_3 are slightly shifted between each case, they exhibit similar behavior for both wavelengths. This indicates that if an MOA PIIL system is designed

for a specific tilt that they system may be able to function for a range of wavelengths by slightly adjusting the spacing between the optical components of the system.

CHAPTER 5

MOA PIIL SYSTEM SIMULATION METHOD

While the characterization analysis of an MOA PIIES provides a very quantitative assessment of system performance, it does not provide example images for evaluation. To this end, this chapter describes the method for simulating a full MOA Fourier–transform PIIES using a combination of ray tracing and Fourier optics. A three-axis MOA Fourier–transform PIIL configuration without mirrors, shown in Figure 26, is used as the basis for this method with the results of the simulations described in Chapter 6.

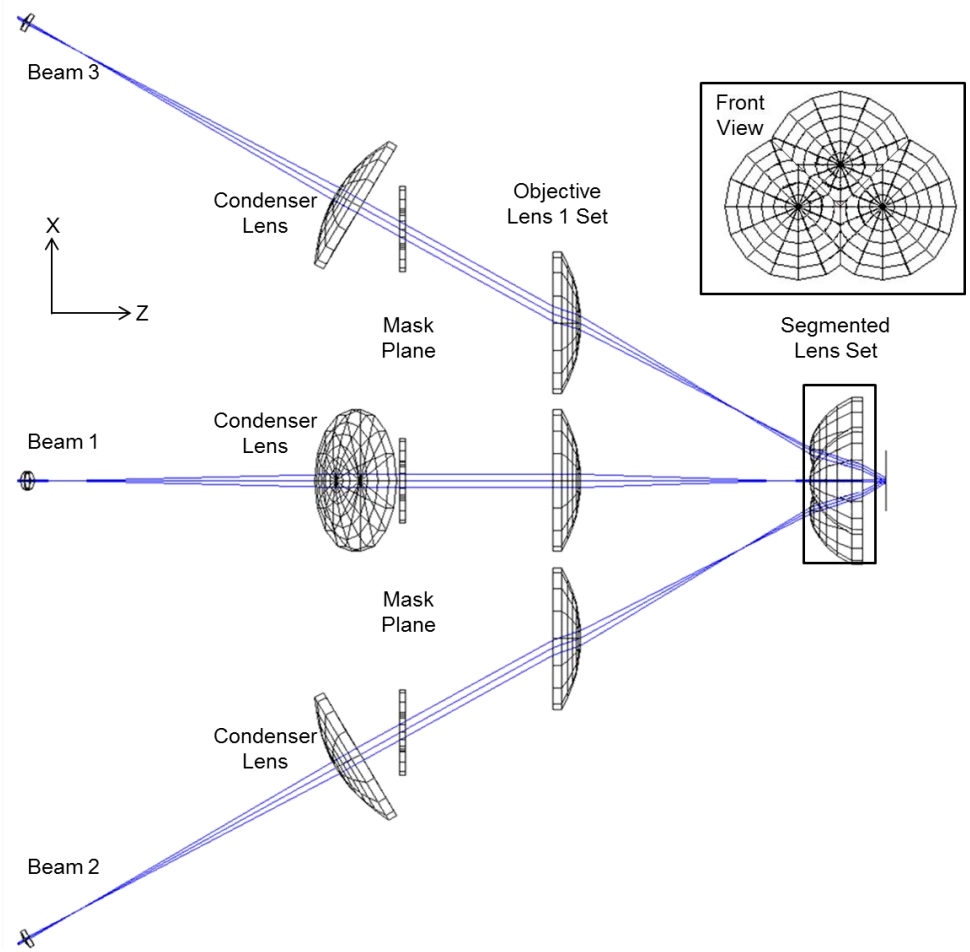

Figure 29: MOA Fourier–transform PIIL system configuration without mirrors.

5.1 Ray Tracing Analysis

To determine the interference pattern produced by an MOA PIIES, ray tracing using ZEMAX optical design software was performed [66]. The advantage of using a ray tracing approach is that it can accurately model the aberrations of the particular optical system used. Ray tracing does not provide an intuitive method for interference calculation; however, due to the fact that ZEMAX can propagate rays with phase and polarization information, it is possible to model interference provided a large number of rays are used. In the specific example of a three-axis MOA PIIES, for a set of three elliptical beams imaged as circular areas that are approximately 6 μm in diameter in the image plane, a simulation of 30,000,000 rays (10M per beam) is used to obtain a high fidelity interference pattern. While ZEMAX does not perform the full interference calculation internally as it cannot accommodate a 3D complex electric field, it can accurately calculate the 3D complex electric field of each ray incident on the image plane and export that data in a binary file format. For the simulations described in Chapter 6, rays were propagated through three identical axes configured for a *p4m* lattice structure. With these data exported to MATLAB, the electric field components of each ray, on a pixel-by-pixel basis, are summed as vectors for all the rays from a single beam that strike a pixel. With total complex field electric field vector, $\boldsymbol{E}$, from each beam calculated for each pixel, the resultant interference pattern intensity, I, is calculated as

$$I = \frac{1}{2}\sum_{i=1}^{3} |\boldsymbol{E_i}|^2 + \mathrm{Re}\{\boldsymbol{E_1}\boldsymbol{E_2}^*\} + \mathrm{Re}\{\boldsymbol{E_1}\boldsymbol{E_3}^*\} + \mathrm{Re}\{\boldsymbol{E_2}\boldsymbol{E_3}^*\} \quad (2)$$

To remove the salt and pepper type noise that occurs from the discrete nature of ray propagation, a median filter is applied to this result. A block diagram picture of this

procedure without a mask is depicted in Figure 34(a). The MATLAB code used to execute this procedure is provided in Appendix B. This ray tracing method can be performed with or without a mask pattern which is modeled as a simple blocking element. This method provides a realistic approximation of what aberrations the mask pattern will incur from the optical system. However, ray tracing does not incorporate the diffraction effect of the mask pattern. Because the mask size is on the same order of magnitude as the wavelength of incident light, these effects cannot be neglected. To include diffraction, a Fourier optics approach is used.

5.2 Fourier Analysis

A 4f optical imaging system, shown in Figure 21, in terms of Fourier optics can be described as the first lens in the system performing a 2D Fourier transform on the object which is imaged as a series of spatial frequency components in the Fourier plane of the system (back focal plane of the first lens) [63]. These spatial frequency components then have an inverse 2D Fourier transform performed on them by the second lens which images the original object in the image plane (back focal plane of the second lens). However, due to the finite aperture of the lenses used in the system, not all of the spatial frequency content is able to be captured. In this context, the second lens of the 4f optical system can be viewed as low-pass filter that only allows spatial frequency content up to a specified value. The radius corresponding to the aperture of the optical system, ρ_0, as shown in Figure 30 is defined as

$$\rho_0 = R \cdot \sin\theta_{Obj} = R \cdot NA \tag{3}$$

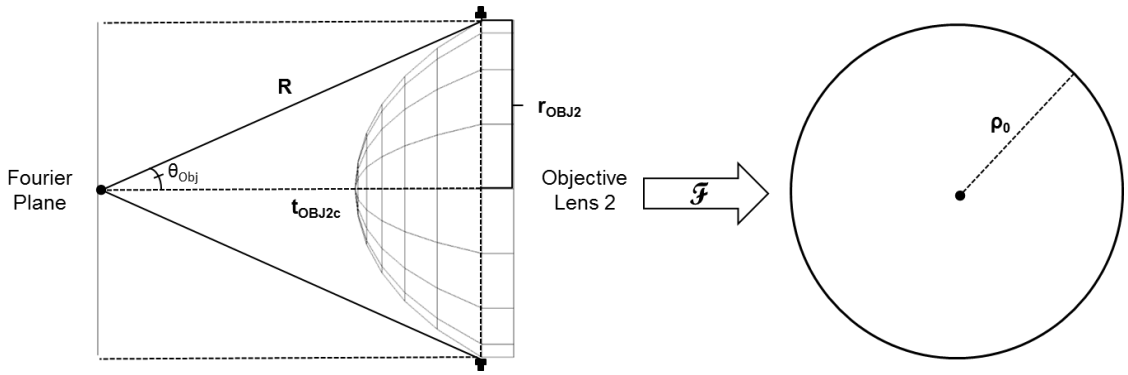

Figure 30: Depiction of the aperture limits of the second objective lens an MOA PIIL.

where R is the radial distance from a point at the object plane to the edge of the aperture of the optical system and NA is the numerical aperture of the system [67]. In the context of the two-objective lens system for this MOA PIIL configuration, the second objective lens provides the limiting aperture for the system such that the NA of that lens can effectively model the NA of the entire system. Using this lens to model the aperture for the system as shown in Figure 30 and assuming a 4f system configuration, R is calculated as

$$R = \sqrt{{t_{OBJ2c}}^2 + {r_{OBJ2}}^2} \tag{4}$$

where t_{OBJ2c} is the thickness of the curved portion of the second objective lens and r_{OBJ2} is the radius of the planar portion of the second objective lens as shown in Figure 30. While these equations will provide the effective aperture of the system in the spatial frequency domain, these results must be properly scaled to the wavelength used. To provide this scale, a square (rectangular) aperture of full width, a, was generated in MATLAB using the same pixel scale as the ZEMAX simulation used to generate the electric fields. The Fraunhofer diffraction pattern from a rectangular aperture corresponds to a 2D Fourier transform of the aperture and is a well-known as a two-

dimensional sinc function squared [63]. Specifically, the distance from the center of the transform to the first zero value in the x-direction, x_f, is given as

$$x_f = \frac{\lambda z}{a/M} = \frac{\lambda f_1}{a/M} \tag{5}$$

where λ is the free-space wavelength of incident light, z is the distance from the transforming element to the Fourier plane, f_1 is the focal length of the first objective lens, a is the full width of the aperture, and M is the magnification of the optical system [63, 67]. Since we know that $z = f_1$, by taking the 2D Fourier transform of the aperture generated in MATLAB (using the fft2 command) and measuring the number of pixels from the center of the transform to the first zero along the x-axis, $\#pix$, a spatial frequency scaling factor, SF, is defined as

$$Scaling\ Factor = SF = \frac{\#pix}{x_f} \tag{6}$$

Thus, the proper size of the aperture, ρ_A, for the two-objective lens system in terms of pixels in the corresponding MATLAB simulation is

$$\rho_A = \rho_0 \cdot SF \tag{7}$$

This description accurately models the diffraction effect of an object imaged by a 4f optical system. For tilted lenses, the imaging portion of the MOA PIIES is not ideally 4f. Because the system is adjusted to mimic the behavior of a 4f optical system as closely as possible, this Fourier optics analysis will provide a good approximation of the diffraction effect of the imaged mask pattern. However, because the both mask plane, Fourier plane, and objective lenses are all tilted, this corresponds to a shift of where the aperture is applied in the Fourier plane as shown in Figure 31. Specifically this offset is equal to

$$Offset = t_{OBJ2c} \cdot \tan\theta \tag{8}$$

as implied by Figure 31 where θ is the tilt of the lens system. Note that for the axes oriented in a *p4m* configuration as shown in Figure 29, the respective offsets for each axis are different based on the relative incidence of each beam with respect to the segmented lens. The correct offsets corresponding to each beam are shown in Figure 32.

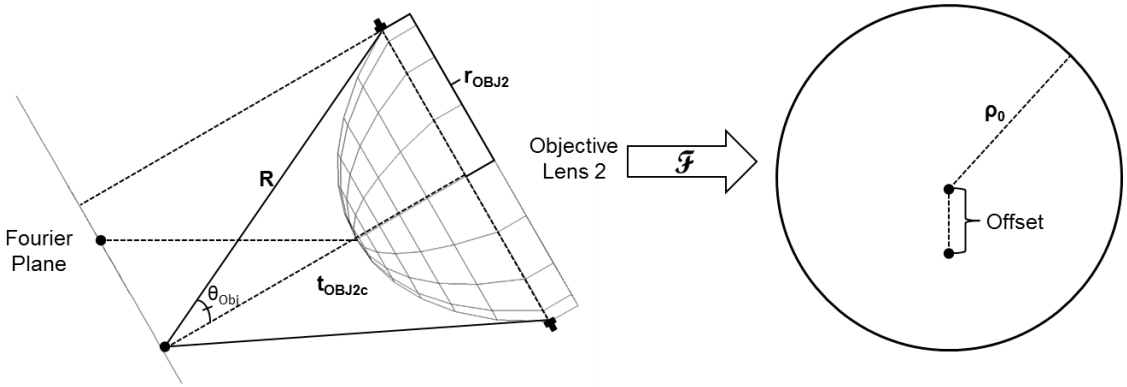

Figure 31: Aperture of a tilted lens system applied to a tilted mask and Fourier plane. Because all planes are still coplanar, the result is a shift in the applied aperture.

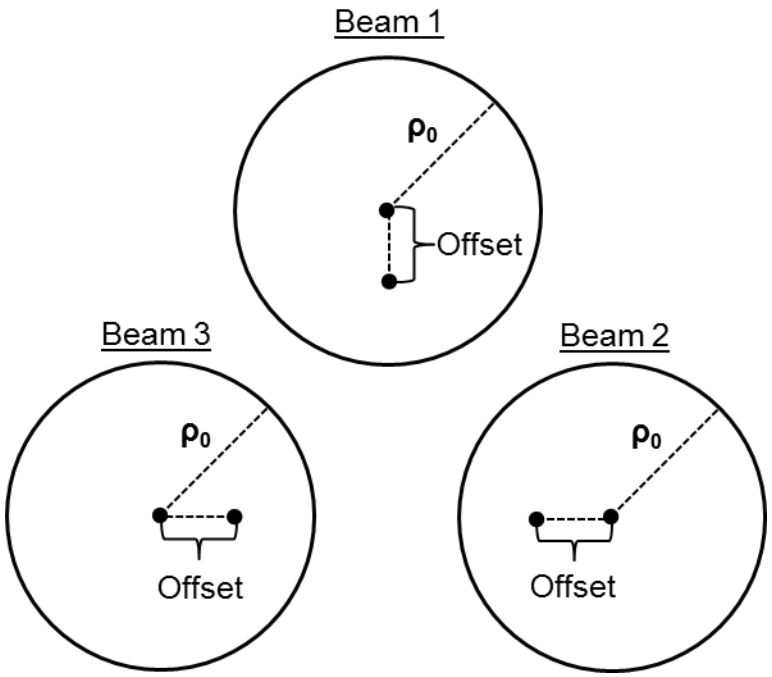

Figure 32: Aperture shifts corresponding to axes (a) 1, (b) 2, and (c) 3 for an MOA PIIL system in a *p4m* configuration

5.3 Combined Analysis

To provide a characterization of the mask pattern image in terms of its aberrations and diffraction behavior, a method that leverages the advantages of both ZEMAX and MATLAB is employed. Using a ray tracing approach with ZEMAX, the non-diffraction limited shape of a single mask element is generated and imported into MATLAB. Once this mask element shape is obtained, it is used to build the full mask pattern desired, in this case, a 90° waveguide bend for a photonic crystal device. A block diagram description of his procedure is shown in Figure 33. Thus, the aberrated mask pattern calculated by ZEMAX is used as the starting point for Fourier analysis

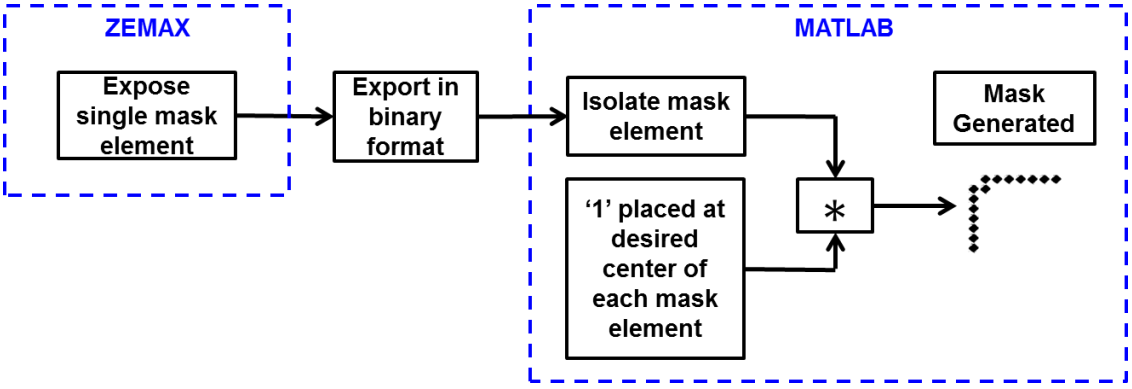

Figure 33: Block diagram of the process to construct a specific mask pattern from ZEMAX data in MATLAB. This process is repeated for each individual mask in an MOA PIIL system.

Once this mask pattern is built, a 2D fast Fourier transform (FFT) of the pattern is performed. Modeling the imaging limits of the optical system, an aperture is applied to this 2D FFT based on the numerical aperture of the second objective lens and an operating wavelength of 363.8nm. With tilted lenses, the aperture that is applied for each axis shown in Figure 32 accounting for the relative incidence of each beam with respect to the segmented lens. Once the correct aperture is applied, an inverse FFT is performed

on the truncated FFT pattern which then generates the mask pattern for each beam. Because the electric field of each beam physically interacts with the mask pattern, this mask pattern is then weighted on a pixel-by-pixel basis with each vector component of the unperturbed electric field for each beam at the image plane. These weighted electrical field components are then used to calculate the mask interference/image pattern using Eq. (2). A block diagram depiction of this process is shown in Fig. 34(b) with an example 90° waveguide bend mask element. The MATLAB code used to execute this procedure is provided in Appendix B.

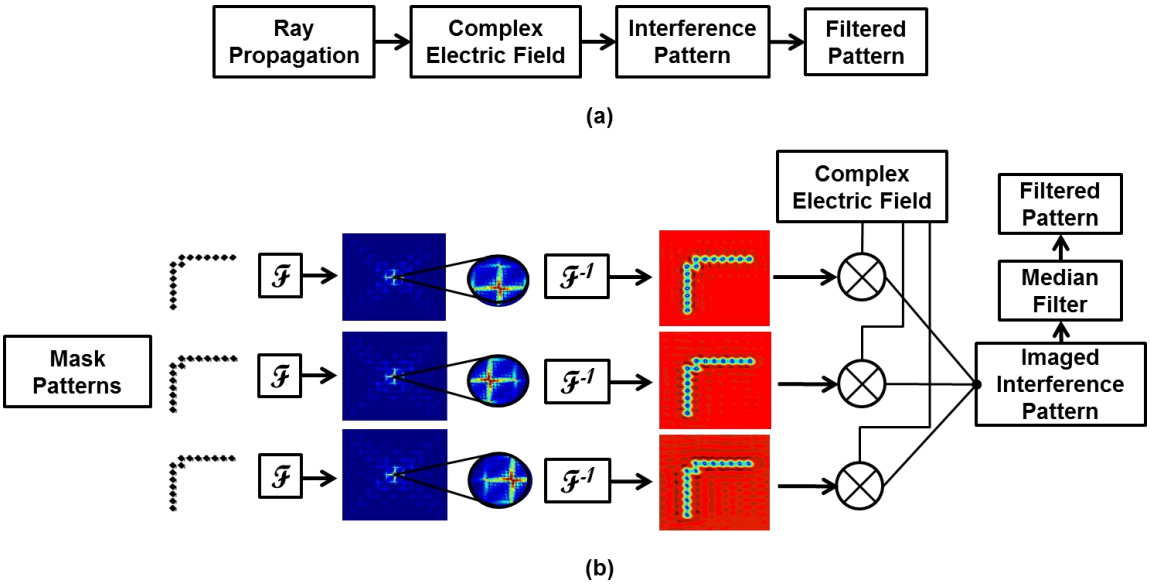

Figure 34: Block diagram of the process to construct the interference pattern in the image plane (a) without and (b) with a mask for a three-axis MOA PIIES. Note that the truncation of the Fourier transform for each beam is offset based on the relative incidence to the segmented lens.

CHAPTER 6

MOA PIIL SYSTEM SIMULATION RESULTS

Using the methods described in Chapter 5, simulations of a full three-axis MOA PIIES were performed for a joint optimum configuration with tilt angles of 30°, 35°, 40°, and 45° to determine the interference/image pattern for two different mask patterns. The first mask pattern was a 90° waveguide bend mask common to each mask as shown in Figure 34. The second mask pattern was a simple rectangular mask placed in various positions for each beam. All simulations were performed using a polarization and wavevector configuration corresponding to a *p4m* lattice structure at a wavelength of 363.8 nm [68].

6.1 Tilt Angle θ – 30 degrees

The interference/image patterns (without and with a mask present) at the center of the three overlapping beams are shown in Figures 35 (a) and (b) for a tilt angle of 30°. The mask used corresponds to a 90° waveguide bend composed of rotated-square mask elements that are 1 μm x 1 μm in the mask plane. The size of mask is reduced in the image plane due to the system magnification of 0.3. A rotated square was chosen for the mask elements for all 90° waveguide bend masks based on the work described in [8, 9] which shows that this is the optimum configuration for the least perturbation to the interference pattern. Comparing the interference patterns with and without the mask present, one can see that the surrounding interference pattern is only slightly perturbed with a single row of motifs eliminated by the mask pattern. Showing an alternate mask configuration, Figure 35(c) shows a 1D interference pattern incorporated into the larger

2D interference pattern by using a series of offset mask patterns for each beam. Each rectangular mask was generated from four 2μm x 4μm rectangular mask elements aligned to form a continuous 4μm x 8μm rectangle in the mask plane. Note that only two 1D patterns are present as the polarization configuration for a *p4m* lattice dictates that beams 2 and 3 have orthogonal polarizations and do not interfere [68].

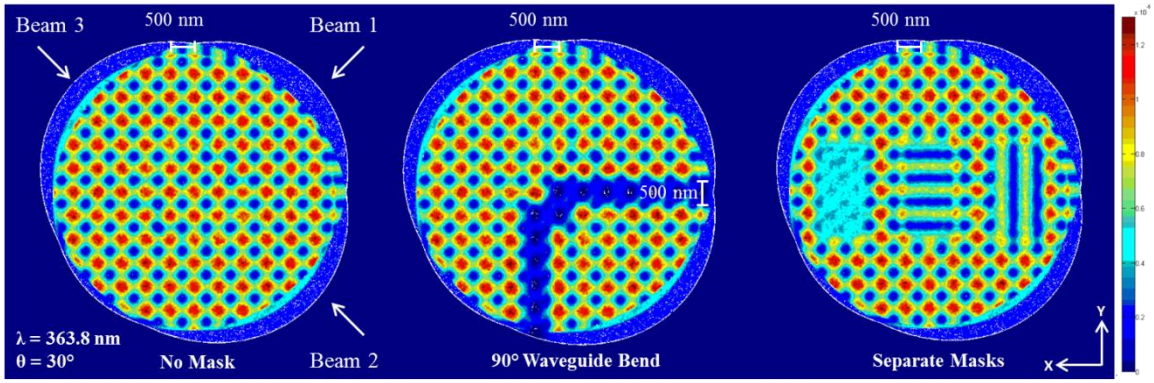

(a) (b) (c)

Figure 35: Simulated interference patterns in the center of the image plane with (a) no mask, (b) a 90° waveguide bend mask, and (c) separate rectangular masks for each beam for an MOA PIIES configuration corresponding to a tilt angle of θ = 30°.

While this analysis is done at the center of the three beams where the aberrations from the MOA PIIES are at their minimum, a second analysis is done 0.631 mm displaced along the Y-axis of the image plane corresponding to approximately half way between the chief ray and marginal rays of the three beams. In this case, the contrast between motifs is slightly reduced due to the aberrations in the system; however, the quality of the formed 90° waveguide bend still maintains a similar shape. These results indicate that even an MOA PIIES which has not been designed to minimize aberrations and ensure collimation can nevertheless produce high fidelity, interference-period-scale mask patterns integrated into a periodic lattice for a 30° lens tilt. These results have been accepted for publication in Applied Optics [69].

6.2 Tilt Angle θ – 35 degrees

The interference/image patterns (without and with a mask present) at the center of the three overlapping beams are shown in Figures 36(a) and (b) for a tilt angle of 35°. The mask used corresponds to a 90° waveguide bend composed of rotated-square mask elements that are 1 μm x 1 μm, the same size as the mask elements used for θ = 30°. With the increase in incidence angle for the beams, the spacing between periodic elements has decreased to 450 nm. Accordingly, the spacing between the individual elements composing the 90° waveguide bend was slightly decreased to ensure the imaged mask pattern matched the lattice periodicity as closely as possible. While the quality of the unperturbed interference pattern is similar to the case of θ = 30°, because of the aberrations present in the MOA PIIES, the increased angle of incidence has caused each individual beam to experience increased astigmatism. This increased astigmatism occurs along a direction that is parallel to the projection of its wavevector onto the image plane based on the orientation of optical elements in each beam axis. This causes the area where all three beams overlap to decrease. Moreover, this causes the intensity of the resulting interference pattern to increase; the relative color scale in this case has been adjusted to show the detail of the interference pattern.

Comparing the interference patterns with and without the mask present, one can see that the surrounding interference pattern is only slightly perturbed with a single row of motifs eliminated by the mask pattern. However, the imaged 90° waveguide bend mask is not as sharp as compared to the one formed in the simulation of the θ = 30° case. Showing an alternate mask configuration, Figure 36(c) shows a 1D interference pattern

incorporated into the larger 2D interference pattern by using a series of offset mask patterns for each beam. Each rectangular mask was generated from four 2μm x 4μm rectangular mask elements aligned to form a continuous 4μm x 8μm rectangle in the mask plane. Once again, only two 1D patterns are present as the polarization configuration for a *p4m* lattice dictates that beams 2 and 3 have orthogonal polarizations and do not interfere. Note that while the each 1D pattern is clearly formed, the increased aberration from the corresponding increase in incidence angle results in imaged mask patterns that begin to resemble parallelograms instead of the original rectangular mask element.

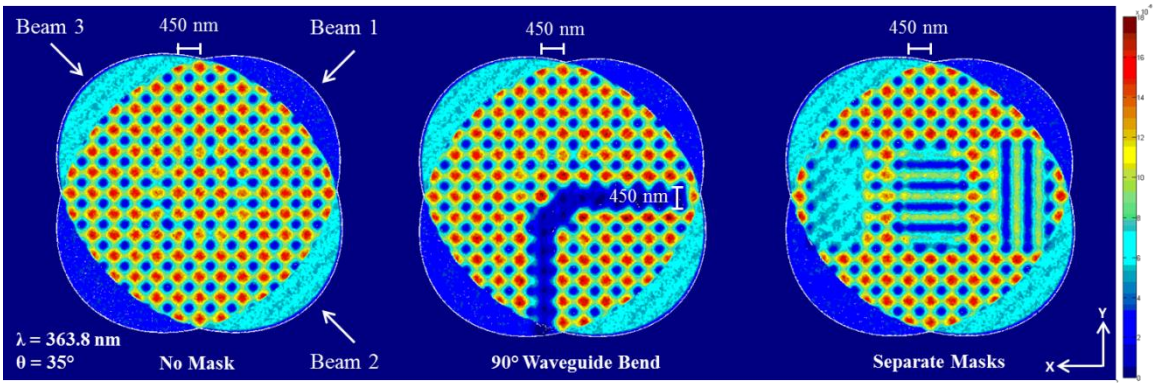

(a) (b) (c)

Figure 36: Simulated interference patterns in the center of the image plane with (a) no mask, (b) a 90° waveguide bend mask, and (c) separate rectangular masks for each beam for an MOA PIIES configuration corresponding to a tilt angle of θ = 35°.

6.3 Tilt Angle θ – 40 degrees

The interference/image patterns (without and with a mask present) at the center of the three overlapping beams are shown in Figures 37(a) and (b) for a tilt angle of 40°. With the increase in incidence angle for the beams, the spacing between periodic elements has decreased to 400 nm. The mask used corresponds to a 90° waveguide bend composed of rotated-square mask elements that are 950 nm x 950 nm, slightly smaller than the mask

elements used for $\theta = 30°$. Based on these changes, the spacing between the individual elements composing the 90° waveguide bend was slightly decreased to ensure the imaged mask pattern matched the lattice periodicity as closely as possible. While the quality of the unperturbed interference pattern is similar to the cases of $\theta = 30°$ and $\theta = 35°$, because of the aberrations present in the MOA PIIES, the increased angle of incidence has caused each individual beam to experience increased astigmatism. This increased astigmatism occurs along a direction that is parallel to the projection of its wavevector onto the image plane based on the orientation of optical elements in each beam axis. This causes the area where all three beams overlap to once again decrease. Similar to the previous case, this causes the intensity of the resulting interference pattern to increase; the relative color scale in this case has been adjusted to show the detail of the interference pattern.

Comparing the interference patterns with and without the mask present, one can see that the surrounding interference pattern is only slightly perturbed with a single row of motifs eliminated by the mask pattern. The imaged 90° waveguide bend mask is similar in quality to the one formed in the simulation of the $\theta = 35°$ case. Showing an alternate mask configuration, Figure 37(c) shows a 1D interference pattern incorporated into the larger 2D interference pattern by using a series of offset mask patterns for each beam. Each rectangular mask was generated from four 1μm x 2μm rectangular mask elements aligned to form a continuous 2μm x 4μm rectangle in the mask plane. Once again, only two 1D patterns are present as the polarization configuration for a *p4m* lattice dictates that beams 2 and 3 have orthogonal polarizations and do not interfere. Note that while the each 1D pattern is clearly formed, the increased aberration from the corresponding increase in incidence angle results in imaged mask patterns that begin to resemble

parallelograms instead of the original rectangular mask element. This behavior is more dominant that in the θ = 35° case due to the increased aberration present in this configuration.

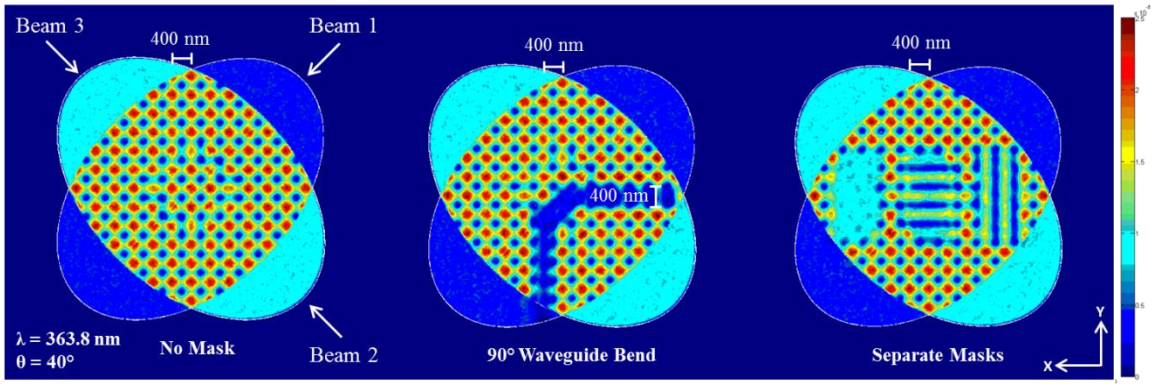

(a) (b) (c)

Figure 37: Simulated interference patterns in the center of the image plane with (a) no mask, (b) a 90° waveguide bend mask, and (c) separate rectangular masks for each beam for an MOA PIIES configuration corresponding to a tilt angle of θ = 40°.

6.4 Tilt Angle θ – 45 degrees

The interference/image patterns (without and with a mask present) at the center of the three overlapping beams are shown in Figures 38(a) and (b) for a tilt angle of 45°. With the increase in incidence angle for the beams, the spacing between periodic elements has decreased to 350 nm. The mask used corresponds to a 90° waveguide bend composed of rotated-square mask elements that are 950 nm x 950 nm, the same size as the mask elements used for θ = 40°. Based on these changes, the spacing between the individual elements composing the 90° waveguide bend was slightly decreased to ensure the imaged mask pattern matched the lattice periodicity as closely as possible. While the quality of the unperturbed interference pattern is similar to the case of θ = 40°, because of the aberrations present in the MOA PIIES, the increased angle of incidence has caused each individual beam to experience increased astigmatism. This increased astigmatism occurs

along a direction that is parallel to the projection of its wavevector onto the image plane based on the orientation of optical elements in each beam axis. This causes the area where all three beams overlap to once again decrease. Similar to the previous case, this causes the intensity of the resulting interference pattern to increase; the relative color scale in this case has been adjusted to show the detail of the interference pattern.

Comparing the interference patterns with and without the mask present, one can see that while the surrounding interference pattern is only slightly perturbed, the single row of motifs is not entirely eliminated by the mask pattern. This is likely due to the large aberration each mask element is experiencing from the system. Figure 38(c) shows an alternate mask configuration using a series of offset mask patterns for each beam to generate 1D interference patterns incorporated into the larger 2D interference pattern. Each rectangular mask was generated from four 1μm x 2μm rectangular mask elements aligned to form a continuous 2μm x 4μm rectangle in the mask plane. In this case, the quality of 1D pattern formed has decreased significantly due to the increased aberration from the corresponding increase in incidence angle. This results in imaged mask patterns that begin to resemble parallelograms instead of the original rectangular mask element. This behavior is more dominant that in the $\theta = 40°$ case due to the increased aberration present in this configuration.

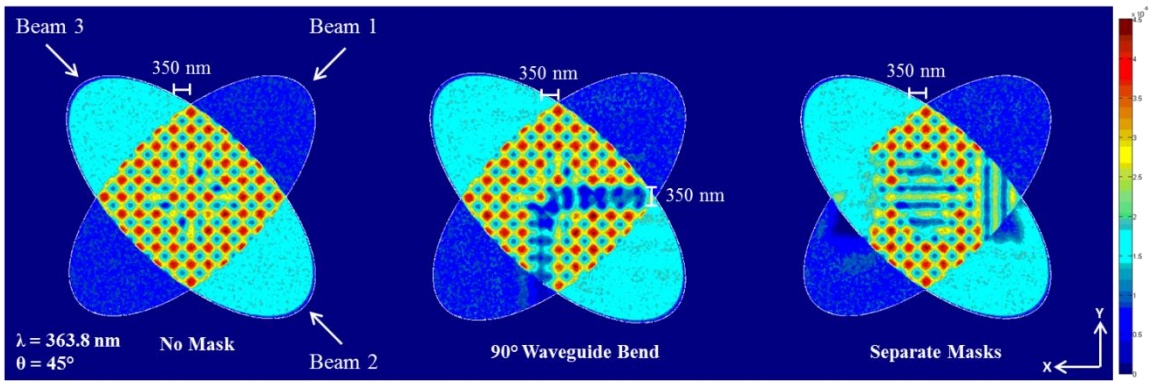

(a) (b) (c)

Figure 38: Simulated interference patterns in the center of the image plane with (a) no mask, (b) a 90° waveguide bend mask, and (c) separate rectangular masks for each beam for an MOA PIIES configuration corresponding to a tilt angle of θ = 45°.

6.5 Comparison and Analysis

As expected, the increase in incidence/tilt angle for each MOA PIIES configuration produced a corresponding decrease in the periodicity of the interference pattern. The quality of the unperturbed interference pattern decreased slightly for the incidence/tilt angles of 40° and 45°, but remained of usable fidelity. Of greater interest, the aberrations present in this MOA PIIES configuration prevent each beam from being imaged as a circle in the image plane. This effect becomes more pronounced as the incidence/tilt angle increases as shown in Figure 39(a) resulting in beams of increased eccentricity. This results in a smaller, but more intense area of exposure as the angle of incidence/tilt increases. To form circular beams at the image plane, custom optical elements could be designed to reduce the aberrations in the system.

With regard to the imaging/interference pattern formed with a set of common 90° waveguide bend masks, the fidelity of the non-periodic functional element is imaged with usable fidelity up to incidence/tilt angles of 40° despite the aberrations present in the system. Because of the aberrations present in this MOA PIIES configuration, a series of

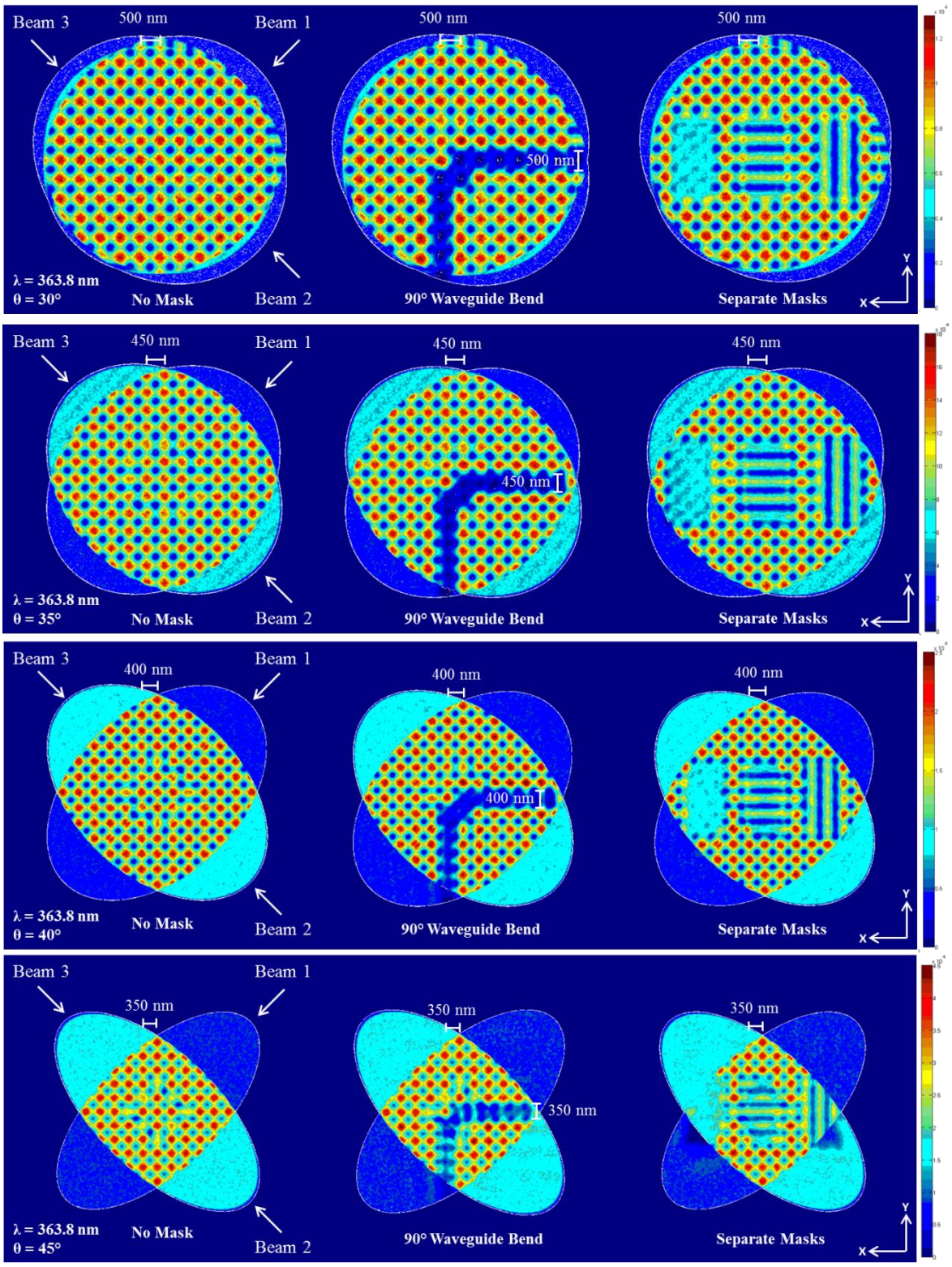

(a) (b) (c)

Figure 39: Comparison of image/interference patterns for θ = 30-45°.

mask elements aligned in the mask plane will yield elements that are no longer aligned with the periodic pattern from multi-beam interference in the image plane as shown in Figures 40(a) and (b). To compensate for this, misaligning the elements in the mask plane will yield elements that are properly aligned but still aberrated as shown in Figures 40 (c) and (d). This will yield the best possible performance as the imaged elements are still aberrated, but aligned with the period pattern in the image plane. Because each mask image is aberrated in a different direction based on orientation of optical elements in each individual beam axis, it seems that these aberrations are effectively weakened over the imaged area. Additionally, each mask image contains different spatial frequency content which enhances the quality of the final image. This averaging allows for a high fidelity formation of the 90° waveguide bend.

In the case of offset masks, the imaged rectangles, shown in Figure 39(c), are of lower fidelity than the 90° waveguide bends in Figure 39(b). Rectangular masks were chosen as a single continuous element because early simulations attempting to use spaced rotated squares to produce a rectangular shape were of substantially degraded quality. Even using continuous mask elements, the quality of the mask and surrounding interference pattern is degraded because each mask images a separate area with its own unique aberration and frequency content. Thus, when incorporating 1D interference patterns within a 2D interference pattern, the aberrations in the optical system will play a larger role in the fidelity of the 1D interference patterns formed. Additionally, the mask used to incorporate a 1D interference pattern must be a continuous single continuous element to maintain the fidelity of the pattern.

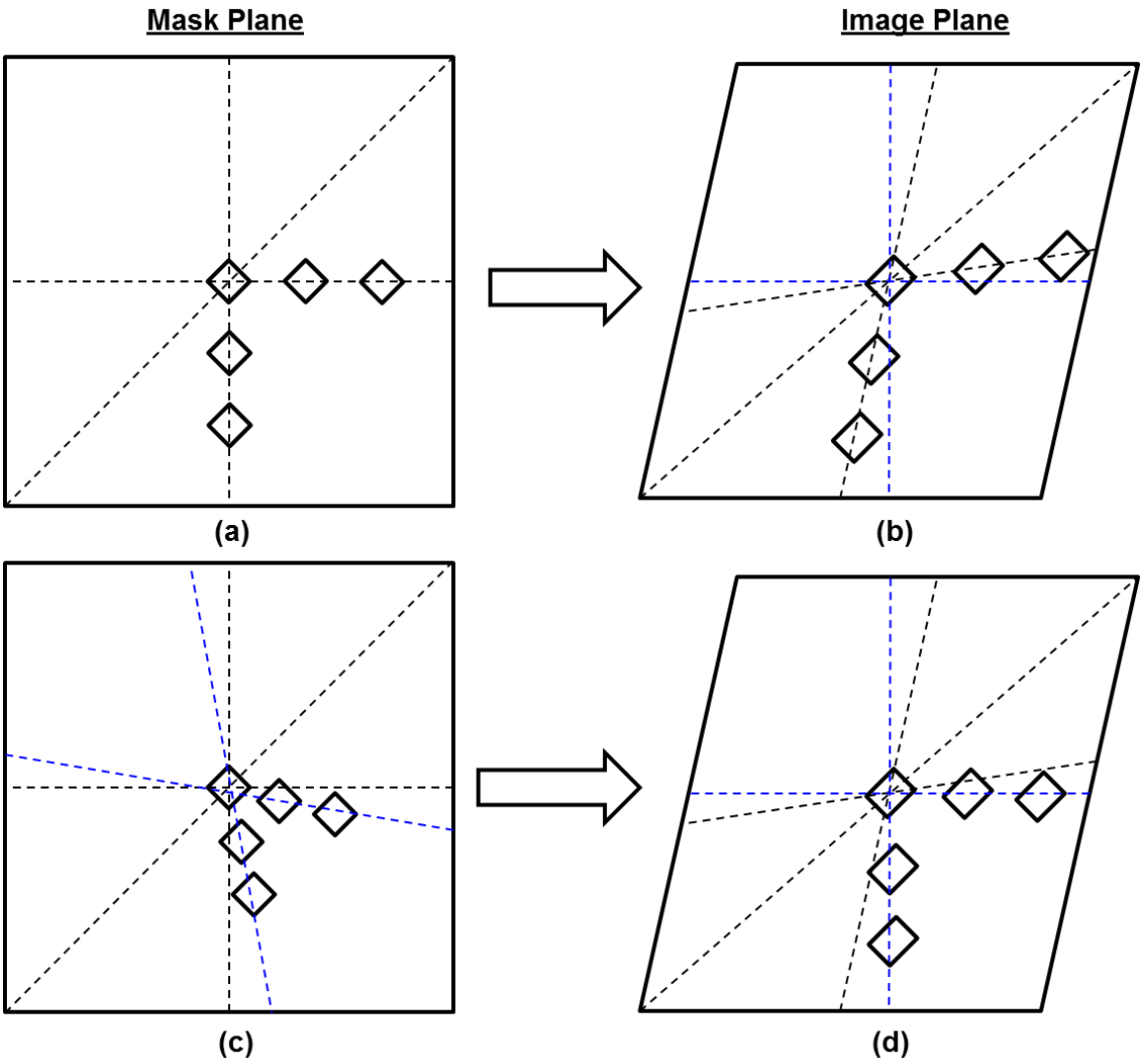

Figure 40: Alignment of mask elements. Because of the aberrations present in this MOA PIIES configuration, (a) a series of mask elements aligned in the mask plane will yield (b) elements that are no longer aligned with the periodic pattern from multi-beam interference in the image plane. To compensate for this, (c) misaligning the elements in the mask plane will yield (d) elements that are properly aligned but still aberrated. This alignment with the periodic pattern in the image plane will yield the best possible performance.

In all cases, the interference motifs surrounding functional elements are largely unperturbed. This occurs because the diffraction patterns associated with the rotated-square mask elements are oriented within the mask to have a minimal effect on the periodic pattern. When rectangular mask elements are used, there is a slight increase in

the perturbation of periodic elements around the imaged mask elements. This occurs because the diffraction pattern of a rectangle is not optimal for a *p4m* lattice configuration. Even with the non-optimal alignment, the surrounding interference pattern is of useable fidelity. At an incidence/tilt angle of 45°, there is significant degradation in the fidelity of the 90° waveguide bend as well as the as rectangular 1D interference patterns shown in Figures 38 and 39. This likely occurs because the aberrations in system are now strong enough such that very little averaging of effects occurs. Thus, for angles of incidence/tilt beyond 40° aberrations in the system become unmanageable requiring a redesign of the optical components.

Thus, even for the non-optimized components used in the MOA PIIES, for a tilt angle of 40° it has been shown that a pattern-integrated interference pattern can be produced with reasonably high fidelity. In place of the fixed non-optimal commercial components used here, custom optical elements could be designed to improve the quality of the desired combination of interference and imaging. Increased angles of incidence/tilt in the system configuration would also be possible allowing for smaller-sized periodic elements.

CHAPTER 7

CONCLUSIONS

The purpose of this thesis has been to establish a methodology for modeling that characterizes, simulates, and optimizes MOA PIIL systems. Ray tracing analysis was used to specify a series of system parameters, intensity pattern metrics, and optical system metrics to characterize the collimation and imaging performance of an MOA PIIES. An optimization process was developed also using ray tracing to minimize jointly the divergence and aberrations for an MOA PIIES for a given fixed set of optical components. This jointly optimized MOA system configuration was used to develop a simulation model combining the advantages of ray tracing and Fourier optics to model successfully the image/interference pattern produced by an MOA PIIES.

7.1 Summary of Results

7.1.1 PIIL Application Areas

The specific application areas of mirco- and nano-electronics, photonic crystals, and biomedical structures were examined to provide context for the research objectives examined in this thesis. PIIL has the potential to meet the demand for the high-volume production of smaller mirco- and nano-electronic integrated devices by forming integrated functional elements in a single, rapid step. Additionally, photonic crystal and biomedical structures are nascent areas that are poised for large growth in which PIIL may potentially be an enabling technology for large-scale commercial production.

7.1.2 PIIL System Configurations and Impact

Various PIIL system configurations and their impact were also examined in detail. PII was framed as a logical progression from conventional interference and holography where the combination of waves that have joint reference and subject roles are used to form pattern-integrated interference patterns. Configurations and naming conventions for various implementations of PIIL with their associated advantages and disadvantages were described in detail. SOA PIIL system configurations utilize a set of optical elements aligned along a single optical axis designed to accommodate multiple beams to form a PII pattern on a photosensitive material. MOA PIIL system configurations utilize multiple sets of optical elements with each set aligned along an individual axis. Each set is designed to accommodate a single beam with the set of optical axes arranged to form a PII pattern on a photosensitive material. To have all masks from the multiple axes in focus on the photosensitive material, the optical elements in the imaging subsystem of each axis must be parallel to the surface of the photosensitive material. This means that the elements of each imaging subsystem would be tilted with respect to their individual optical axis. Each of these system configurations can incorporate an imaging subsystem composed of either a single objective lens or a double objective lens system arranged in a Fourier-transform configuration. Each of these imaging subsystem types may in general incorporate multiple optical elements that can be effectively modeled as either one of these two types. SOA system configurations have fewer elements and are simpler to configure while MOA system configurations offer more degrees of freedom to exploit. A basic objective lens imaging subsystem configuration is simple to implement while a Fourier–transform double-objective lens system offers the ability for spatial frequency

filtering to enhance imaging quality, larger demagnification to produce smaller elements, and have larger image-side NA allowing for higher resolution imaging. The impact of these various PIIL configurations is to allow rapid prototyping with the use of commercially available components while also allowing for the potential of high-volume production with the incorporation of a diffractive photomask (DPM). A DPM allows for an interferometrically stable implementation that can be used repeatedly without having to consider the careful alignment of the original PIIL system.

7.1.3 MOA PIIL System Characterization and Optimization

With the context for PIIL systems properly established, ray optics was used to formulate a characterization model to describe the aberrations that occur in an MOA PIIL system. An MOA Fourier–transform PIIL configuration implemented with single-element, non-optimal lenses that were previously used in the prototype SOA PIIES was the specific case chosen to develop this model. The characterization and optimization were performed on a single axis of a MOA configuration under the assumption that all axes of the system were degenerate; however, the characterization and optimization model could easily be performed on different axes. A set of interference/image pattern metrics, collimation and ray spot diagrams, were used to describe respectively the quality of the periodic pattern and mask image formed. The optical system parameters to be optimized for this model were the distance between the mask plane and the first objective lens, the distance between the two objective lenses, and the distance between the second objective lens and the image plane; denoted as d_1, d_2, and d_3 respectively in Figure 19. Using ZEMAX optical design software, these optical system parameters were optimized

in a manner such that the resulting imaging subsystem configuration would approximate a 4f optical imaging system as closely as possible. A description of this procedure is given in Figure 22. This optimization was performed by considering collimation and ray spot diagrams both individually and jointly and for input wavelengths of 363.8 nm (Ar-ion laser) and 780 nm (optics design wavelength). Simulations for tilt angles from 0° to 45° in 5° intervals showed that as the tilt angle of optical elements was increased, the aberrations present in the optical system also increased. The optimization of collimation and image quality individually produce generally similar requirements on the optical system. The large amounts of divergence and displacement in the spot pattern that occur with higher angles of tilt indicate that a more purpose-specific optical system would be needed to correct these effects further for larger tilt angles. The results for system optimization for input wavelengths of 363.8 nm (Ar-ion laser) and 780 nm (wavelength for which the optics were designed) showed very little change in system behavior.

7.1.4 MOA PIIL System Simulation Method

While the characterization analysis of an MOA PIIES provided a very quantitative assessment of system performance, it did not provide example images for evaluation. To this end, a method for simulating a full MOA Fourier–transform PIIES using a combination of ray tracing and Fourier optics was developed using a three-axis MOA Fourier–transform PIIL configuration without mirrors. Ray tracing does not provide an intuitive method for interference calculation but can be used to model interference provided a large number of rays with phase and polarization information are used. This provides the advantage of accurately modeling the system's aberrations and was used to

calculate the interference pattern and aberrated mask image by calculating values in ZEMAX and exporting and processing the data in MATLAB. Because mask elements are on the same order as the wavelength used, the diffraction effect of the mask pattern was incorporated by applying a FFT to the aberrated mask image and truncating it based on the NA of the optical system and the wavelength of light used. Combining these methods in MATLAB yielded a very accurate approximate of the image/interference pattern produced by a MOA PIIES.

7.1.5 MOA PIIL System Simulation Results

Simulations of a full three-axis MOA PIIES were performed for a joint optimum configuration with tilt angles of 30°, 35°, 40°, and 45° to determine the interference/image pattern for two different mask patterns. The first mask pattern was a 90° waveguide bend mask common to each mask. The second mask pattern was a simple rectangular mask placed in various positions for each beam. All simulations were performed using a polarization and wavevector configuration corresponding to a *p4m* lattice structure at a wavelength of 363.8 nm. It was demonstrated that an increased angle of incidence/tilt system configuration results in a smaller, but more intense area of exposure due to the aberrations in the system configuration. In general, masks that are formed by overlapping the images of several beams are of higher quality than the image produced by a single beam. Moreover, the quality of the mask image formed within the pattern remained of usable fidelity up to a tilt angle of 40°. Thus, even for the non-optimized components used in the MOA PIIES, it has been shown that a pattern-integrated interference pattern can be produced with reasonably high fidelity. At a tilt

angle of 45°, significant degradation in the image/interference pattern due to the aberrations in the system necessitating a redesign of system components. In place of the fixed non-optimal commercial components used here, custom optical elements could be designed to improve the quality of the desired combination of interference and imaging. Increased angles of incidence/tilt in the system configuration would also be possible allowing for smaller-sized periodic elements.

7.2 Future Work

The work presented in this thesis is intended to provide a framework for characterizing, simulating, and optimizing MOA configuration PIIL systems. As previously stated, all work was performed with single element, non-optimal lenses. To optimize fully the system performance, a redesign of the optical components to remove system aberrations is required. Future research following this work should investigate the design of purpose-specific lenses and the development of a prototype MOA configured PIIES to verify experimentally the results of simulations.

7.2.1 Design of Purpose-Specific Lenses

The single element, non-optimal lenses used to develop the characterization, optimization, and simulation models presented in this thesis were originally designed for an SOA PIIES which had to accommodate three beams [1, 4, 5]. Lenses to be used for a MOA configuration need to accommodate only one beam and could be greatly reduced in size as shown in Figures 41(b) and 42(c). Moreover, the optical elements can be specifically designed for a particular application.

Starting with the first elements in a single axis of a MOA configuration, the expander lens and condenser lens set that produces a collimated beam incident upon the axis mask can be more suitably chosen. As the expander and condenser lenses are never tilted for any MOA configuration, only the size and focal lengths of these elements needs to be changed to optimize performance. The ratio of the focal length of the condenser lens to the focal length of the expander lens determines the radius of the beam that is incident on the mask plane. This ratio should be suitably chosen based on the desired size of the exposure area on the photosensitive material and the associated magnification of the imaging subsystem. The diameter of these lenses should be chosen so that they are large enough to accommodate a single beam, but no larger. The thickness of these lenses should be selected to be a reasonable values based upon the specified radius of the curved surface and diameter of the lens. An example of a suitable diameter for a condenser lens is shown in Figures 41(b) and 42(c). Choosing a commercially available expander lens and designing a condenser lens that meets these specifications would allow for the simplest implementation. Additionally, to expose a circular beam cross-section at the image plane, elliptical input beams are needed due to the relative tilt of the mask and image planes to the incident beam. For the simulations described in Chapter 6, the input beams were specified to be elliptical, but it is possible to design the expander and condenser lens to produce an elliptical beam if desired rather than having a separate system to do so.

The design of purpose-specific objective lenses would involve optical system parameters to be specified as well as ones to be optimized. Optical system parameters for the two objective lenses which should be specified are the ratio of their focal lengths and

the physical size (diameter and thickness) of the lenses. Optical system parameters which should be optimized are the tilt of the aspheric surface of both lenses, the aspheric coefficients of those surfaces, and the spacing of the objective lenses and the photosensitive material.

Similar to the relationship between the expander and condenser lenses, the ratio of the focal lengths of the second objective lens to the first objective lens will affect the size of the exposure area on the photosensitive material. However, this focal length ratio also determines the magnification of the imaging subsystem of the PIIES. It is desirable to have a magnification of less than one because this will decrease the size of the functional elements that can be imaged. The previous SOA PIIES utilized an objective lens set with a magnification of 0.3. Therefore, the focal length of each objective lens, determined by the radius of curvature specified for the aspheric surface should be chosen based on these considerations and the desired system performance. Moreover, the diameter of these of objective lenses can be greatly reduced as they only need to accommodate a single beam. An example of a more suitable diameter choice for the objective lenses is shown in in Figures 41(b) and 42(c) for the same lens thickness as the original lenses implemented in the prototype SOA configuration [1, 4, 5]. Additionally, the thickness of the objective lenses should be suitable scaled with the change in diameter to accommodate a single beam.

While these lens specifications would adjust the exposure area, magnification, physical size of the objective lenses for a particular application, they do not address correcting the large aberrations introduced from tilting the lenses. To reduce and remove these aberrations, each objective lens must be designed as an asymmetric lens to

counteract the effects of tilting the lenses. The simplest way to introduce asymmetry into each lens is to specify a relative tilt of the curved lens surface with respect to its planar surface as shown in Figure 41 for the two objective lenses. Using the same merit functions and optimization procedures as described in Appendix A and Chapter 4 respectively, the tilt of the curved surface of each objective lens can be specified as a variable to be optimized so long as the displacement of the lens along the y-direction was suitably adjusted to ensure the chief ray remains parallel to the system axis as shown in Figure 41. It may also be workable to optimize each objective lens separately to ensure a symmetric input to each objective lens yields a symmetric output.

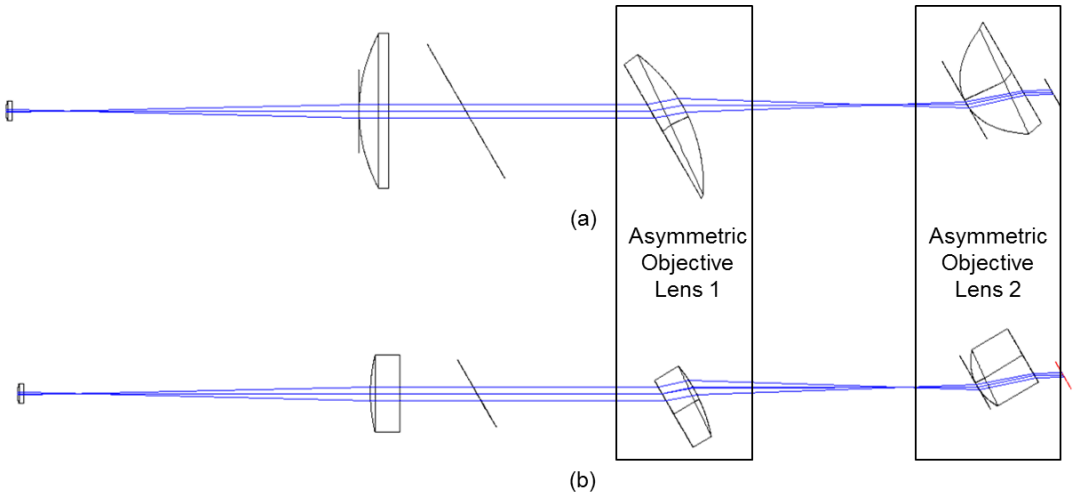

Figure 41: Single axis of a MOA PIIL system configuration implemented using asymmetric objective lenses with diameters (a) the same as the previously used non-optimal elements and (b) reduced in size more appropriate to accommodate a single beam. In principle, the thickness of these lenses could also be reduced.

With these more suitable lenses designed, the relative placement of these objective lenses and the photosensitive plane would also need to be suitably adjusted. Fortunately, these parameters would be optimized using the exact same procedure as described in Chapter 4. As an additional enhancement, the aspheric coefficients for each objective

lens surface can be adjusted to minimize the spherical aberration of the image/interference pattern recorded in the photosensitive material. These coefficients could be optimized after an appropriate asymmetric lens has already been designed.

Thus, in designing purpose-specific lenses for a practical implementation of an MOA PIIES, the same software applications and similar techniques can be used. Instead of simply varying the relative placement of the system's optical elements, the parameters of each optical element can be varied to optimize system performance. Once the new optical elements have been designed, they can be characterized and simulated using the techniques presented in this thesis.

7.2.2 Design of MOA PIIL Experimental Configuration

The development of a prototype MOA PIIL configuration to verify experimentally the results of simulations is necessary to continue the development of these systems. While the full three-axis MOA PIIES shown in Figure 29 that was simulated in Chapter 6 could be physically constructed, the lenses used can be excessively large and the configuration of the three axes would be difficult to construct with limited resources. To construct a MOA PIIES in a more compact manner, the introduction of a mirror between the second objective lens and the photosensitive material could be inserted as shown in Figure 42. This would allow for all three axes to be parallel and closely spaced before converging on the image plane as shown in Figure 43. However, because of this compact design, the single-element, non-optimal lenses used to construct a MOA PIIES in Chapters 5 and 6 would be too large and would obstruct the beams from different axes. To remedy this, these lenses could be truncated as shown in Figure 42(b) such that only

the portion of each lens that interacts with each axis beam remains. The result of this truncation is shown in Figure 42(b) where the new lens elements have the exact same performance as the full size lenses shown in Figure 42(a).

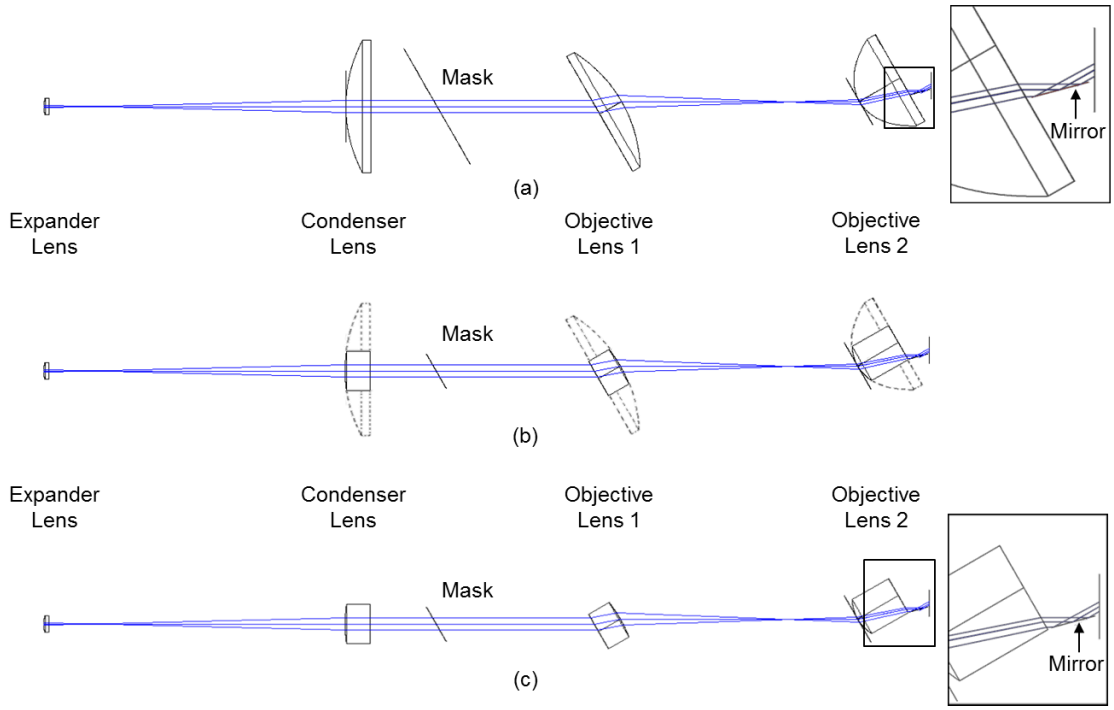

Figure 42: Single axis of a MOA PIIL system configuration with mirror. This can be implemented using (a) the non-optimal optical components used in an SOA PIIES. Because their excessive size will obstruct beams from other axes, (b) it is necessary to truncate these lenses. (c) The system implemented using these truncated elements yields the same system performance as the full-sized elements

In constructing a full three-axis MOA PIIES shown in Figure 43, it should be noted that the required spacing of the axes require that the condenser lenses and the objective lens sets need to be constructed as segemented lenses. This construction may incorporate the advantage of interferometric stability normally associated with a SOA configuration as each segmented lens may be considered as a single element when aligning the system. The tight spacing of the mask elements as well as the three mirrors needed to redirect each beam to the image plane suggests the construction of a custom element designed to

hold all three elements. Due to size requirements, the thickness of the second objective lens had to be reduced requiring a slight adjustment to the placement of the image plane. The aspheric surface of the second objective lens was unaltered. The truncated, non-optimal elements shown in Figure 43 can be replaced with custom-designed, purpose-specific lenses which will affect the spacing the the axes and the optical elements with the axes, but the general experimental configuration will remain the same.

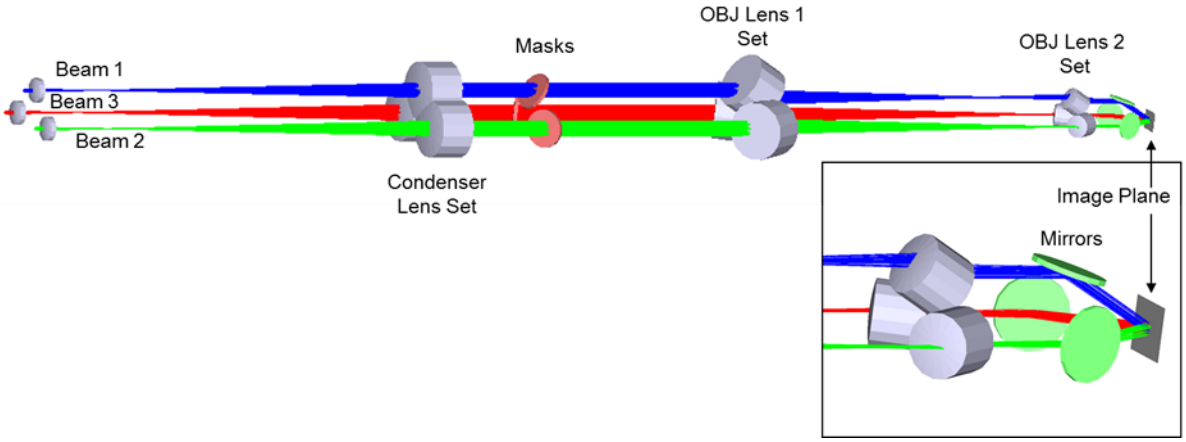

Figure 43: Full three-axis MOA PIIES implemented using the truncated, non-optimal elements used in a previous SOA PIIES.

7.3 Concluding Remarks

The research described in thesis has defined a methodology of modeling for an MOA system configuration for PIIL. This work is intended as a first step towards the development of a custom-built prototype MOA PIIES. While the simulations presented show functional elements designed for applications for photonic crystals, there is great potential for future applications biomedical structures, microelectronics, and any area where rapid, low cost fabrication of periodic structures with integrated, interference-period scale functional elements is desired.

APPENDIX A

ZEMAX SYSTEM CHARACTERIZATION AND OPTIMIZATION

The MOA PIIL system characterization and optimization described in Chapter 4 was developed and modeled using ZEMAX optical design software [66]. ZEMAX has two primary program modes, sequential and non-sequential mode [66]. In sequential mode operation, the optical components of a system are constructed in the order, or sequence, in which they are entered into the program. Thus, the position and orientation of each optical element is only specified in reference to the previously entered element. This mode allows for the full range of ZEMAX tools to be leveraged and is suggested for use in designing imaging systems [66]. However, sequential mode analysis cannot generate multiple beams which are necessary when modeling multi-beam interference. Non-sequential mode operation, optical elements are specified in a fixed XYZ coordinate space and individually placed based on the user's specifications [66]. This mode also allows for the placement of multiple ray sources; however, fewer ZEMAX tools are available for analysis. Using both sequential and non-sequential mode analysis, merit functions were applied to optimize the quantities d_1, d_2, and d_3 and characterize system performance as specified in Chapter 4. Additionally, ray data for the simulations described in Chapters 5 and 6 were generated non-sequential analysis mode.

For all ZEMAX simulations, the same set of objective lens components was used. The first objective lens was a Thorlabs AL100200-A aspheric lens with a 100 mm diameter and an effective focal length of 200 mm. The second objective lens was a

Thorlabs AL7560-A aspheric lens with a 75 mm diameter and an effective focal length of 60mm. Based on the data available in the Thorlabs specification sheets, these lenses were constructed as even aspheres in ZEMAX using the data listed in Table 2. An even aspheric surface is a surface that is described by a polynomial expansion of the deviation from a spherical (or aspheric described by a conic) surface [66]. ZEMAX uses an aspheric model to describe the shape of the lens. Specifically, the "sag" or z-coordinate of the aspheric lens surface, *z*, is specified by the equation

$$z = \frac{c\,r^2}{1+\sqrt{1-(1+k)c^2r^2}} + \alpha_2 r^2 + \alpha_4 r^4 + \alpha_6 r^6 + \alpha_8 r^8 + \alpha_{10} r^{10} + \alpha_{12} r^{12} + \alpha_{14} r^{14} + \alpha_{16} r^{16} \quad (9)$$

where *c* is the curvature (the reciprocal of the radius of curvature) of the surface, *r* is the radial coordinate of the surface, *k* is the conic constant, and α_n is the nth order aspheric coefficient [66]. The conic, *k*, is equal to the negative square of the ellipticity, ε, of the surface (i.e. $k = -\varepsilon^2$) with the conic being less than -1 for hyperbolas, -1 for parabolas, between -1 and 0 for ellipses, 0 for spheres, and greater than 0 for oblate ellipsoids [66]. The radius of curvature, thickness, and diameter for these aspheric lenses are listed in subsequent tables detailing sequential and non-sequential analysis.

Table 2: ZEMAX aspheric lens equation data.

OBJ Lens #	Glass	Conic	4th Order Term	6th Order Term	8th Order Term	10th Order Term	12th Order Term	14th Order Term	16th Order Term
1	N-BK7	-1	-4.9646E-08	-7.4018E-13	-9.4142E-18				
2	N-BK7	-0.905	1.6366E-06	4.1293E-10	9.893E-14	-3.6809E-17	-4.6067E-21	5.5772E-24	-2.6358E-27

The 4f optical imaging subsystem of the MOA PIIES to be optimized was constructed in both non-sequential and sequential mode in ZEMAX. Table 3 depicts the key parameters entered in non-sequential mode whose configuration is shown in Figure 21(b); Table 4 depicts the key parameters entered in sequential mode whose configuration is shown in Figure 21(a). In Table 3, the origin of the XYZ coordinate

system is located at the center of the mask plane. In Table 4, there origin of the XYZ coordinate system is located at the center of the image plane. In both tables, the term "radius" refers to the radius of curvature of the lens surface while the term "semi-diameter" refers to the half the diameter of the lens aperture. The type "standard" refers to a surface that is defined by the first term of Eq.(9). The type "coordinate break" indicates a change in the reference coordinate system in sequential mode. A coordinate break can have either a decenter in X, Y, or Z, or a rotation about the X, Y, Z axis. Rotations are performed in the order X, Y, Z if there are multiple rotations. The values listed in both tables correspond to the specific configuration for a tilt angle of $\theta = 30°$. The quantities listed as "variable" in both tables indicate parameters that were optimized.

Table 3: ZEMAX non-sequential mode lens data for $\theta = 30°$.

#	Object Type	Radius (*mm*)	Thickness (*mm*)	Semi-Diameter (*mm*)	X Position (*mm*)	Y Position (*mm*)	Z Position (*mm*)	Tilt About X (*Degrees*)	Notes
1	Even Asphere	102.24	19	50	0	3.835188	***Variable (d_1)***	-30	Objective Lens 1- See Table 2
2	Even Asphere	30.67	35.5	37.5	0	3.835188	***Variable (d_2)***	-30	Objective Lens 2- See Table 2
3	Source Ray				0	0	0	0	Analysis rays originating at center of mask plane
4	Source Ray				0	0	0	-2.5	
5	Source Ray				0	0	0	2.5	
6	Source Ray				0	0	0	-5	
7	Source Ray				0	0	0	5	

Table 4: ZEMAX sequential mode lens data for $\theta = 30°$.

#	Type	Radius (*mm*)	Thickness (*mm*)	Semi-Diameter (*mm*)	Decenter Y (*mm*)	Tilt About X (*Degrees*)	Notes
0	Standard	Infinity	Infinity				
1	Coordinate Break		0			-30	
2	Standard	Infinity	103.6228614	50			
3	Coordinate Break				-66.367848		
4	Standard	Infinity		26.6886			
5	Standard	Infinity	19	50			Objective Lens 1- See Table 2
6	Even Asphere	-102.24	***Variable (d_2)***	50			
7	Coordinate Break				-89.8825082		
8	Standard	Infinity		28.865			
9	Even Asphere	30.67	35.5	37.5			Objective Lens 2- See Table 2
10	Coordinate Break						
11	Standard	Infinity	16.050713	37.5			
12	Coordinate Break				-21.4848887		
13	Standard	Infinity		37.5			

For all optimizations, the ZEMAX optimization feature seeks to find a local minimum for the a specified merit function, *MF*, of the general form

$$MF^2 = \frac{\sum W_i \left(V_i - T_i\right)^2}{\sum W_i}, \tag{10}$$

where *W* is the absolute value of the weight of the operand, *V* is its current value, *T* is the target value, and *i* indicates the operand number [1, 66]. In this method, a root-mean-square algorithm is employed by calculating the square root of the average value of the squares of the individual errors [1, 66].

To determine the spacing between the mask plane and objective lens 1, d_1, a merit function optimization in non-sequential mode analysis was performed. Table 5 depicts the operands that were specified in this merit function to achieve the condition specified in Chapter 4. The NRSA operand is a generic non-sequential ray trace operand [66]. The source number refers to the object number as specified in Table 3. The segment number refers to the ray segment number that contains data. The data number indicates which datum is to be referenced; datum #6 corresponds to the z-direction cosine of the ray segment [66]. The z-direction cosine is a unitless direction cosine where a value of 1 corresponds to a ray traveling in the z-direction. The target value of 1 corresponds to rays that are collimated when exiting the first objective lens.

Table 5: ZEMAX merit function specifications used to optimize d_1.

Source #	Operand	Segment #	Data #	Target Value	Weight
3	NSRA	3	6	1	0.5
4	NSRA	3	6	1	0.5
5	NSRA	3	6	1	0.5
6	NSRA	3	6	1	0.5
7	NSRA	3	6	1	0.5

To determine the spacing between objective lens 1 and objective lens 2, d_2, a merit function optimization in sequential mode analysis was performed. Three different merit functions were employed to optimize collimation, the ray spot diagram, and both jointly. Tables 6, 7, and 8 depict the operands that were specified in each respective merit function to achieve the results in Chapter 4. For all merit functions, the surface numbers listed correspond to the surface numbers listed in Table 4. The operand REAC is the ray z-direction cosine after refraction from the surface listed [66]. The z-direction cosine is a unitless direction cosine where a value of 1 corresponds to a ray traveling in the z-direction. H_x, H_y, P_x, and P_y indicated the normalized field and pupil coordinates of a ray where (0,1,0,0) corresponds the chief ray and (0,0,0,1) corresponds to the marginal ray in the +y-direction. The collimation merit function attempts to have all rays pointing in the same direction as the chief ray. Based on the system configuration, the z-direction cosine of the chief ray always corresponds to cos(θ).

Table 6: ZEMAX merit function specifications used to optimize d_2 for collimation.

Surface #	Operand	Hx, Hy	Px, Py	Target Value	Weight
13	REAC	0,1	0,0	cos(θ)	1
13	REAC	0,0	1,0	cos(θ)	1
13	REAC	0,0	(-)1,0	cos(θ)	1
13	REAC	0,0	0,1	cos(θ)	1
13	REAC	0,0	0,(-)1	cos(θ)	1

In the spot diagram merit function, REAX and REAY are the ray x- and y-coordinates at the surface and ray specified. The operand SUMM performs a summation between two specified operands. This merit function compares the rays along the x- and y-axes and attempts to ensure rays that were spaced the same distance from the chief ray

in the mask plane maintain their relative spacing. Note that since the mask and image plane are tilted with respect to the optical axis of the system (specified by the path of the chief ray), an elliptical beam must be used to ensure its projection onto the mask and image planes corresponds to a circle. Thus, the rays that are specified along the y-direction have their pupil coordinates scaled by a factor of cos(θ) to ensure comparisons between rays along the x- and y-axes are performed correctly.

Table 7: ZEMAX merit function specifications used to optimize d_2 for spot diagram.

Surface #	Operand	Op#1	Op#2	Target Value	Weight
13	SUMM	REAY(P_y*cos(θ))	REAY(-P_y*cos(θ))	0	1
13	SUMM	REAX(P_x)	REAY(-P_y*cos(θ))	0	1
13	SUMM	REAX(-P_x)	REAY(P_y*cos(θ))	0	1
Note: P_y=P_x = {0.1-1.0} @ 0.1 increments; thus there are 30 values that are input into the merit function					

The joint merit function a combination of the elements of the collimation and spot diagram merit functions. Because the units of the inputs into collimation merit function (direction cosine — unitless) and the spot diagram merit function (mm) are not equivalent, a weight factor of 1000 was applied to REAC operands and a weight factor of 1 to SUMM operands to account for this difference in scales.

Table 8: ZEMAX merit function specifications used to jointly optimize d_2 for collimation and spot diagram.

Surface #	Operand	Hx, Hy	Px, Py	Op#1	Op#2	Target Value	Weight
13	REAC	0,1	0,0	N/A	N/A	1	1000
13	REAC	0,0	1,0	N/A	N/A	1	1000
13	REAC	0,0	(-)1,0	N/A	N/A	1	1000
13	REAC	0,0	0,1	N/A	N/A	1	1000
13	REAC	0,0	0,(-)1	N/A	N/A	1	1000
13	SUMM	N/A	N/A	REAY(P_y*cos(θ))	REAY(-P_y*cos(θ))	0	1
13	SUMM	N/A	N/A	REAX(P_x)	REAY(-P_y*cos(θ))	0	1
13	SUMM	N/A	N/A	REAX(-P_x)	REAY(P_y*cos(θ))	0	1
Note: P_y=P_x = {0.1-1.0} @ 0.1 increments; thus there are 30 values that are input into the merit function							

The spacing between objective lens 2 and the image plane, d_3, was determined using non-sequential mode analysis. As explained in Chapter 4 and shown in Figure 22, by assuming an arbitrary but reasonable initial values for d_2 and d_3 are determined by calculating where the two rays specified in lines #4 and #5 in Table 4 intersect after exiting the second objective lens. This was calculated by exporting the data specified in Table 9 from ZEMAX into Excel and solving for the point in the YZ plane where the two rays intersect. Data numbers 2 and 3 correspond to the y- and z-coordinates of the beginning of the ray segment specified which are respectfully annotated as Y_+ and Z_+ for the ray oriented +2.5° and as Y_- and Z_- for the ray oriented -2.5°. Data numbers 5 and 6 correspond to the y- and z-direction cosines at the beginning of the ray segment specified which are respectfully annotated as U_{y+} and U_{z+} for the ray oriented +2.5° and as U_{y-} and U_{z-} for the ray oriented -2.5°. Using the values specified in Table 9, the y- and z-coordinates of the center of the image plane, Y_{img} and Z_{img} respectively, are calculated as

$$Z_{img} = \frac{C_+ - C_-}{(U_{y-}/U_{z-} - U_{y+}/U_{z+})}; \quad Y_{img} = C_+ + \frac{U_{y+}}{U_{z+}} Z_{img} \qquad (11), (12)$$

where

$$C_\pm = Y_\pm - \frac{U_{y\pm}}{U_{z\pm}} Z_\pm \qquad (13)$$

Table 9: ZEMAX data exported to Excel to determine d_3 given d_1 and d_2.

Source # (from Table 3)	Operand	Segment #	Data #	Notes
4	NSRA	4	2	Y_-
4	NSRA	4	3	Z_-
4	NSRA	5	5	U_{y-}
4	NSRA	5	6	U_{z-}
5	NSRA	4	2	Y_+
5	NSRA	4	3	Z_+
5	NSRA	5	5	U_{y+}
5	NSRA	5	6	U_{z+}

APPENDIX B

MATLAB SIMULATIONS

In simulations of a full three-axis MOA PIIES, the ray data to calculate the image/interference pattern was generated using ZEMAX optical design software in non-sequential analysis mode based on configuration specified by the joint optimization of the MOA PIIES. A total of 30,000,000 analysis rays (10,000,000 per beam) were used calculate the unperturbed interference pattern. All ray data was recorded on a 2000 x 2000 pixel detector in ZEMAX with each pixel corresponding to a size of 5 nm x 5 nm. These data were saved in a .ZRD file format. This file was read into MATLAB using the following .m file

```
clear all;
data = fopen('MOA_35D_NS_Centered.ZRD','r');
version = fread(data,1,'int');
maxsegspossible = fread(data,1,'int');

% Define the total number of rays to be read
total_number_rays = 30000000;
initial_masterarray = zeros(total_number_rays, 12);

for k=1:total_number_rays

% Determine number of segments in the ray
ray1seg = fread(data,1,'int32');
array = zeros(ray1seg,200);

% Pick out Source Beam based of XYZ Coordinate
junk1 = fread(data,48,'char'); % Skip all of the bits before before XYZ
Coordinate of first segment
x1 = fread(data,1,'float64');
y1 = fread(data,1,'float64');
z1 = fread(data,1,'float64');
junk2 = fread(data,128,'char'); % Read the rest of the 1st segment data
if y1 > 10
    source_beam = 1;
elseif x1 < 10
    source_beam = 2;
elseif x1 > 10
```

```
    source_beam = 3;
end;

% Scan past all segments to the final segment
for i=2:ray1seg-1
array(i,:) = fread(data,200,'char');
end;

% Read each data field for the last ray segment
status = fread(data,1,'char');
to_draw = fread(data,1,'char');
junk3 = fread(data,2,'char');
level = fread(data,1,'int32');
hit_object = fread(data,1,'int32');
in_object = fread(data,1,'int32');
int_parent = fread(data,1,'int32');
int_storage = fread(data,1,'int32');
int_xybin = fread(data,1,'int32');
int_lmbin = fread(data,1,'int32');
index = fread(data,1,'float64');
starting_phase = fread(data,1,'float64');
x = fread(data,1,'float64');
y = fread(data,1,'float64');
z = fread(data,1,'float64');
l = fread(data,1,'float64');
m = fread(data,1,'float64');
n = fread(data,1,'float64');
nx = fread(data,1,'float64');
ny = fread(data,1,'float64');
nz = fread(data,1,'float64');
path_to = fread(data,1,'float64');
intensity = fread(data,1,'float64');
phase_of = fread(data,1,'float64');
phase_at = fread(data,1,'float64');
exr = fread(data,1,'float64');
exi = fread(data,1,'float64');
eyr = fread(data,1,'float64');
eyi = fread(data,1,'float64');
ezr = fread(data,1,'float64');
ezi = fread(data,1,'float64');

% Store all data fields in the master array
initial_masterarray(k,:)= [int_xybin source_beam intensity phase_at ...
    exr exi eyr eyi ezr ezi ray1seg k];
end;

% Rearrange data so that is sorted by Pixel Number then Source Beam
new_masterarray = sortrows(initial_masterarray);

save MOA_30M_30D_NS_new_masterarray new_masterarray total_number_rays -
v7.3;
```

Once these data was read into MATLAB, matrices specifying the complex electric field along the x-, y-, and z-directions for each of three beams (nine total matrices) were constructing using the following .m file to calculate the unperturbed interference pattern

```
clear all;
% Load ray file of choice
load MOA_30M_30D_NS_new_masterarray

% Define the dimensions and total number of pixels in the detector
x_pixel_number = 2000;
y_pixel_number = 2000;
total_number_pixels = x_pixel_number*y_pixel_number;

% Setup arrays for recording all components of the Complex Electric
field
% Beam 1
ex_beam_1_array = zeros(y_pixel_number,x_pixel_number);
ey_beam_1_array = zeros(y_pixel_number,x_pixel_number);
ez_beam_1_array = zeros(y_pixel_number,x_pixel_number);
% Beam 2
ex_beam_2_array = zeros(y_pixel_number,x_pixel_number);
ey_beam_2_array = zeros(y_pixel_number,x_pixel_number);
ez_beam_2_array = zeros(y_pixel_number,x_pixel_number);
% Beam 3
ex_beam_3_array = zeros(y_pixel_number,x_pixel_number);
ey_beam_3_array = zeros(y_pixel_number,x_pixel_number);
ez_beam_3_array = zeros(y_pixel_number,x_pixel_number);

% Setup array for beam counter
beam_counter_array = zeros(y_pixel_number,x_pixel_number);

% If mask inserted in Zemax, need to skip past all rays that do not
strike
% the photoresist
j = 1;  % Start at the beginning of new_masterarray
while new_masterarray(j,1) == 0 % Indicates that a ray does not strike
image plane
    j = j + 1;
end;

% Determine the Intensity of Each Individual Pixel and Store in a
Matrix
for q=1:total_number_pixels

% Generate holding matrices for each individual beam
beam_1_holder = zeros(1,12);
beam_2_holder = zeros(1,12);
beam_3_holder = zeros(1,12);
% Generate arrays to hold all rays from each beam
all_beam_1 = beam_1_holder;
```

```
all_beam_2 = beam_2_holder;
all_beam_3 = beam_3_holder;

if j <= length(new_masterarray) && q < new_masterarray(j,1) % Indicates
that the next pixel with data has not been reached
    pixel_intensity_123 = 0;
elseif q > new_masterarray(total_number_rays,1) % Indicates all pixels
with data have been read
    pixel_intensity_123 = 0;
else % Case that there is data to be read
    % See what rays strike this pixel
    k = 1;  % Select rays from Beam 1
    if j > length(new_masterarray) % See if all rays have been
exhausted
        pixel_intensity_123 = 0; % No more rays to analyze
    else
    while j <=  length(new_masterarray) && q == new_masterarray(j,1) &&
k == new_masterarray(j,2)
        new_ray_beam_1 = new_masterarray(j,:);
        all_beam_1 = [all_beam_1; new_ray_beam_1];
        j = j + 1;
    end;
    k = 2; % Select rays from Beam 2
    if j > length(new_masterarray) % See if all rays have been
exhausted
        pixel_intensity_123 = 0; % No more rays to analyze
    else
    while j <=  length(new_masterarray) && q == new_masterarray(j,1) &&
k == new_masterarray(j,2)
        new_ray_beam_2 = new_masterarray(j,:);
        all_beam_2 = [all_beam_2; new_ray_beam_2];
        j = j + 1;
    end;
    k = 3; % Select rays from Beam 3
    if j > length(new_masterarray)  % See if all rays have been
exhausted
        pixel_intensity_123 = 0; % No more rays to analyze
    else
    while j <= length(new_masterarray) && q == new_masterarray(j,1) &&
k == new_masterarray(j,2)
        new_ray_beam_3 = new_masterarray(j,:);
        all_beam_3 = [all_beam_3; new_ray_beam_3];
        j = j + 1;
    end;
    end;
    end;
    end;

    % Calculate Mean values and sums for each beam (remove effects of
1st
    % Row) to Calculate Intensity, Phase, and Electric Field for each
Beam
    % Beam 1
    sum_all_beam_1 = sum(all_beam_1, 1);
```

```
    E_beam_1 = [(sum_all_beam_1(5) + 1i*sum_all_beam_1(6))
(sum_all_beam_1(7) + ...
        1i*sum_all_beam_1(8)) (sum_all_beam_1(9) +
1i*sum_all_beam_1(10))]; % E field expressed as a vector
    I_beam_1 = 0.5*dot(E_beam_1,E_beam_1);

    % Beam 2
    sum_all_beam_2 = sum(all_beam_2, 1);
    E_beam_2 = [(sum_all_beam_2(5) + 1i*sum_all_beam_2(6))
(sum_all_beam_2(7) + ...
        1i*sum_all_beam_2(8)) (sum_all_beam_2(9) +
1i*sum_all_beam_2(10))]; % E field expressed as a vector
    I_beam_2 = 0.5*dot(E_beam_2,E_beam_2);

    % Beam 3
    sum_all_beam_3 = sum(all_beam_3, 1);
    E_beam_3 = [(sum_all_beam_3(5) + 1i*sum_all_beam_3(6))
(sum_all_beam_3(7) + ...
        1i*sum_all_beam_3(8)) (sum_all_beam_3(9) +
1i*sum_all_beam_3(10))]; % E field expressed as a vector
    I_beam_3 = 0.5*dot(E_beam_3,E_beam_3);

    % Enter Beam Counter for each pixel
    if I_beam_1 > 0 && I_beam_2 > 0 && I_beam_3 > 0
        beam_counter = 3;
    elseif (I_beam_1 == 0 || I_beam_2 == 0 || I_beam_3 == 0) &&
((I_beam_1 > 0 && I_beam_2 > 0) || (I_beam_2 > 0 && I_beam_3 > 0) ||
(I_beam_1 > 0 && I_beam_3 > 0))
        beam_counter = 2;
    else
        beam_counter = 1;
    end;

 % Store Electric Field Values in arrays
% Beam 1
% Ex
if rem(q,x_pixel_number) == 0
ex_beam_1_array(ceil(q/x_pixel_number),x_pixel_number) = E_beam_1(1);
else
ex_beam_1_array(ceil(q/x_pixel_number),rem(q,x_pixel_number)) =
E_beam_1(1);
end;
% Ey
if rem(q,x_pixel_number) == 0
ey_beam_1_array(ceil(q/x_pixel_number),x_pixel_number) = E_beam_1(2);
else
ey_beam_1_array(ceil(q/x_pixel_number),rem(q,x_pixel_number)) =
E_beam_1(2);
end;
% Ez
if rem(q,x_pixel_number) == 0
ez_beam_1_array(ceil(q/x_pixel_number),x_pixel_number) = E_beam_1(3);
else
```

```
ez_beam_1_array(ceil(q/x_pixel_number),rem(q,x_pixel_number)) =
E_beam_1(3);
end;

% Beam 2
% Ex
if rem(q,x_pixel_number) == 0
ex_beam_2_array(ceil(q/x_pixel_number),x_pixel_number) = E_beam_2(1);
else
ex_beam_2_array(ceil(q/x_pixel_number),rem(q,x_pixel_number)) =
E_beam_2(1);
end;
% Ey
if rem(q,x_pixel_number) == 0
ey_beam_2_array(ceil(q/x_pixel_number),x_pixel_number) = E_beam_2(2);
else
ey_beam_2_array(ceil(q/x_pixel_number),rem(q,x_pixel_number)) =
E_beam_2(2);
end;
% Ez
if rem(q,x_pixel_number) == 0
ez_beam_2_array(ceil(q/x_pixel_number),x_pixel_number) = E_beam_2(3);
else
ez_beam_2_array(ceil(q/x_pixel_number),rem(q,x_pixel_number)) =
E_beam_2(3);
end;

% Beam 3
% Ex
if rem(q,x_pixel_number) == 0
ex_beam_3_array(ceil(q/x_pixel_number),x_pixel_number) = E_beam_3(1);
else
ex_beam_3_array(ceil(q/x_pixel_number),rem(q,x_pixel_number)) =
E_beam_3(1);
end;
% Ey
if rem(q,x_pixel_number) == 0
ey_beam_3_array(ceil(q/x_pixel_number),x_pixel_number) = E_beam_3(2);
else
ey_beam_3_array(ceil(q/x_pixel_number),rem(q,x_pixel_number)) =
E_beam_3(2);
end;
% Ez
if rem(q,x_pixel_number) == 0
ez_beam_3_array(ceil(q/x_pixel_number),x_pixel_number) = E_beam_3(3);
else
ez_beam_3_array(ceil(q/x_pixel_number),rem(q,x_pixel_number)) =
E_beam_3(3);
end;

% Assign value of pixel to beam counter array
if rem(q,x_pixel_number) == 0
beam_counter_array(ceil(q/x_pixel_number),x_pixel_number) =
beam_counter;
```

```
else
beam_counter_array(ceil(q/x_pixel_number),rem(q,x_pixel_number)) =
beam_counter;
end;

end;

end;

% Save Electric Field Arrays
save MOA_30M_30D_NS_Electric_fields ex_beam_1_array ey_beam_1_array ...
    ez_beam_1_array ex_beam_2_array ey_beam_2_array ez_beam_2_array ...
    ex_beam_3_array ey_beam_3_array ez_beam_3_array x_pixel_number ...
    y_pixel_number beam_counter_array;

% Calculate Interference
% DC component of each of the three beams
dc_1 = 0.5*(real(ex_beam_1_array.*conj(ex_beam_1_array)) + ...
     real(ey_beam_1_array.*conj(ey_beam_1_array)) + ...
     real(ez_beam_1_array.*conj(ez_beam_1_array)));
dc_2 = 0.5*(real(ex_beam_2_array.*conj(ex_beam_2_array)) + ...
     real(ey_beam_2_array.*conj(ey_beam_2_array)) + ...
     real(ez_beam_2_array.*conj(ez_beam_2_array)));
dc_3 = 0.5*(real(ex_beam_3_array.*conj(ex_beam_3_array)) + ...
     real(ey_beam_3_array.*conj(ey_beam_3_array)) + ...
     real(ez_beam_3_array.*conj(ez_beam_3_array)));
dc_123 = dc_1 + dc_2 + dc_3;
% Calculate 3 beam interference
 interference_pattern_123 = dc_123 +
real(ex_beam_1_array.*conj(ex_beam_2_array)) + ...
     real(ey_beam_1_array.*conj(ey_beam_2_array)) + ...
     real(ez_beam_1_array.*conj(ez_beam_2_array)) + ...
     real(ex_beam_1_array.*conj(ex_beam_3_array)) + ...
     real(ey_beam_1_array.*conj(ey_beam_3_array)) + ...
     real(ez_beam_1_array.*conj(ez_beam_3_array)) + ...
     real(ex_beam_2_array.*conj(ex_beam_3_array)) + ...
     real(ey_beam_2_array.*conj(ey_beam_3_array)) + ...
     real(ez_beam_2_array.*conj(ez_beam_3_array));
% Calculated 2 beam interference (12)
 interference_pattern_12 = dc_1 + dc_2 +
real(ex_beam_1_array.*conj(ex_beam_2_array)) + ...
     real(ey_beam_1_array.*conj(ey_beam_2_array)) + ...
     real(ez_beam_1_array.*conj(ez_beam_2_array));
% Calculated 2 beam interference (13)
 interference_pattern_13 = dc_1 + dc_3 +
real(ex_beam_1_array.*conj(ex_beam_3_array)) + ...
     real(ey_beam_1_array.*conj(ey_beam_3_array)) + ...
     real(ez_beam_1_array.*conj(ez_beam_3_array));
% Calculated 2 beam interference (23)
 interference_pattern_23 = dc_2 + dc_3 +
real(ex_beam_2_array.*conj(ex_beam_3_array)) + ...
     real(ey_beam_2_array.*conj(ey_beam_3_array)) + ...
     real(ez_beam_2_array.*conj(ez_beam_3_array));
```

```
smooth_dc_123 = medfilt2(dc_123, [10 10]);
smooth_interference_pattern_123 = medfilt2(interference_pattern_123,
[10 10]);
smooth_interference_pattern_12 = medfilt2(interference_pattern_12, [10
10]);
smooth_interference_pattern_13 = medfilt2(interference_pattern_13, [10
10]);
smooth_interference_pattern_23 = medfilt2(interference_pattern_23, [10
10]);

 % Plot Detector Image (Interference Pattern Only)
figure(1)
surface(smooth_interference_pattern_123,'EdgeColor','none')
figure(2)
surface(smooth_interference_pattern_12,'EdgeColor','none')
figure(3)
surface(smooth_interference_pattern_13,'EdgeColor','none')
figure(4)
surface(smooth_interference_pattern_23,'EdgeColor','none')
```

With the unperturbed interference pattern calculated, 1,000,000 analysis rays were used to calculate the shape of the aberrated mask image for each of the three axes of the MOA PIIES. This ray data was also recorded on a 2000 x 2000 pixel detector in ZEMAX with each pixel corresponding to a size of 5 nm x 5 nm to ensure proper scaling. This ray data was saved in a .ZRD file format which was read into MATLAB using the following .m file to construct a single mask element

```
clear all;
data = fopen('Mask_2.ZRD','r');
version = fread(data,1,'int');
maxsegspossible = fread(data,1,'int');

% Define the total number of rays to be read
total_number_rays = 1000000;
initial_masterarray = zeros(total_number_rays, 2);

for k=1:total_number_rays

% Determine number of segments in the ray
ray1seg = fread(data,1,'int32');
array = zeros(ray1seg,200);

% Pick out Source Beam based of XYZ Coordinate
junk1 = fread(data,48,'char'); % Skip all of the bits before XYZ
Coordinate of first segment
x1 = fread(data,1,'float64');
```

```
y1 = fread(data,1,'float64');
z1 = fread(data,1,'float64');
junk2 = fread(data,128,'char'); % Read the rest of the 1st segment data
if y1 > 10
    source_beam = 1;
elseif x1 < 10
    source_beam = 2;
elseif x1 > 10
    source_beam = 3;
end;

% Scan past all segments to the final segment
for i=2:ray1seg-1
array(i,:) = fread(data,200,'char');
end;

% Read each data field for the last ray segment
status = fread(data,1,'char');
to_draw = fread(data,1,'char');
junk3 = fread(data,2,'char');
level = fread(data,1,'int32');
hit_object = fread(data,1,'int32');
in_object = fread(data,1,'int32');
int_parent = fread(data,1,'int32');
int_storage = fread(data,1,'int32');
int_xybin = fread(data,1,'int32');
int_lmbin = fread(data,1,'int32');
index = fread(data,1,'float64');
starting_phase = fread(data,1,'float64');
x = fread(data,1,'float64');
y = fread(data,1,'float64');
z = fread(data,1,'float64');
l = fread(data,1,'float64');
m = fread(data,1,'float64');
n = fread(data,1,'float64');
nx = fread(data,1,'float64');
ny = fread(data,1,'float64');
nz = fread(data,1,'float64');
path_to = fread(data,1,'float64');
intensity = fread(data,1,'float64');
phase_of = fread(data,1,'float64');
phase_at = fread(data,1,'float64');
exr = fread(data,1,'float64');
exi = fread(data,1,'float64');
eyr = fread(data,1,'float64');
eyi = fread(data,1,'float64');
ezr = fread(data,1,'float64');
ezi = fread(data,1,'float64');

% Store all data fields in the master array
initial_masterarray(k,:)= [int_xybin intensity];
end;

% Rearrange data so that is sorted by Pixel Number
```

```
new_masterarray = sortrows(initial_masterarray);

% Define the dimensions and total number of pixels in the detector
x_pixel_number = 2000;
y_pixel_number = 2000;
total_number_pixels = x_pixel_number*y_pixel_number;

% Define array for mask
mask_array = zeros(y_pixel_number,x_pixel_number);

% With mask inserted in Zemax, need to skip past all rays that do not
strike
% the photoresist
j = 1;  % Start at the beginning of new_masterarray
while new_masterarray(j,1) == 0 % Indicates that a ray does not strike
image plane
    j = j + 1;
end;

% Determine the Intensity of Each Individual Pixel and Store in a
Matrix
for q=1:total_number_pixels

% Generate holding matrices for each individual beam
intensity_holder = zeros(1,1);

% Generate arrays to hold all rays from each beam
all_intensity_holder = intensity_holder;

if j <= length(new_masterarray) && q < new_masterarray(j,1) % Indicates
that the next pixel with data has not been reached
    mask_array_value = 0;
elseif q > new_masterarray(total_number_rays,1) % Indicates all pixels
with data have been read
    mask_array_value = 0;
else % Case that there is data to be read
    % Pick out intensity of each ray in the pixel
    if j > length(new_masterarray) % See if all rays have been
exhausted
        mask_array_value = 0; % No more rays to analyze
    else
    while j <=  length(new_masterarray) && q == new_masterarray(j,1)
        new_intensity_value = new_masterarray(j,2);
        all_intensity_holder = [all_intensity_holder;
new_intensity_value];
        j = j + 1;
    end;
    end;

    % Sum to find intensity of each pixel
    mask_array_value = sum(all_intensity_holder);

     % Store Electric Field Values in arrays
```

```
    if rem(q,x_pixel_number) == 0
    mask_array(ceil(q/x_pixel_number),x_pixel_number) =
mask_array_value;
    else
    mask_array(ceil(q/x_pixel_number),rem(q,x_pixel_number)) =
mask_array_value;
    end;

end;

end;

smooth_mask_array = medfilt2(mask_array, [20 20]);
binary_mask = ceil(smooth_mask_array);

R_set = 100; % Set far away points to 1
for a=1:y_pixel_number
    for b=1:x_pixel_number
        if sqrt((a-1000)^2 + (b-1000)^2) >= R_set;
            binary_mask(a,b) = 1;
        end;
    end;
end;

% Flip ones and zeros for ready use in imaged interference calc., mark
% which beam the mask belongs to.
binary_mask_2 = abs(binary_mask - ones(y_pixel_number,x_pixel_number));

figure(1)
surface(binary_mask_2,'EdgeColor','none')

save MOA_30M_30D_Mask_2_element binary_mask_2;
```

With the complex electric fields and single mask element for each beam formatted as matrix in MATLAB, the final image/interference pattern was calculated with the following .m file

```
clear all;
close all;
% Load Electric Field file of choice
load MOA_30M_30D_NS_Electric_fields

% Calculate Interference
% DC component of each of the three beams
dc_1 = 0.5*(real(ex_beam_1_array.*conj(ex_beam_1_array)) + ...
     real(ey_beam_1_array.*conj(ey_beam_1_array)) + ...
     real(ez_beam_1_array.*conj(ez_beam_1_array)));
dc_2 = 0.5*(real(ex_beam_2_array.*conj(ex_beam_2_array)) + ...
     real(ey_beam_2_array.*conj(ey_beam_2_array)) + ...
```

```
     real(ez_beam_2_array.*conj(ez_beam_2_array)));
dc_3 = 0.5*(real(ex_beam_3_array.*conj(ex_beam_3_array)) + ...
     real(ey_beam_3_array.*conj(ey_beam_3_array)) + ...
     real(ez_beam_3_array.*conj(ez_beam_3_array)));
dc_123 = dc_1 + dc_2 + dc_3;
% Calculate 3 beam interference
 interference_pattern_123 = dc_123 +
real(ex_beam_1_array.*conj(ex_beam_2_array)) + ...
     real(ey_beam_1_array.*conj(ey_beam_2_array)) + ...
     real(ez_beam_1_array.*conj(ez_beam_2_array)) + ...
     real(ex_beam_1_array.*conj(ex_beam_3_array)) + ...
     real(ey_beam_1_array.*conj(ey_beam_3_array)) + ...
     real(ez_beam_1_array.*conj(ez_beam_3_array)) + ...
     real(ex_beam_2_array.*conj(ex_beam_3_array)) + ...
     real(ey_beam_2_array.*conj(ey_beam_3_array)) + ...
     real(ez_beam_2_array.*conj(ez_beam_3_array));
% Calculated 2 beam interference (12)
 interference_pattern_12 = dc_1 + dc_2 +
real(ex_beam_1_array.*conj(ex_beam_2_array)) + ...
     real(ey_beam_1_array.*conj(ey_beam_2_array)) + ...
     real(ez_beam_1_array.*conj(ez_beam_2_array));
% Calculated 2 beam interference (13)
 interference_pattern_13 = dc_1 + dc_3 +
real(ex_beam_1_array.*conj(ex_beam_3_array)) + ...
     real(ey_beam_1_array.*conj(ey_beam_3_array)) + ...
     real(ez_beam_1_array.*conj(ez_beam_3_array));
% Calculated 2 beam interference (23)
 interference_pattern_23 = dc_2 + dc_3 +
real(ex_beam_2_array.*conj(ex_beam_3_array)) + ...
     real(ey_beam_2_array.*conj(ey_beam_3_array)) + ...
     real(ez_beam_2_array.*conj(ez_beam_3_array));

smooth_dc_123 = medfilt2(dc_123, [10 10]);
smooth_interference_pattern_123 = medfilt2(interference_pattern_123,
[10 10]);
smooth_interference_pattern_12 = medfilt2(interference_pattern_12, [10
10]);
smooth_interference_pattern_13 = medfilt2(interference_pattern_13, [10
10]);
smooth_interference_pattern_23 = medfilt2(interference_pattern_23, [10
10]);

 % Plot Detector Image (Interference Pattern Only)
figure(1)
surface(smooth_interference_pattern_123,'EdgeColor','none')
figure(2)
surface(smooth_interference_pattern_12,'EdgeColor','none')
figure(3)
surface(smooth_interference_pattern_13,'EdgeColor','none')
figure(4)
surface(smooth_interference_pattern_23,'EdgeColor','none')

% Introduce Diffraction-Limited Mask and Imaging
% Load Mask Elements for each beam from ZEMAX data
```

```
load MOA_30M_30D_Mask_1_500nm_Offset_1
load MOA_30M_30D_Mask_2_500nm_Offset_1
load MOA_30M_30D_Mask_3_500nm_Offset_1

% Generate Mask Outline Features common to all
mask_outline = zeros(y_pixel_number,x_pixel_number);
x_offset = -100;    % Offset to center on a constr. intfr. feature
y_offset = -100;  % Offset to center on a constr. intfr. feature
motif_spacing = 100; % Number of pixels to the center of next maximum
% Build outline common to all masks (90 Degree Waveguide Bend)
mask_outline(y_pixel_number/2 + y_offset,x_pixel_number/2 + x_offset) =
1;
mask_outline(y_pixel_number/2 + y_offset,x_pixel_number/2+motif_spacing
+ x_offset) = 1;
mask_outline(y_pixel_number/2 +
y_offset,x_pixel_number/2+2*motif_spacing + x_offset) = 1;
mask_outline(y_pixel_number/2 +
y_offset,x_pixel_number/2+3*motif_spacing + x_offset) = 1;
mask_outline(y_pixel_number/2 +
y_offset,x_pixel_number/2+4*motif_spacing + x_offset) = 1;
mask_outline(y_pixel_number/2 +
y_offset,x_pixel_number/2+5*motif_spacing + x_offset) = 1;
mask_outline(y_pixel_number/2 +
y_offset,x_pixel_number/2+6*motif_spacing + x_offset) = 1;
mask_outline(y_pixel_number/2-motif_spacing + y_offset,x_pixel_number/2
+ x_offset) = 1;
mask_outline(y_pixel_number/2-motif_spacing +
y_offset,x_pixel_number/2-motif_spacing + x_offset) = 1;
mask_outline(y_pixel_number/2-2*motif_spacing +
y_offset,x_pixel_number/2-motif_spacing + x_offset) = 1;
mask_outline(y_pixel_number/2-3*motif_spacing +
y_offset,x_pixel_number/2-motif_spacing + x_offset) = 1;
mask_outline(y_pixel_number/2-4*motif_spacing +
y_offset,x_pixel_number/2-motif_spacing + x_offset) = 1;
mask_outline(y_pixel_number/2-5*motif_spacing +
y_offset,x_pixel_number/2-motif_spacing + x_offset) = 1;
mask_outline(y_pixel_number/2-6*motif_spacing +
y_offset,x_pixel_number/2-motif_spacing + x_offset) = 1;
mask_outline(y_pixel_number/2-7*motif_spacing +
y_offset,x_pixel_number/2-motif_spacing + x_offset) = 1;
% Build Each Mask
% Mask 1
mask_conv_1 = conv2(binary_mask_1,mask_outline);
mask_1 = zeros(y_pixel_number,x_pixel_number);
% Cut out center of convolution and flip ones and zeros
for a=1:y_pixel_number
    for b=1:x_pixel_number
        mask_1(a,b) = mask_conv_1((a + y_pixel_number/2),(b +
x_pixel_number/2));
        if mask_1(a,b) >= 1
            mask_1(a,b) = 0;
        elseif mask_1(a,b) == 0
            mask_1(a,b) = 1;
        end;
    end;
```

```
end;

% Mask 2
mask_conv_2 = conv2(binary_mask_2,mask_outline);
mask_2 = zeros(y_pixel_number,x_pixel_number);
% Cut out center of convolution and flip ones and zeros
for a=1:y_pixel_number
    for b=1:x_pixel_number
        mask_2(a,b) = mask_conv_2((a + y_pixel_number/2),(b +
x_pixel_number/2));
        if mask_2(a,b) >= 1
            mask_2(a,b) = 0;
        elseif mask_2(a,b) == 0
            mask_2(a,b) = 1;
        end;
    end;
end;

% Mask 3
mask_conv_3 = conv2(binary_mask_2,mask_outline);
mask_3 = zeros(y_pixel_number,x_pixel_number);
% Cut out center of convolution and flip ones and zeros
for a=1:y_pixel_number
    for b=1:x_pixel_number
        mask_3(a,b) = mask_conv_3((a + y_pixel_number/2),(b +
x_pixel_number/2));
        if mask_3(a,b) >= 1
            mask_3(a,b) = 0;
        elseif mask_3(a,b) == 0
            mask_3(a,b) = 1;
        end;
    end;
end;


% Generate different aperture stops for each beam
% Aperture for Beam 1
aperture_1 = zeros(y_pixel_number,x_pixel_number);
R_ap = 22; % for 2000x2000 pixels (1 pixel = 5x5nm)@ 363.8 nm f1= 200
mm, f2 = 60mm (NA 0.619)
for a=1:y_pixel_number
    for b=1:x_pixel_number
        if sqrt((a-1008)^2 + (b-1000)^2) <= R_ap;
            aperture_1(a,b) = 1;
        else
            aperture_1(a,b) = 0;
        end;
    end;
end;
% Aperture for Beam 2
aperture_2 = zeros(y_pixel_number,x_pixel_number);
for a=1:y_pixel_number
    for b=1:x_pixel_number
        if sqrt((a-1000)^2 + (b-1008)^2) <= R_ap;
```

```
            aperture_2(a,b) = 1;
        else
            aperture_2(a,b) = 0;
        end;
    end;
end;
% Aperture for Beam 3
aperture_3 = zeros(y_pixel_number,x_pixel_number);
for a=1:y_pixel_number
    for b=1:x_pixel_number
        if sqrt((a-1000)^2 + (b-992)^2) <= R_ap;
            aperture_3(a,b) = 1;
        else
            aperture_3(a,b) = 0;
        end;
    end;
end;

fourier_mask_1 = fftshift(fft2(mask_1)).*aperture_1;
diff_mask_1 = ifft2(fourier_mask_1);
fourier_mask_2 = fftshift(fft2(mask_2)).*aperture_2;
diff_mask_2 = ifft2(fourier_mask_2);
fourier_mask_3 = fftshift(fft2(mask_3)).*aperture_3;
diff_mask_3 = ifft2(fourier_mask_3);

% Beam 1
mask_weighted_ex_1 = diff_mask_1.*ex_beam_1_array;
mask_weighted_ey_1 = diff_mask_1.*ey_beam_1_array;
mask_weighted_ez_1 = diff_mask_1.*ez_beam_1_array;

% Beam 2
mask_weighted_ex_2 = diff_mask_2.*ex_beam_2_array;
mask_weighted_ey_2 = diff_mask_2.*ey_beam_2_array;
mask_weighted_ez_2 = diff_mask_2.*ez_beam_2_array;

% Beam 3
mask_weighted_ex_3 = diff_mask_3.*ex_beam_3_array;
mask_weighted_ey_3 = diff_mask_3.*ey_beam_3_array;
mask_weighted_ez_3 = diff_mask_3.*ez_beam_3_array;

% Calculate DC intensity terms for each beam with mask
dc_1_mask = 0.5*(real(mask_weighted_ex_1.*conj(mask_weighted_ex_1)) +
...
     real(mask_weighted_ey_1.*conj(mask_weighted_ey_1)) + ...
     real(mask_weighted_ez_1.*conj(mask_weighted_ez_1)));

dc_2_mask = 0.5*(real(mask_weighted_ex_2.*conj(mask_weighted_ex_2)) +
...
     real(mask_weighted_ey_2.*conj(mask_weighted_ey_2)) + ...
     real(mask_weighted_ez_2.*conj(mask_weighted_ez_2)));

dc_3_mask = 0.5*(real(mask_weighted_ex_3.*conj(mask_weighted_ex_3)) +
...
     real(mask_weighted_ey_3.*conj(mask_weighted_ey_3)) + ...
```

```
     real(mask_weighted_ez_3.*conj(mask_weighted_ez_3)));
dc_123_mask = dc_1_mask + dc_2_mask + dc_3_mask;
% Calculate Interference Pattern with Mask
mask_detector_image = dc_123_mask +
real(mask_weighted_ex_1.*conj(mask_weighted_ex_2)) + ...
     real(mask_weighted_ey_1.*conj(mask_weighted_ey_2)) + ...
     real(mask_weighted_ez_1.*conj(mask_weighted_ez_2)) + ...
     real(mask_weighted_ex_1.*conj(mask_weighted_ex_3)) + ...
     real(mask_weighted_ey_1.*conj(mask_weighted_ey_3)) + ...
     real(mask_weighted_ez_1.*conj(mask_weighted_ez_3)) + ...
     real(mask_weighted_ex_2.*conj(mask_weighted_ex_3)) + ...
     real(mask_weighted_ey_2.*conj(mask_weighted_ey_3)) + ...
     real(mask_weighted_ez_2.*conj(mask_weighted_ez_3));

smooth_mask_detector_image = medfilt2(mask_detector_image, [10 10]);

figure(6)
surface(smooth_mask_detector_image,'EdgeColor','none')
figure(7)
surface(mask_1,'EdgeColor','none')
figure(8)
surface(mask_2,'EdgeColor','none')
figure(9)
surface(mask_3,'EdgeColor','none')

% Smooth Individual beams
smooth_dc_1_mask = medfilt2(dc_1_mask, [10 10]);
smooth_dc_2_mask = medfilt2(dc_2_mask, [10 10]);
smooth_dc_3_mask = medfilt2(dc_3_mask, [10 10]);

figure(10)
surface(smooth_dc_1_mask,'EdgeColor','none')
figure(11)
surface(smooth_dc_2_mask,'EdgeColor','none')
figure(12)
surface(smooth_dc_3_mask,'EdgeColor','none')
```

REFERENCES

[1] G. M. Burrow, *Pattern-Intergrated Interference Lithography: Single-Exposure Formation of Photonic-Crystal Lattices with Integrated Functional Elements*, Ph.D Thesis, School of Electrical and Computer Engineering, Georgia Institute of Technology, Atlanta, Georgia, May 2012.

[2] G. M. Burrow and T. K. Gaylord, "Interference projection exposure system and method of using the same," U. S. Patent Application Publication No. 2012/0081687 filed Sept. 30, 2010.

[3] G. M. Burrow and T. K. Gaylord, "Diffractive photo-mask and methods of using and fabricating the same," U. S. Patent Application Publication No. 2012/0082943 filed Sept. 30, 2010.

[4] G. M. Burrow, M. C. R. Leibovici, and T. K. Gaylord, "Pattern-integrated interference lithography: single-exposure fabrication of photonic-crystal structures," *Appl. Opt.*, vol. 51, pp. 4028-4041, Jun. 20, 2012.

[5] G. M. Burrow, M. C. R. Leibovici, J. W. Kummer, and T. K. Gaylord, "Pattern-integrated interference lithography instrumentation," *Rev. Sci. Instrum.,* vol. 83, pp. 063707-1-063707-10, Jun. 1, 2012.

[6] T. K. Gaylord, M. C. R. Leibovici, and G. M. Burrow, "Pattern-integrated interference [Invited]," *Appl. Opt.*, vol. 52, pp. 61-72, Jan. 1, 2013.

[7] M. C. R. Leibovici, G. M. Burrow, and T. K. Gaylord, "Pattern-integrated interference lithography: prospects for nano- and microelectronics," *Opt. Express*, vol. 20, pp. 23643-23652, Oct. 8, 2012.

[8] M. C. R. Leibovici and T. K. Gaylord, "Simulation of photonic-crystal devices fabricated via pattern-integrated interference lithography," presented at Frontiers in Optics, paper FW1F.5, Orlando, FL, 2013.

[9] M. C. R. Leibovici and T. K. Gaylord, "Pattern-integrated interference lithography: Vector modeling and 1D, 2D, and 3D device structures," *J. Vac. Sci. Technol. B,* vol. 31, 06F501, Nov 2013.

[10] D. E. Sedivy and T. K. Gaylord, "Characterization of multiple-optical-axis implementation of pattern-integratedinterference lithography," presented at Frontiers in Optics, paper FTh3F.2, Orlando, FL, 2013.

[11] M. Rothschild, "Nanopatterning with UV optical lithography," *Mater. Res. Soc. Bull.*, vol. 30, pp. 942-946, Dec. 2005.

[12] M. Fritze, T. M. Bloomstein, B. Tyrrell, T. H. Fedynyshyn, N. N. Efremow Jr, D. E. Hardy, S. Cann, D. Lennon, S. Spector, M. Rothschild, and P. Brooker, "Hybrid optical maskless lithography: scaling beyond the 45 nm node," *J. Vac. Sci. Technol. B,* vol. 23, pp. 2743-2748, Nov./Dec. 2005.

[13] M. Fritze, T. M. Noomstein, B. Tyrrell, and M. Rothschild, "Extending 193nm immersion with hybrid optical maskless lithography," *Sol. St. Technol.,* vol. 49, pp. 41-45, 2006.

[14] M. C. Lemme, C. Moormann, H. Lerch, M. Moller, B. Vratzov, and H. Kurz, "Triple-gate metal-oxide-semiconductor field effect transistors fabricated with interference lithography," *Nanotech.,* vol. 15, pp. 208-210, Feb. 9, 2004.

[15] J. Murakowski, G. J. Schneider, and D. Prather, "Fabrication of 3-dimensional photonic crystals with embedded defects," *Proc. SPIE,* vol. 5347, pp. 181-189, 2004.

[16] Y. C. Chen, J. B. Geddes, J. T. Lee, P. V. Braun, and P. Wiltzius, "Holographically fabricated photonic crystals with large reflectance," *Appl. Phys. Lett.,* vol. 91, pp. 241103-1-241103-3, 2007.

[17] T. Liu, M. Fallahi, J. V. Moloney, and M. Mansuripur, "Fabrication of two-dimensional photonic crystals with embedded defects using blue-laser-writer and optical holography," *IEEE Photonics Technol. Lett.,* vol. 18, pp. 1100-1102, May 1, 2006.

[18] M. Tokushima, J. Ushida, A. Gomyo, M. Shirane, and H. Yamada, "Efficient transmission mechanisms for waveguides with 90 bends in pillar photonic crystals," *J. Opt. Soc. Am. B,* vol. 22, pp. 2472-2479, 2005.

[19] S. Grilli, P. Ferraro, L. Sansone, B. Tiribilli, M. Vassalli, and P. De Natale, "Fabrication of 2D sub-micron structures in lithium niobate for photonic crystal applications," in *Nanoengineering: Fabrication, Properties, Optics, and Devices II*, San Diego, CA, pp. 1-9, August 3, 2005 - August 4, 2005.

[20] G. M. Burrow and T. K. Gaylord, "Multi-beam interference advances and applications: Nano-electronics, photonic crystals, metamaterials, subwavelength structures, optical trapping, and biomedical structures," *Micromachines,* vol. 2, pp. 221-257, June 2011.

[21] C. O. Cho, J. Jeong, J. Lee, H. Jeon, I. Kim, J. D. H., Y. S. Park, and J. C. Woo, "Photonic crystal band edge laser array with a holographically generated square-lattice pattern," *Appl. Phys. Lett.,* vol. 87, pp. 161102-1-161102-3, Oct. 10, 2005.

[22] M. Thorhauge, L. H. Frandsen, and P. I. Borel, "Efficient photonic crystal directional couplers," *Opt. Lett.,* vol. 28, pp. 1525-1527, 2003.

[23] A. Chutinan and S. Noda, "Waveguides and waveguide bends in two-dimensional photonic crystal slabs," *Phys. Rev. B,* vol. 62, pp. 4488-4492, 2000.

[24] M. Campbell, D. N. Sharp, M. T. Harrison, R. G. Denning, and A. J. Turberfield, "Fabrication of photonic crystals for the visible spectrum by holographic lithography," *Nature,* vol. 404, pp. 53-56, Mar. 2, 2000.

[25] A. Lasagni, Y. Dajun, S. Peng, and S. Das, "Rapid fabrication of biocompatible hydrogels microdevices using laser interference lithography," *Proc. SPIE,* vol. 7365, pp. 73650I-1-73650I-9, 2009.

[26] J.-H. Jang, D. Dendukuri, H. T. Alan, E. L. Thomas, and P. S. Doyle, "A route to three-dimensional structures in a microfluidic device: stop-flow interference lithography," *Angewandte Chemie Internat. Ed.,* vol. 46, pp. 9027-9031, Dec. 3, 2007.

[27] N. J. Sniadecki, R. A. Desai, S. A. Ruiz, and C. S. Chen, "Nanotechnology for cell-substrate interactions," *Annals Biomedical Engr.,* vol. 34, pp. 59-74, Jan. 2006.

[28] P. A. Wieringa, R. W. F. Wiertz, E. L. de Weerd, and W. L. C. Rutten, "In vitro verification of a 3-D regenerative neural interface design: examination of neurite growth and electrical properties within a bifurcating microchannel structure," *Proc. IEEE,* vol. 98, pp. 389-397, Mar. 2010.

[29] M. P. Lutolf, F. E. Weber, H. G. Schmoekel, J. C. Schense, T. Kohler, R. Muller, and J. A. Hibbell, "Repair of bone defects using synthetic mimetics of collagenous extracellular matrices," *Nature Biotechnol.,* vol. 21, pp. 513-518, May 2003.

[30] E. L. Hedberg-Dirk and U. A. Martinez, "Large-scale protein arrays generated with interferometric lithography for spatial control of cell-material interactions," *J. Nanomater.,* vol. 2010, pp. 1767501-1767509, May 2010.

[31] S. R. J. Brueck, "Optical and interferometric lithography - nanotechnology enablers," *Proc. IEEE,* vol. 93, pp. 1704-1721, Oct. 2005.

[32] S. R. J. Brueck, X. Chen, A. Frauenglass, S. Zaidi, and J. Wilczynski, "Methods and apparatus for integrating optical and interferometric lithography to produce complex patterns," U. S. Patent 6,233,044 issued May 15, 2001.

[33] S. R. J. Brueck, S. Zaidi, and A. Chu, "Method for fine-line interfererometric lithography," U. S. Patent 5,415,835 issued May 16, 1995.

[34] S. R. J. Brueck, S. H. Zaidi, X. Chen, and Z. Zhang, "Interferometric lithography -- from periodic arrays to arbitrary patterns," *Microelectr. Engr.*, vol. 41-42, pp. 145-148, 1998.

[35] J. L. Stay, *Multi-Beam-Interference-Based Methodology for the Fabrication of Photonic Crystal Structures*, PhD thesis, School of Electrical and Computer Engineering, Georgia Institute of Technology, Atlanta, GA, Oct. 2009.

[36] L. Z. Cai, X. L. Yang, and Y. R. Wang, "Formation of three-dimensional periodic microstructures by interference of four noncoplanar beams," *J. Opt. Soc. Am. A*, vol. 19, pp. 2238-2244, Nov. 2002.

[37] L. Z. Cai, X. L. Yang, and Y. R. Wang, "All fourteen Bravais lattices can be formed by interference of four noncoplanar beams," *Opt. Lett.*, vol. 27, pp. 900-902, June 1, 2002.

[38] M. L. Dakss, L. Kuhn, P. F. Heidrich, and B. A. Scott, "Grating coupler for efficient excitation of optical guided waves in thin films," *Appl. Phys. Lett.*, vol. 16, pp. 523-525, June 15, 1970.

[39] S. H. Zaidi and S. R. J. Brueck, "Multiple-exposure interferometric lithography," *J. Vac. Sci. Technol. B*, vol. 11, pp. 658-666, May/June 1993.

[40] K.-S. Lim, M. Lee, H. Shin, and H. Kim, "Step-wise Ag thin film patterns fabricated by holographic lithography," *Thin Solid Films*, vol. 517, pp. 3273-5, Apr. 2, 2009.

[41] J. H. Jang, C. K. Ullal, M. Maldovan, T. Gorishnyy, S. Kooi, C. Y. Koh, and E. L. Thomas, "3D micro- and nanostructures via interference lithography," *Adv. Funct. Mater.*, vol. 17, pp. 3027-3041, Nov. 5, 2007.

[42] C. S. Peng and C. Tan, "Fast, high efficiency and cost-effective laser nano-lithography," *Proc. SPIE*, vol. 7657, pp. 765708-765712, 2010.

[43] S. Ura, M. Hamada, J. Ohmori, K. Nishio, and K. Kintaka, "Free-space-wave drop demultiplexing waveguide device fabricated by use of the interference exposure method," *Appl. Opt.*, vol. 45, pp. 22-26, Jan. 1, 2006.

[44] M. G. Capeluto, G. Vaschenko, M. Grisham, M. C. Marconi, S. Luduena, L. Pietrasanta, L. Yunfeng, B. Parkinson, C. S. Menoni, and J. J. Rocca, "Nanopatterning with interferometric lithography using a compact $\lambda = 46.9$-nm laser," *IEEE Trans. on Nanotechnol.*, vol. 5, pp. 3-7, Jan. 2006.

[45] H. H. Solak, D. He, W. Li, S. Singh-Gasson, F. Cerrina, B. H. Sohn, X. M. Yang, and P. Nealey, "Exposure of 38 nm period grating patterns with extreme ultraviolet interferometric lithography," *Appl. Phys. Lett.,* vol. 75, pp. 2328-2330, Aug. 18, 1999.

[46] L. Petti, V. Matarazzo, M. Rippa, G. Zito, S. De Nicola, G. Abbate, and P. Mormile, "High resolution lithography as a tool to fabricate quasiperiodic crystals," in *Theoretical and Computational Nanophotonics (TaCoNa-Photonics 2009). 2nd International Workshop,* USA, pp. 146-148, 28-30 Oct. 2009.

[47] M. Qi, E. Lidorikis, P. T. Rakich, S. G. Johnson, J. D. Joannopoulos, E. P. Ippen, and H. I. Smith, "A three-dimensional optical photonic crystal with designed point defects," *Nature,* vol. 429, pp. 538-542, 2004.

[48] R. M. de Ridder, C. G. Bostan, H. A. G. M. van Wolferen, I. van Dorssen, L. Vogelaar, F. B. Segerink, L. Kuipers, and N. F. van Hulst, "Fabrication of photonic crystal slabs and defects using laser interference lithography and focused ion beam-assisted deposition," *Proceedings of the 4th International Conference on Transparent Optical Networks,* vol. 2, pp. 14-19, Apr. 2002.

[49] L. Pang, W. Nakagawa, and Y. Fainman, "Fabrication of two-dimensional photonic crystals with controlled defects by use of multiple exposures and direct write," *Appl. Opt.,* vol. 42, pp. 5450-5456, Sept. 20, 2003.

[50] P. Parisse, D. Luciani, A. D'Angelo, S. Santucci, P. Zuppella, P. Tucceri, A. Reale, and L. Ottaviano, "Patterning at the nanoscale: atomic force microscopy and extreme ultraviolet interference lithography," *Mater. Sci. Engr. B,* vol. 165, pp. 227-230, Dec. 15, 2009.

[51] N. D. Lai, T. S. Zheng, D. B. Do, J. H. Lin, and C. C. Hsu, "Fabrication of desired three-dimensional structures by holographic assembly technique," *Appl. Phys. A,* vol. 100, pp. 171-175, July 2010.

[52] T. Horiuchi, K. Harada, S. Matsuo, Y. Takeuchi, E. Tamechika, and Y. Mimura, "Resolution enhancement by oblique illumination optical lithography using a transmittance-adjusted pupil filter," *Jpn. J. Appl. Phys.,* vol. 34, pp. 1698 -1708, Mar. 1995.

[53] N. D. Lai, W. P. Liang, J. H. Lin, and C. C. Hsu, "Rapid fabrication of large-area periodic structures containing well-defined defects by combining holography and mask techniques," *Opt. Express,* vol. 13, pp. 5331-5337, July 11, 2005.

[54] C. A. Mack, *Field Guide to Optical Lithgraphy*. Bellingham, Washington: SPIE Press, pp. 81-83, 2006.

[55] W. J. Smith, *Modern Optical Engineering*, Third ed. New York: McGraw-Hll, pp. 52-53, 2000.

[56] L.-J. Lu, X.-Y. Hu, and C.-Y. Sheng, "Optimization method for ultra-wide-angle and panoramic optical systems," *Appl. Opt.*, vol. 51, pp. 3776-3786, Jun 10, 2012.

[57] M. M. Talha, Y. Wang, D. Cheng, and J. Chang, "Design of a compact wide field of view HMD optical system using freeform surfaces - art. no. 662416," in *International Symposium on Photoelectronic Detection and Imaging 2007: Optoelectronic System Design, Manufacturing, and Testing*. vol. 6624, pp. 662416-1-662416-14, 2008.

[58] S. F. Ray, *Applied Photographic Optics*, 3rd ed.: Oxford, pp. 415-419, 2002.

[59] J. D. Cooper, *Nikon-Nikkormat Handbook*. Garden City, NY 11530: American Photographic Book Publishing Co., Inc., pp. 1-13, 1974.

[60] K. Roberts, D. Beckett, D. Boertjes, J. Berthold, and C. Laperle, "100G and beyond with digital coherent signal processing," *IEEE Comm. Mag.*, vol. 48, pp. 62-69, Jul 2010.

[61] K. Roberts, "100G-key technology enablers of 100Gbit/s in carrier networks," presented at the 2011 Optical Fiber Communication Conference and Exposition, Washington, 2011.

[62] S. Tsunashima, F. Nakajima, Y. Nasu, R. Kasahara, Y. Nakanishi, T. Saida, T. Yamada, K. Sano, T. Hashimoto, H. Fukuyama, H. Nosaka, and K. Murata, "Silica-based, compact and variable-optical-attenuator integrated coherent receiver with stable optoelectronic coupling system," *Opt. Express*, vol. 20, pp. 27174-27179, Nov 2012.

[63] J. W. Goodman, *Introduction to Fourier Optics*. San Francisco, Mcgraw-hill, pp. 76-77, 1968.

[64] G. M. Burrow, M. C. R. Leibovici, J. W. Kummer, and T. K. Gaylord, "Pattern-integrated interference lithography instrumentation," *Rev. Sci. Instrum.*, vol 83, pp. 063707-1-063707-10, Jun. 1, 2012

[65] T. K. Gaylord, J. L. Stay, and G. M. Burrow, "Method of fabricating photo-masks for implementation of multi-beam interference lithography," Georgia Tech Record of Invention No. 4991, Sept. 18, 2009.

[66] *Zemax Optical Design Program User's Guide*: Focus Software, Inc., Tucson, Arizona, 2003.

[67] A. K.-K. Wong, *Optical imaging in projection microlithography*. SPIE Optical Engineering Press: Bellingham, WA, pp. 51-67, 2005.

[68] J. L. Stay, G. M. Burrow, and T. K. Gaylord, "Three-beam interference lithography methodology," *Rev. Sci. Instrum.*, vol. 82, pp. 231151-231158, Mar. 1, 2011.

[69] D. E. Sedivy and T. K. Gaylord, "Modeling of multiple-optical-axis pattern-integrated interference lithography systems," *Appl. Opt.*, vol. 53, Accepted, May 2014.